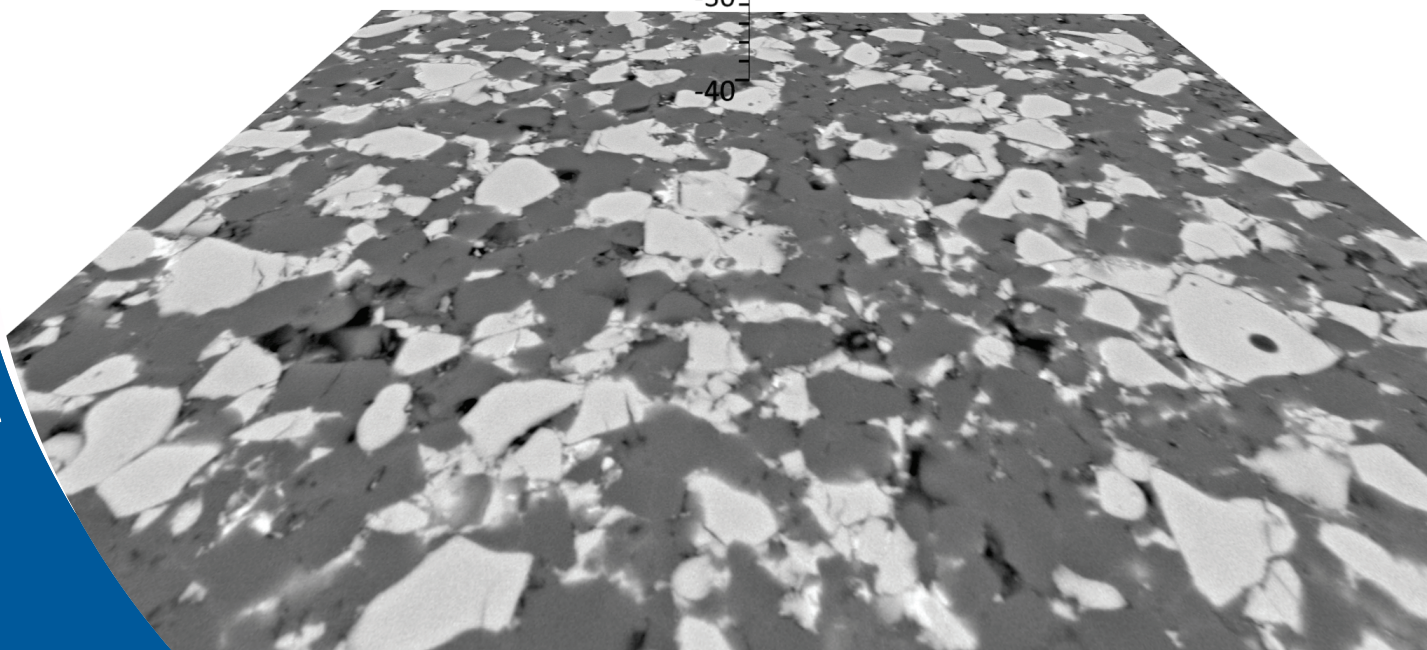
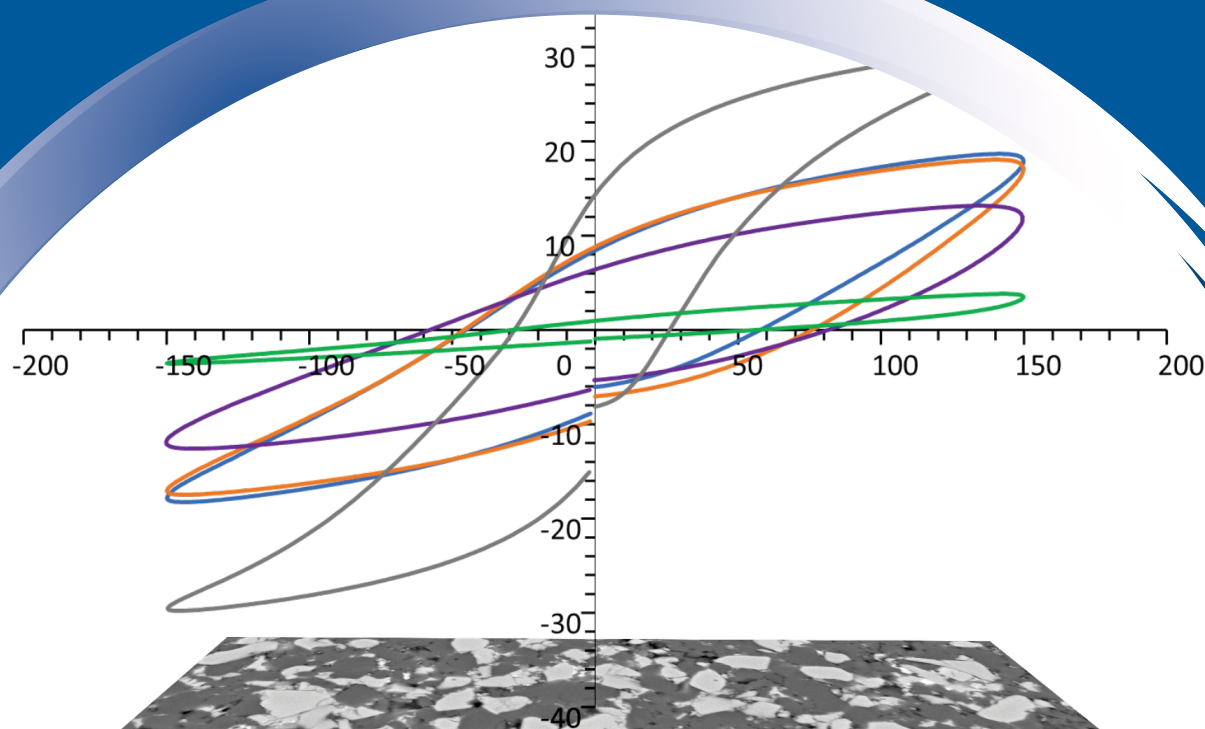


ISSN 0352-9045

Informacije MIDEM

*Journal of Microelectronics,
Electronic Components and Materials*
Vol. 54, No. 3(2024), September 2024

*Revija za mikroelektroniko,
elektronske sestavne dele in materiale*
letnik 54, številka 3(2024), September 2024



Informacije MIDEM 3-2024

Journal of Microelectronics, Electronic Components and Materials

VOLUME 54, NO. 3(191), LJUBLJANA, SEPTEMBER 2024 | LETNIK 54, NO. 3(191), LJUBLJANA, SEPTEMBER 2024

Published quarterly (March, June, September, December) by Society for Microelectronics, Electronic Components and Materials - MIDEM.
Copyright © 2024. All rights reserved. | Revija izhaja trimesečno (marec, junij, september, december). Izdaja Strokovno društvo za mikroelektroniko, elektronske sestavne dele in materiale – Društvo MIDEM. Copyright © 2024. Vse pravice pridržane.

Editor in Chief | Glavni in odgovorni urednik

Marko Topič, University of Ljubljana (UL), Faculty of Electrical Engineering, Slovenia

Editor of Electronic Edition | Urednik elektronske izdaje

Kristijan Brecl, UL, Faculty of Electrical Engineering, Slovenia

Associate Editors | Odgovorni področni uredniki

Vanja Ambrožič, UL, Faculty of Electrical Engineering, Slovenia

Arpad Bürmen, UL, Faculty of Electrical Engineering, Slovenia

Danjela Kuščer Hrovatin, Jožef Stefan Institute, Slovenia

Matija Pirc, UL, Faculty of Electrical Engineering, Slovenia

Franc Smole, UL, Faculty of Electrical Engineering, Slovenia

Matjaž Vidmar, UL, Faculty of Electrical Engineering, Slovenia

Editorial Board | Uredniški odbor

Mohamed Akil, ESIEE PARIS, France

Giuseppe Buja, University of Padova, Italy

Gian-Franco Dalla Betta, University of Trento, Italy

Martyn Fice, University College London, United Kingdom

Ciprian Iliescu, Institute of Bioengineering and Nanotechnology, A*STAR, Singapore

Marc Lethiecq, University of Tours, France

Teresa Orłowska-Kowalska, Wrocław University of Technology, Poland

Luca Palmieri, University of Padova, Italy

Goran Stojanović, University of Novi Sad, Serbia

International Advisory Board | Časopisni svet

Janez Trontelj, UL, Faculty of Electrical Engineering, Slovenia - Chairman

Cor Claeys, IMEC, Leuven, Belgium

Denis Donlagič, University of Maribor, Faculty of Elec. Eng. and Computer Science, Slovenia

Zvonko Fazarinc, CIS, Stanford University, Stanford, USA

Leszek J. Golonka, Technical University Wrocław, Wrocław, Poland

Jean-Marie Haussonne, EIC-LUSAC, Octeville, France

Barbara Malič, Jožef Stefan Institute, Slovenia

Miran Mozetič, Jožef Stefan Institute, Slovenia

Stane Pejovnik, UL, Faculty of Chemistry and Chemical Technology, Slovenia

Giorgio Pignatelli, University of Perugia, Italy

Giovanni Soncini, University of Trento, Trento, Italy

Iztok Šorli, MIKROIKS d.o.o., Ljubljana, Slovenia

Hong Wang, Xi'an Jiaotong University, China

Headquarters | Naslov uredništva

Uredništvo Informacije MIDEM

MIDEM pri MIKROIKS

Stegne 11, 1521 Ljubljana, Slovenia

T. +386 (0)1 513 37 68

F. + 386 (0)1 513 37 71

E. info@midem-drustvo.si

www.midem-drustvo.si

Annual subscription rate is 160 EUR, separate issue is 40 EUR. MIDEM members and Society sponsors receive current issues for free. Scientific Council for Technical Sciences of Slovenian Research Agency has recognized Informacije MIDEM as scientific Journal for microelectronics, electronic components and materials. Publishing of the Journal is co-financed by Slovenian Research Agency and by Society sponsors. Scientific and professional papers published in the journal are indexed and abstracted in COBISS and INSPEC databases. The Journal is indexed by ISI® for Sci Search®, Research Alert® and Material Science Citation Index™.

Letna naročnina je 160 EUR, cena posamezne številke pa 40 EUR. Člani in sponzorji MIDEM prejema posamezne številke brezplačno. Znanstveni svet za tehnične vede je podal pozitivno mnenje o reviji kot znanstveno-strokovni reviji za mikroelektroniko, elektronske sestavne dele in materiale. Izdajo revije sofinancirajo ARRS in sponzorji društva. Znanstveno-strokovne prispevke objavljene v Informacijah MIDEM zajemamo v podatkovne baze COBISS in INSPEC. Prispevke iz revije zajema ISI® v naslednje svoje produkte: Sci Search®, Research Alert® in Materials Science Citation Index™.

Design | Oblikovanje: Snežana Madič Lešnik; Printed by | tisk: Biro M, Ljubljana; Circulation | Naklada: 1000 issues | izvodov; Slovenia Taxe Percue | Poštnina plačana pri pošti 1102 Ljubljana

Content | Vsebina

Original scientific papers

Izvirni znanstveni članki

A. Farkasvölgyi, L. Csurgai-Horváth, A. Hilt: High Resolution Rain Intensity Measurement and its Application on Free Space Optics	167	A. Farkasvölgyi, L. Csurgai-Horváth, A. Hilt: Merjenje intenzivnosti dežja z visoko ločljivostjo in njegova uporaba v optiki prostega prostora
M. Šadl, B. Repič, I. Goričan, D. Kuščer and H. Uršič: Aerosol-Deposition-Derived Graphite Thick Films for Electrochemical Sensors	177	M. Šadl, B. Repič, I. Goričan, D. Kuščer and H. Uršič: Debele plasti grafita nanešene v aerosolu za elektrokemijske senzorje
S. S. Subramanian, M. Gandhi: Low Power CMOS Full Adder Cells based on Alternative Logic for High-Speed Arithmetic Applications	187	S. S. Subramanian, M. Gandhi: Celice CMOS z nizko porabo energije na osnovi alternativne logike za hitre aritmetične aplikacije
P. Ramamoorthy, K. Ramanathan: A Novel Method for 5Generation Multiple-Input, Multiple-Output Orthogonal Frequency-Division Multiplexing using Cauchy Evading Golden Tortoise Adaptive-Bi Directional-Long Short-Term Memory	201	P. Ramamoorthy, K. Ramanathan: Nova optimizacijska metoda izogibanja zlati želvi za oceno MIMO OFDM 5G kanala
B. Velkavrh, U. Tomc, M. Šadl, V. Regis, M. Koblar, B. Colarič, A. Kitanovski and H. Uršič: Preparation of Dielectric Layers for Applications in Digital Microfluidic Thermal Switches	215	B. Velkavrh, U. Tomc, M. Šadl, V. Regis, M. Koblar, B. Colarič, A. Kitanovski and H. Uršič: Priprava dielektričnih plasti za uporabo v digitalnih mikrofluidnih toplotnih stikalih
S. Salmanov, D. Kuščer, M. Otoničar: Cold Sintering of Perovskite-Perovskite Particulate Composite Based on $K_{0.5}Na_{0.5}NbO_3$ and $BiFeO_3$	225	S. Salmanov, D. Kuščer, M. Otoničar: Hladno sintranje prahov perovskitov na osnovi $K_{0.5}Na_{0.5}NbO_3$ in $BiFeO_3$
Front page: Polarization response to applied electric field in $BiFeO_3$ - $K_{0.5}Na_{0.5}NbO_3$ ceramic composites and their end-members, prepared by the cold sintering pro- cess. (Salmanov et al.)		Naslovnica: Polarizacija v odvisnosti od električnega polja v hladno sintranih keramičnih kompozitih $BiFeO_3$ - $K_{0.5}Na_{0.5}NbO_3$ in krajnih trdnih raztopinah. (Salmanov et al.)

High Resolution Rain Intensity Measurement and its Application on Free Space Optics

Andrea Farkasvölgyi¹, László Csurgai-Horváth¹, Attila Hilt¹

¹Department of Broadband Infocommunications and Electromagnetic Theory, Budapest University of Technology and Economics, Budapest, Hungary

Abstract: Thunderstorms affect our everyday life. Among the various types of precipitation, it is extremely important to determine rain intensity both for scientific and for economic reasons. Various traditional meteorological methods and other techniques, such as radio measurements can be applied to this. The fluctuation of the received signal level, occurring on radio connections, especially in the shorter millimeter wavelength range, strongly depends on the rain intensity. Thus, the fading phenomenon is also suitable for measuring the rain intensity indirectly. We present our new method of producing calibrated attenuation time series from the measured data of the received signal level, which can be used to directly express the rain intensity. It is concluded that the method is suitable for the detection of rapid and instantaneous changes in rain intensity due to the high sampling rate. Our results have many possible applications: from high-resolution detection of time-varying rainfall intensity to adaptive communication control systems with short reaction times. We present the effect of heavy rainfall on free-space optical connections, an important secure and high data rate link type. We assume that high-intensity rain would result in the disturbance of optical connections and worst-case it would result in its interruption. We analyzed the magnitude of deterioration by the probability of fade. Based on our results, we draw attention to the fact that nowadays increasingly frequent, high-intensity precipitation bursts can damage optical connections. We advise some solutions to eliminate the harmful effects of intense rain.

Keywords: mmW; high resolution measurement; rain intensity sensing; FSO link; outage probability

Merjenje intenzivnosti dežja z visoko ločljivostjo in njegova uporaba v optiki prostega prostora

Izvleček: Nevihte vplivajo na naše vsakdanje življenje. Med različnimi vrstami padavin je iz znanstvenih in gospodarskih razlogov izjemno pomembno določiti jakost dežja. Pri tem lahko uporabimo različne tradicionalne meteorološke metode in druge tehnike, kot so radijske meritve. Nihanje ravni sprejetega signala, ki se pojavlja na radijskih povezavah, zlasti v krajšem območju milimetrskih valovnih dolžin, je močno odvisno od intenzivnosti dežja. Zato je pojav bledenja primeren tudi za posredno merjenje intenzivnosti dežja. Predstavljamo našo novo metodo izdelave umerjenih časovnih vrst slabljenja iz izmerjenih podatkov o ravni sprejetega signala, ki se lahko uporabijo za neposredno izražanje intenzivnosti dežja. Ugotavljamo, da je metoda zaradi visoke stopnje vzorčenja primerna za zaznavanje hitrih in trenutnih sprememb intenzivnosti dežja. Naši rezultati se lahko velikokrat uporabijo: od zaznavanja časovno spremenljive intenzivnosti dežja z visoko ločljivostjo do prilagodljivih sistemov za nadzor komuniciranja s kratkimi reakcijskimi časi. Predstavljamo vpliv močnega deževja na optične povezave v prostem prostoru, ki so pomembna vrsta varnih povezav z visoko hitrostjo prenosa podatkov. Predpostavljamo, da bi močno deževje povzročilo motnje optičnih povezav, v najslabšem primeru pa bi povzročilo njihovo prekinitev. Velikost poslabšanja smo analizirali z verjetnostjo izginotja. Na podlagi naših rezultatov opozarjamo na dejstvo, da lahko dandanes vse pogostejši, visoko intenzivni nalivi poškodujejo optične povezave. Svetujemo nekaj rešitev za odpravo škodljivih učinkov intenzivnega dežja.

Ključne besede: mmW; merjenje visoke ločljivosti; zaznavanje intenzivnosti dežja; povezava FSO; verjetnost izpada

* Corresponding Author's e-mail: farkasvolgyi.andrea@vik.bme.hu, csurgai-horvath.laszlo@vik.bme.hu, hilt.attila@vik.bme.hu

How to cite:

A. Farkasvölgyi et al., "High Resolution Rain Intensity Measurement and its Application on Free Space Optics", Inf. Midem-J. Microelectron. Electron. Compon. Mater., Vol. 54, No. 3(2024), pp. 167–175

1 Introduction

Rain intensity is a very important physical quantity whose measurement is fundamental in many areas. Meteorological observations, agricultural purposes, flight safety, and even the quality of terrestrial or satellite radio communication at millimetric wavelengths (mmW) are closely related to the amount of liquid precipitation [1-3]. Various types of measurement devices are suitable for measuring precipitation, including rain intensity, from simple tipping bucket gauges or drop counter sensors to real-time sensors or radar-based measurements [4]. In general, the devices for measuring rain intensity work with a certain integration time, which can be several minutes long. The measurement result provided by these devices is expressed as the rain intensity in [mm/h] detected at the geographic location of the measuring system. Considering mmW radio connections, the received signal power is affected by precipitation, especially by the attenuation of intensive rainfalls [2, 3]. On the other hand, this phenomenon can be used to determine the magnitude of the rain intensity from the rain attenuation [5], for which the appropriate calculations can be found in the relevant recommendations of ITU, the International Telecommunications Union [6]. On longer radio connections, we must account for the difference between the effective and the real path lengths [7]. However, on very short connections, it can be assumed that the rain affects the whole path length with uniform rain attenuation. Consequently, in this article our findings are also based on this assumption. We present a new method based on a computation of rain intensity from the change in signal level, measured on a very short radio hop operating in the 58 GHz band. The great advantage of the method is that the instantaneous rain intensity can be determined with high resolution, which is limited only by the sampling rate of the received signal level (RSL). The process provides a solution for the rapid detection of precipitation conditions and many practical application possibilities can be assigned for our new detection process.

The rest of the paper is organized as follows. Section 2 briefly introduces the applied measurement setup, using an experimental millimeter wave wireless radio link. Section 3 explains the data processing method of the measured received power level time series, in order to obtain the required attenuation time series. Section 4 introduces the inverse method to get rain attenuation time series from the attenuation time series data. Sections 5 and 6 present the impact of high-intensity precipitation on Free Space Optical (FSO) links by estimating the deterioration of outage probability. Finally, the application areas, remarks and conclusions are given in Sections 7, 8 and 9.

2 The measurement setup

The primary objective of this paper is to estimate the intensity of rainfall by analyzing the received signal power level of a radio link. The measurements are carried out by an experimental full-duplex V-band radio link. The used Nokia MetroHopper wireless access link has been originally designed for dense microcellular networks [8, 9]. This 58 GHz radio is set up to function over short distances to establish a low-latency connection to base stations. The main parameters of the implemented link are listed in Table 1., while the location and the outdoor radio unit can be seen in Fig. 1.

Table 1: Radio link parameters

Location	Budapest
Path length	d = 118 m
Frequency	f = 57.725 GHz
Link polarization	Vertical (V)
Typical TX output power	+5 dBm
TX/RX antenna gain	G = 34 dBi
BER=10 ⁻³ threshold	-75 dBm
BER=10 ⁻⁶ threshold	-73 dBm
Link capacity	4 x 2 Mbit/s

The radio indoor units have been installed at both ends of the link, providing a local management interface and ports for the 4x2 Mbit/s capacity. In our experimental setup payload data was not transmitted, only the received signal strength was monitored in [dBm] and logged with a granularity of 1 sample/second via the scripting tool of the management interface.



Figure 1: MetroHopper link between two buildings.

The free space path loss (FSL) of the experimental link is [3, 10]:

$$FSL^{[dB]} = 92.4^{[dB]} + 20\log_{10}(f^{[GHz]}) + 20\log_{10}(d^{[km]}) \quad (1)$$

Where f is the link frequency in [GHz] and d is the hop length in [km]. With the parameters of Table 1, $FSL=109$

dB. There is an additional attenuation due to the atmospheric gases, especially the effect of oxygen adds a further 1.1 dB [7, 11].

The typical (and nonadjustable) output power of the radio units is $P_{TX} = +5$ dBm [8]. The link polarization is vertical. After the alignment of the outdoor units, with the device parameters listed in Table 1., during clear sky conditions the measured received signal power level is roughly -56 dBm at the receiver side. According to the MetroHopper radio User's Manual [8], the minimum required RSL is -75 dBm (for $BER = 10^{-3}$) resulting a 19 dB fade margin for the measurement setup. Considering the very short hop length, this fade margin is sufficiently high to detect even the most intensive rain events in Budapest.

3 Processing of the received signal level data

For this study we processed the received power measurements on the experimental link between 1st of January to 28th of February 2023, when the availability of the data was 93%. This period was noticeably rainy in Hungary and the temperature was always above 0°C, therefore all precipitation was in liquid form. In Fig. 2. the time series of measured received power is depicted for January 2023:

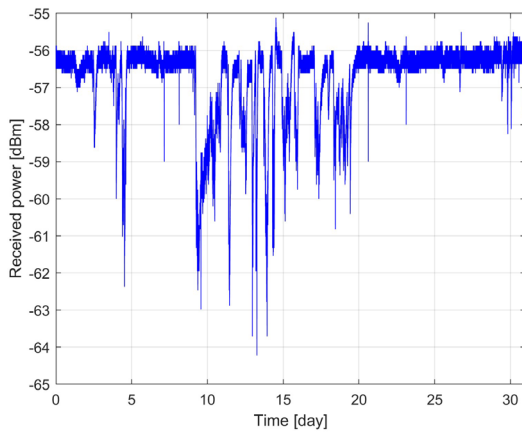


Figure 2: Received power time series for January 2023 (with one second resolution).

ITU-R P.838-3 [6] gives the relationship between specific attenuation γ_R and rain intensity R as:

$$A^{[dB]} = d^{[km]} \cdot \gamma_R^{[dB/km]} = d \cdot k_{H/V} \cdot R^{\alpha_{H/V}} \quad (2)$$

where d is the length of the radio link in [km], R is the rain rate in [mm/h]. Constants k and α are frequency

and polarization dependent values according to ITU-R P.838-3 [6]. In the case of our vertically (V) polarized experimental 58 GHz link, these constants are $k_V=0.8129$ and $\alpha_V=0.7552$.

When we apply the inverse form of the equation (2) given in ITU-R P.838-3, the momentary value of rain intensity R_i can be expressed as:

$$R_i^{[mm/h]} = 10^{\frac{\log_{10}\left(\frac{A_i}{d \cdot k}\right)}{\alpha}} \quad (3)$$

where A_i is the i^{th} value of the path attenuation time series in [dB], and d is the link length in [km] as in Eq. (2). We note that because of the very short link, the effective path length and the actual path length can be considered equal in our case.

Please note, that the momentary value of R_i is calculated from a high-resolution data collection. Even though according to Eq. (2)-(3), the unit of R_i is given in [mm/h], R_i represents values obtained from very frequent measurements of 1 sample/second R_i^* as discussed in part 4. When hourly rain volume is required, the R_i^* sample/second values can be converted to mm/h values as:

$$R_i^{[mm/h]} = \frac{1}{3600} \sum_{i=1}^{3600} R_i^{*[mm/h]} \quad (4)$$

Path attenuation cannot be directly measured; it is the difference between the clear sky level and the momentary measured received signal power RSL_i in [dBm]. As the simplest solution, the clear sky level can be determined as the median of the received power during a precipitation-free day. In equation (2) the attenuation, and indirectly the clear sky level appears in the exponent of the equation, thus the resulting rain intensity value is very sensitive to this parameter. However, even a daily clear sky level may slightly vary due to the temperature variation of the air or the outdoor radio units, or due to the changes in the air humidity or the concentration of the atmospheric gases. This may introduce an uncertainty to the process.

In order to get a calibrated result, concurrent measurement data of a weather station was applied, especially the total amount of rain for one month. This weather station is part of the MetNet network [12], collecting several meteorological data such as temperature, humidity, heat index, dew point, wind direction and speed, air pressure and rain intensity. The distance between the weather station and our radio link is only 763 m, therefore it can be expected that there is no significant difference between the total monthly amount

of rain at the two different locations. The calibration method for January 2023 was as it follows:

1. select one clear sky day and determine the median of the received signal level (8th January):
 $RSL_m = -56.3$ dBm
2. transform received power time series to attenuation time series with $A_i = RSL_m - RSL_i$ [dB]
3. calculate the time series of rain intensity R_i with equation (3)
4. determine the total amount of rain R_{total} in [mm/month] during the whole month as:

$$R_{total} \left[\frac{\text{mm}}{\text{month}} \right] = \frac{1}{3600} \sum_{i=1}^{31 \cdot 24 \cdot 3600} R_i^* \left[\frac{\text{mm}}{\text{h}} \right] \quad (5)$$

5. get the total amount of rain for January from the MetNet data ($R_M = 102.9$ mm/month)
6. modify the value of median RSL_m and repeat the process from step 2 until $R_M = R_{total}$ (in mm that has fallen during the entire month).

Applying the process described above, a calibrated time series of rain intensity can be determined for the whole month, as it can be seen in Fig. 3. The upper plot shows the rain intensity time series as resulted with the simple median value. The lower plot presents the rain intensity after calibration. Using the above recursive steps 2-6, the original median clear sky received power level for January was modified from -56.3 dBm to -60.65 dBm, resulting an identical value that was recorded by the MetNet station. Due to the stability of the radio connection and the meteorological station's equipment, it is enough to perform the calibration once, and it can also be applied correctly in case of further measurements.

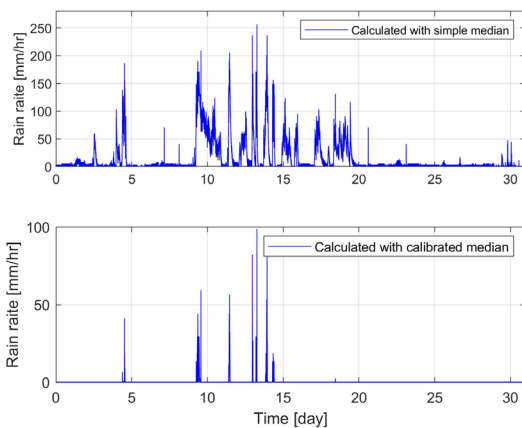


Figure 3: Time series of rain intensity for January 2023, calculated with simple median (top) and by using the calibration method (bottom).

4 Detecting rain attenuation with high resolution

In sections 2 and 3, we demonstrated that a short distance millimeter wavelength radio link can be utilized to sense the momentary rain intensity by measuring the received signal level and convert it to rain intensity time series. A supporting calibration process ensures the validity of the transformed rain intensity data. The most important advantage of the method is that the sampling rate of the resultant rain intensity time series is identical to the sampling rate of the RSL over the radio link. Actually, this is 1 sample/sec, therefore the fast changes in the rain intensity can be also detected, contrarily to the conventional sensors, that usually smooth the high peaks due to their integrating behaviour.

Fig. 4. depicts a typical rain event in January 2023 with a duration of approximately 5 minutes. In the center of the rainfall event a fast increase of the rain intensity is observable, having a duration of only 15 seconds.

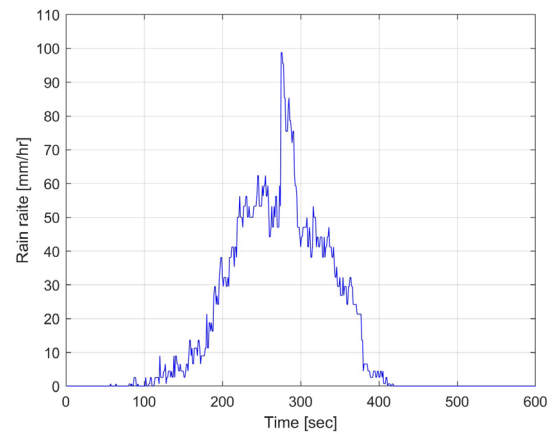


Figure 4: Single rain event with high instantaneous peak intensity. Measured on 13th of January 2023.

Another similar effect can be observed in Fig. 5., detected on 20th of February 2023 with a length of 50 seconds. An extreme peak of the rain intensity is observable with only 5 seconds duration, when the rain intensity increased almost two times higher than in the surrounding periods.

5 Discussion of high-resolution detection

There could be several application areas of this kind of rain intensity sensing. In case of adaptive control of the modulation and coding over terrestrial or satellite communication links [13] high resolution and fast information about the momentary rain intensity may support the adaptive algorithm and higher throughput can be achieved. In case of a diversity systems, when several

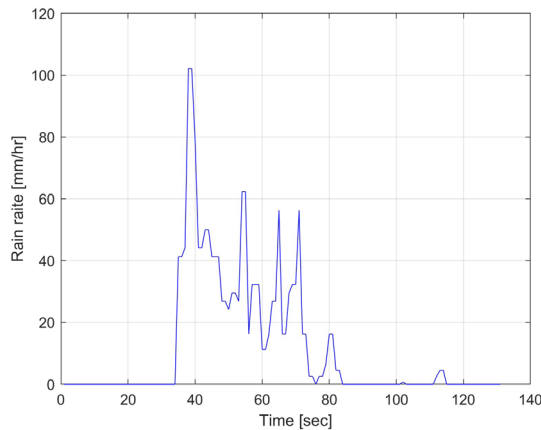


Figure 5: Single rain event with short duration peak intensity. Detected on 20th of February 2023.

radio stations are operated at multiple geographical locations, the perfect knowledge about the local rain rate changes may be very advantageous. Similarly, if diversity radio and free space optical links are concurrently operated over the same path, the fast-switching control of the two different media may increase the channel capacity and maintain the overall link availability. Applying legacy, constant bit rate mmW radios in the 58 GHz band for the continuous rain intensity monitoring has some advantages. Firstly, the high atmospheric attenuation reduces the maximum radio hop lengths in Europe, typically below 1 km [3, 7, 9, 15]. For the same reason, the probability of unwanted interference from other mmW transceivers is smaller. Secondly, the novel Gbit/s radios in E-band (80 GHz) switch adaptively when signal to noise ratio degrades due to precipitation or interference [3, 14]. Continuous switching between modulation modes would result in less accurate rain intensity measurement as different transmit power and received signal thresholds apply to different symbol rates [3, 7, 15]. Finally, in several countries, the V-band is either unlicensed or the frequency fees are moderate due to the high atmospheric losses around 58-60 GHz [7, 9]. Therefore, 58 GHz links can operate as a continuous backup for FSO links to provide guaranteed bit rates in foggy days when FSO capacity is reduced [27].

6 Impact of high-intensity precipitation on FSO communication links

Planning a new terrestrial wireless connection, the current environmental challenges caused by meteorological events of recent years must be taken into account. Some few years ago, intense rainfall was not a problem in this region of Central Europe. A decade ago, the outage probability of RF links due to rain were orders of

magnitude less frequent than in recent years. This is why we must reconsider the effects of intense rain. Based on own long-term experience and measurements, the impact of short-term, very intense precipitation event which greatly deteriorates the availability of the connection becomes an increasingly serious problem. This point is confirmed by measurements from other research centers [16, 17]. The long-term statistics used previously do not include the effects of very short and very intense precipitation events. It is not enough to plan the terrestrial connections based only on average values of rainfall rate. Intensive precipitation events must be monitored and compensated rapidly and adaptively. For this monitoring and compensation method, the instantaneous rainfall rate is required at very short intervals. To measure rapid precipitation events, the measurement of rainfall-rates averaged over minutes or hours is unfortunately not sufficient. The rainfall intensity determination method, presented in part 3 is suitable for a quick determination of the instantaneous rain intensity, by which the outage probability of the connection can be reduced, and such the reliability improved. Note, that even though the average rainfall intensity has negligible influence on the FSO connections, the intense precipitation significantly decreases the availability of the connection. Therefore, because of the recent climate changes in our environment, we should manage this new influence and deal with the effect of intense rain on the FSO link. Compensating the effect of intense precipitation on FSO links is less demanding than on RF hops. This is because rain affects FSO much less than RF links, which is validated by our calculations. In the FSO connection, the outage probability of fade does not alter if the transmitted signal is pre-compensated at the transmitter. The simplest method to manage this process is to reduce the data rate to a suitable level since the instantaneous data rate is proportional to the allocated bandwidth. Based on our calculation, the connection will not be interrupted by heavy rain if the applied data rate does not exceed 100 Mbps.

7 Calculation of FSO connection outage probability in case of heavy rain

7.1 FSO channel model

The required minimum received power of the FSO link depends on the sensitivity of the optical detector, the allocated bandwidth, and the signal-to-noise ratio. Accordingly, the minimum required received power can be determined, see in [18], by equation (6).

$$P_{\text{req}} = NEP \cdot \sqrt{BW} \cdot SNR \quad (6)$$

where, NEP is photodetector noise equivalent power, BW is the applied bandwidth, and SNR is the minimum required signal-to-noise ratio, provided at the receiver. The required minimum signal-to-noise ratio depends on the type of modulation and the demanded bit error probability.

The effect of rain on the FSO link, i.e. the fading phenomenon on the propagating optical signal, can be demonstrated by outage probability. The magnitude of the received optical power varies depending on the intensity of the rainfall. In addition to increasing the total attenuation of an optical link, based on the recommendation of Kumar et. al, in [19], it can be taken into account that the structure parameter of the turbulent medium increases as a result of the rain. Our calculation is based on the modified Hufnagel-Valley (H-V) model (see in detail in [20]), which can be used adequately in heavy rain.

The fading margin of the optical connection can be determined by the ratio of the long-term average of the maximum signal power received in clear-sky, rain-free weather conditions and the required minimum received optical power. The amount of the fading margin is given by equation (7).

$$FM_{\text{FSO}}^{\text{[dB]}} = P_{\text{FSO rec-avg}}^{\text{[dBm]}} - P_{\text{FSO req}}^{\text{[dBm]}} \quad (7)$$

where $P_{\text{FSO rec-avg}}^{\text{[dBm]}} \Big|_{R_{\text{rain}}=0\text{mm/h}} = \mathbb{E}\{P_{\text{FSO rec}}^{\text{[dBm]}}\}$ is the average of the maximum received signal power. Therefore, the fading margin (FM) was calculated as the difference between $P_{\text{FSO rec-avg}}^{\text{[dBm]}}$ and $P_{\text{FSO req}}^{\text{[dBm]}}$.

The fading margin must be always greater than the highest level of rain attenuation, $FM_{\text{FSO}} \geq \max\{A_{\text{rain}}^{\text{[dB]}}\}$, where $A_{\text{rain}}^{\text{[dB]}}$ is the rain attenuation based on [21]. Accordingly, the value of the instantaneous received signal power above the threshold can be determined by the fading margin of the system and the instantaneous value of the attenuation caused by the rainy turbulent medium. The level of the average received power above the threshold value can be specified by equation (8).

$$\Delta_p^{\text{[dB]}} = P_{\text{FSO rec-inst.}}^{\text{[dBm]}} - P_{\text{FSO req}}^{\text{[dBm]}} - A_{\text{rain}}^{\text{[dB]}} \quad (8)$$

Note, that several options can be used to compensate for the effect of heavy rain. To effectively compensate, the current rain intensity and its short-term estimated value must be known. To compensate for the negative effect of rain, a closed-loop control system is required, which can pre-compensate the radiated optical signal according to the rainfall rate. Among several mitigation techniques, the most efficient is the accurate selection

of bandwidth. Accordingly, using a lower data rate results in bandwidth efficiency, a smaller allocated bandwidth. Our paper does not deal with the strongly destructive effect of fog, which can only be compensated with hybrid FSO-RF systems [22, 29].

7.2 FSO outage probability due to fade

The probability of FSO link outage was calculated by the cumulative distribution function $F(\gamma)$ of the signal-to-noise ratio ($\gamma_{\text{av opt}}$) measured at the receiver. It is defined as:

$$P_{\text{out FSO}} = P_r(\gamma_{\text{opt avg}} < \gamma_{\text{opt th}}) = F(\gamma_{\text{opt th}}) \quad (9)$$

and approximated by lognormal distribution as:

$$P_{\text{out FSO}} = 0.5 \left(1 + \operatorname{erf} \left(\frac{0.5\sigma_I^2 - \Phi_T}{\sqrt{2}\sigma_I} \right) \right) \quad (10)$$

In Equation (10) $\Phi_T = \ln \left(\frac{\gamma_{\text{opt avg}}}{\gamma_{\text{opt th}}} \right)$ is the SNR of average

and the threshold; $\sigma_I^2(R_{\text{Rain}})$ is the normalized irradiance variance, the ‘scintillation index’. The variance of the received signal level can be determined based on the modified structure parameter, which can be estimated based on the frequently used H-V model and with the Kumar’s addition [19]:

$$\begin{aligned} C_n^2(h) = & 5.94 \cdot 10^{-53} \left(\frac{v}{27} \right)^2 \cdot h^{10} \cdot e^{-\left(\frac{h}{1000}\right)} + \\ & + 2.7 \cdot 10^{-16} e^{-\left(\frac{h}{1500}\right)} + \\ & + A \cdot e^{-\left(\frac{h}{100}\right)} + R \cdot 10^{-16} \cdot e^{-\left(\frac{h}{1000}\right)} \end{aligned} \quad (11)$$

In equation (11) v is the wind speed, in [m/h], h is the altitude above sea level, in [m], A is the structure parameter at sea level, $C_n^2(h=0 \text{ m})$ in $[\text{m}^{-2/3}]$, and R is the rainfall rate in [mm/h]. The variance of the received signal is given by equation (12) as:

$$\sigma_I^2 = e^{\left(\frac{0.49\sigma_R^2}{(1+1.1\sigma_R^{12/5})^{7/6}} + \frac{0.51\sigma_R^2}{(1+0.69\sigma_R^{12/5})^{7/6}} \right)} - 1 \quad (12)$$

where, σ_R^2 is the Rytov variance.

8 Results of the impact of rain on FSO link

Our calculated result is depicted in Fig. 6. We confirm that the optical link can be significantly impacted by short-term heavy rainfall events that have occurred frequently in the last few years. It can be seen that the effect of heavy rains (up to roughly 100 mm/h) can only be compensated by optimally reduced data rate. Based on Fig. 6, it is concluded that FSO links longer than 2 km are more exposed to interruptions caused by rain, as seen in [23, 24].

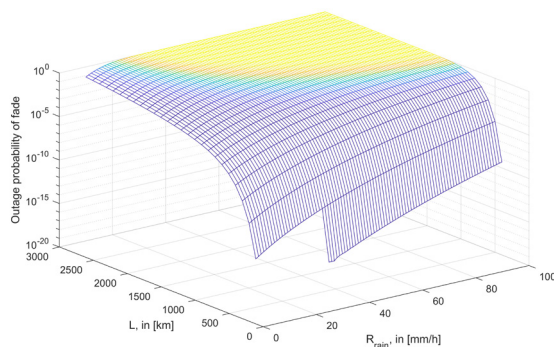


Figure 6: Outage probability of FSO link as a function of link distance L , and rainfall rate R_{rain} , with fade margin of $M_{FSO} = 25$ dB.

Nevertheless, we recommend avoiding long distance terrestrial optical links in Central Europe, where rain rates can exceed 50 mm/h and in short periods even may reach 100 mm/h [25].

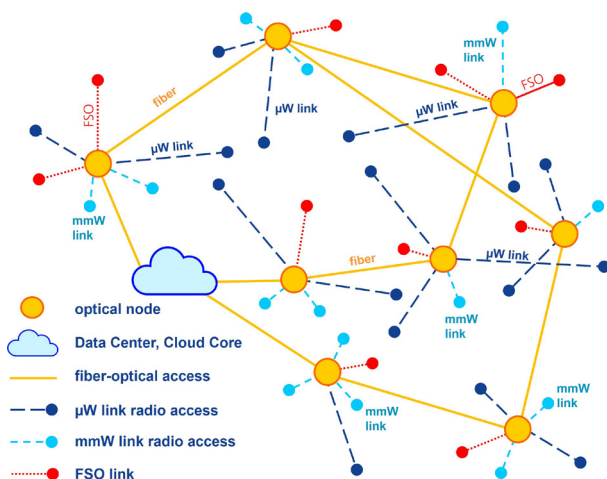


Figure 7: Meshed wireless RF/FSO network with fiber-optical backbone for 5G and future 6G access.

On the other hand, this restriction does not introduce a strict limitation for actual 5G and future beyond 5G anyhaul links. These access networks will use a mesh of

fiber-optical, RF (microwave and mmW) and FSO links [26-31]. As shown in Fig. 7, the longer connections are fiber-optical or microwave links [7, 28, 30]. FSO and mmW links are mainly used for the dense urban connections that are typically shorter than 2 km [3, 7, 15, 29, 31].

9 Conclusions

In our paper, the deterioration of terrestrial communication links as a result of increasingly frequent heavy rainfall events in recent years has been discussed in detail. Precise and adequately frequent measurement of instantaneous rain intensity is becoming more important from both scientific and economic point of view. In our article, an indirect rain intensity measurement method is presented, based on the received signal level fluctuation of the radio receiver used in a millimeter wave link. To determine the rain intensity, we used a short-range experimental radio hop operating in at 58 GHz. Based on the received signal level data of the mmW connection, the instantaneous rain intensity was determined. The applied computation process has been presented: first, the attenuation time series must be calculated in a calibrated mode, then the rain intensity data can be generated based on the attenuation time series. It was shown that the new method is suitable for the detection of rapid, instantaneous changes in rain intensity due to the high sampling rate. Among the many application possibilities of our results, we present a relevant type of adaptive communication, the effect of intense rain on FSO connections. It was shown that the increasingly frequent high-intensity precipitation events can significantly deteriorate the free-space optical connections. The quality of the optical connection is shown by determining the probability of fade. We recommended a basic planning guideline to avoid the harmful effects of very intensive rainfalls in Central European areas. Finally, some few words on our future topic: the 5G and 6G networks in the future will be mixed mesh networks. As a result, mm-wave links will enmesh our environment. Therefore, the high-precision rain measurement will be continuously available, by 5G and 6G stations installed on top of buildings. The end users will access the system via adaptive FSO/mm-wave links, thus ensuring optimized data connection. We plan to determine the availability of the system in the case of hybrid connections, adaptive FSO/mm-wave, by which the spectral efficiency of the system can be improved over a service territory.

10 Conflict of Interest

The authors declare no conflict of interest.

11 Acknowledgments

The authors thank Dr. Levente Dudás and Viktor Fehérvári for the useful discussions and help in the V-band experiments. The research has been supported by the National Research, Development and Innovation Fund of Hungary under the 2020-1.1.2-PIACI-KFI funding scheme.

12 References

1. J.C.Rodda, H.Dixon, "Rainfall measurement revisited", *Weather*, Vol.67, No.5, pp.131–136. 2012. <https://doi.org/10.1002/wea.875>
2. L.Csurgai-Horváth, I.Frigyes, J.Bitó, "Propagation and availability on E-band terrestrial radio", 6th European Conference on Antennas and Propagation, EUCAP, pp.73-76, Prague, Czech Republic, March 2012. <https://doi.org/10.1109/EuCAP.2012.6206539>
3. A.Hilt: "Throughput Estimation of K-zone Gbps Radio Links Operating in the E-band", *Informacije MIDEM, Journal* Vol.52, No.1, pp.29-39, Ljubljana, Slovenia, 2022. <https://doi.org/10.33180/InfMIDEM2022.104>
4. E.Vuerich, C.Monesi, L.G.Lanza, L.Stagi, E.Lanzinger, "Instruments and observing methods", report No.99. World Meteorological Organization. Italy, Germany, 10.2007-04.2009.
5. O.Goldshtein, H.Messer, A.Zinevich, "Rain rate estimation using measurements from commercial telecommunications links", *IEEE Transactions on Signal Processing*, Vol.57, No.4, pp.1616–1625, Jan. 2009. <https://doi.org/10.1109/TSP.2009.2012554>
6. Recommendation ITU-R P.838-3, "Specific Attenuation Model for Rain for Use in Prediction Methods", ITU, Geneva, Switzerland, 2005.
7. A.Hilt, "Microwave Hop-Length and Availability Targets for the 5G Mobile Backhaul", *IEEE 42nd Telecommunications and Signal Processing Conference*, Budapest, Hungary, 2019. <https://doi.org/10.1109/TSP.2019.8768870>
8. Nokia, Product Description, MetroHopper with FIU 19(E)/RRIC, C33512.85-F0, DN99592717, Issue 5-0 en, 2003.
9. A.Hilt, T.Pap, "Application of 58 GHz Band for GSM Access Networks in Hungary", *Proc. of the 11th MicroColl conference*, Budapest, Hungary, 2003. <https://hdl.handle.net/10890/16318>
10. Recommendation ITU-R P.525-4, "Calculation of free-space attenuation", P Series, Radiowave propagation, ITU, Geneva, Switzerland, Aug. 2019.
11. Recommendation ITU-R P.676-13, "Attenuation by atmospheric gases and related effects", P Series, Radiowave propagation, ITU, Geneva, Switzerland, Aug. 2022.
12. MetNet Hungary Ltd., <https://www.metnet.hu/>
13. L.Csurgai-Horváth, "Receiver station in Budapest for Q/V band satellite site diversity and adaptive coding and modulation experiments with Alphasat", *International Journal on Satellite Communication Networking*, Vol.37, pp.149–162, 2019. <https://doi.org/10.1002/sat.1270>
14. H.Li, J.Zhang, Q.Hong, H.Zheng, J.Zhang, "Exploiting adaptive modulation in E-band software-defined backhaul network", 8th Annual Computing and Communication Workshop and Conference, pp.1009–1013, Las Vegas, USA, January 2018.
15. A.Hilt: "Gbit Radios for the Mobile Anyhaul", 25th Seminar on Radio Communications, SRK'2022, pp.505-515, ISBN: 978-961-243-433-5, Ljubljana, Slovenia, <https://hdl.handle.net/10890/16800>.
16. S.A.Al-Gailani, A.B.Mohammad, R.Q.Shaddad, "Enhancement of free space optical link in heavy rain attenuation using multiple beam concept", *Optik*, Vol.124, No.21, pp.4798-4801, ISSN 0030-4026, 2013. <https://doi.org/10.1016/j.ijleo.2013.01.098>
17. U.A.Korai, L.Luini, R.Nebuloni, "Model for the Prediction of Rain Attenuation Affecting Free Space Optical Links", *MDPI Electronics*, Vol.7, No.12, 407. 2018. <https://doi.org/10.3390/electronics7120407>
18. V.Mackowiak, J.Peupelmann, Y.Ma, A.Gorges, "NEP-noise equivalent power", Thorlabs Inc., 56, 2015.
19. S.Kumar, P.Arora, "Modeling C2n by Inclusion of Rainfall Parameter and Validate Modified Log Normal and Gamma-Gamma Model on FSO Communication Link", *Journal of Optical Communications* 2019. <https://doi.org/10.1515/joc-2019-0247>
20. L.C.Andrews, R.L.Phillips, "Laser Beam Propagation Through Random Media", 2nd edition, SPIE Press, Bellingham, Washington, USA 2005.
21. Report ITU-R F.2106-1, "Fixed service applications using free-space optical links", F Series, Fixed service, ITU, Geneva, Switzerland, Nov. 2010.
22. M.Lapčák, L.Ovseník, N.Zdravecký, J.Orave S.Andrejčík, "Deep data analysis methods applied to hard switching in hybrid FSO/RF systems", *IEEE 33rd International Conference Radioelektronika*, pp.1-6, Pardubice, Czech Republic, Apr. 2023. <https://doi.org/10.1109/RADIOELEKTRONIKA57919.2023.10109039>

23. W.Zhan, Z.Hao, R.Li, et al., "Influence mechanism of repetition frequency on pulse position modulation in deep space laser communication", Cluster Comput 22 (Suppl 6), pp.14451–14460, 2019.
<https://doi.org/10.1007/s10586-018-2313-x>
24. A.Farkasvölgyi, I.Frigyes, "Correlation Problems in Optical Multichannel Systems in Satellite Communication", IEEE Photonics & Electro-magnetics Research Symposium – Spring, PIERS-Spring pp.902-907, 2019.
<https://doi.org/10.1109/PIERS-Spring46901.2019.9017666>
25. M.Lakatos, L.Hoffmann, "Increasing trend in short term precipitation and higher return levels due to climate change", in Országos Települési Csapadékviz-gazdálkodási Konferencia (in Hungarian), Cum Scientia pro Aquis Hungariae, 2017, pp.8-16, ISBN 978-615-5845-21-5.
26. A.K.Garg, V.Janyani, B.Batagelj, N.H.Z.Abidin, M.H.A.Bakar, "Hybrid FSO/fiber optic link based reliable & energy efficient WDM optical network architecture," Optical Fiber Technology, Vol.61, 2021, p.102422,
<https://doi.org/10.1016/j.yofte.2020.102422>
27. A.Hilt, "Feasibility of D-band Fixed Radio Links for 5G and Beyond Access Networks", IEEE 34th International Conference Radioelektronika, pp.1-6,
<https://doi.org/10.1109/RADIOELEKTRONIKA61599.2024.10524063>.
28. M.A.Ilgaz, A.Lavrič, B.Batagelj, M.Vidmar, "Centralized Millimeter-Wave Opto-Electronic Oscillator", Photonics North (PN) 2020.
29. E.Leitgeb, "Optical Wireless Technologies as Upgrade and Extension to Traditional RF for Communications and Sensing", IEEE 34th International Conference Radioelektronika, Žilina, Slovak Republic, April 2024.
30. A.Fayad, T.Cinkler, J.Rak, M.Jha, "Design of cost-efficient optical fronthaul for 5G/6G networks: An optimization perspective", MDPI Sensors, Vol.22, No.23, p.9394, Dec. 2022.
<https://doi.org/10.3390/s22239394>
31. P.Poornachari, K.Palanichamy, G.Madan M, A.P. Samathuvamani, "Simulations of Mode Division Multiplexed Free Space Optics with Photonics Traversal Filter using Multi-Mode Fiber", Informacije MIDEM Journal, Vol.51, No.4, pp.207-213, Ljubljana, Slovenia, 2021.
<https://doi.org/10.33180/InfMIDEM2021.401>



Copyright © 2024 by the Authors.
This is an open access article distributed under the Creative Commons Attribution (CC BY) License (<https://creativecommons.org/licenses/by/4.0/>), which permits unrestricted use, distribution, and reproduction in any medium, provided the original work is properly cited.

Arrived: 16. 04. 2024

Accepted: 22. 05. 2024

Aerosol-Deposition-Derived Graphite Thick Films for Electrochemical Sensors

Matej Šadl¹⁺, Barbara Repič^{1,2,+}, Ivana Goričan^{1,2}, Danjela Kuščer^{1,2} and Hana Uršič^{1,2}

¹Electronic Ceramics Department, Jožef Stefan Institute, Ljubljana, Slovenia

²Jožef Stefan International Postgraduate School, Ljubljana, Slovenia

⁺M.Š. and B.R. contributed equally

Abstract: Disposable electrochemical (EC) sensors are usually manufactured by screen printing and post-deposition temperature curing of the sensor's components. However, complete removal of an organic vehicle requires curing at temperatures of a few hundred °C, which can lead to electrode-substrate incompatibilities and limit the choice of material. In this work, graphite thick-film electrodes without additives were deposited on polyimide substrates at room temperature using the aerosol-deposition method. The resulting thick films had good adhesion, a defect-free surface, a thickness of a few micrometers, a root-mean-square roughness of 0.68 μm and sheet resistance of 27 Ω/sq. Scanning electron microscopy of the film surface revealed good particle compaction, while the X-ray diffraction analysis showed no peak broadening of the graphite thick films, which indicates a different deposition mechanism than that normally observed for ceramic powders. The EC properties of the graphite working electrodes were evaluated using cyclic voltammetry. The graphite films showed a low capacitive current of 0.114 mA, good reversibility of the redox process, a high EC active surface area of 1.44 cm²/cm_{geo}² and a standard heterogeneous electron-transfer-rate constant of 0.0019 cm·s⁻¹. The aerosol-deposited graphite thick-film electrodes show potential for the EC detection of a broad range of chemicals.

Keywords: graphite electrode; electrochemical detection; aerosol deposition; room-temperature process; polyimide foil

Debele plasti grafita nanešene v aerosolu za elektrokemijske senzorje

Izvleček: Elektrokemijski (EK) senzorji za enkratno uporabo se običajno izdelujejo tako, da komponente senzorja natisnemo s sitotiskom ter jih nato temperaturno obdelamo. Za popolno odstranitev organskega nosilca je plasti potrebno segreti do nekaj sto °C, kar lahko privede do nezdružljivosti med elektrodo in podlago ter omeji izbiro materiala. V tej raziskavi smo z metodo nanosa plasti v aerosolu pri sobni temperaturi pripravili debeloplastne grafitne elektrode brez dodatkov na poliimidne podlage. Tako pripravljene debele plasti se dobro držijo podlage, imajo površino brez vidnih defektov, debelino nekaj mikrometrov, hrapavost 0.68 μm in plastno upornost 27 Ω/sq. Z vrstično elektronsko mikroskopijo smo na površini plasti opazili kompaktno strukturo delcev. Pri rentgenski difrakciji debelih plasti grafita ne zaznamo širitve vrhov, kar nakazuje, da je mehanizem nanašanja pri grafitu drugačen kot je običajno za keramični prah. EK lastnosti grafitnih delovnih elektrod smo analizirali s ciklično voltametrijjo. Grafitne plasti izkazujejo nizek kapacitivni tok z vrednostjo 0.114 mA, dobro reverzibilnost redoks procesa, veliko EK aktivno površino z vrednostjo 1.44 cm²/cm_{geo}² in visok standardni koeficient heterogene reakcije z vrednostjo 0.0019 cm·s⁻¹. Debeloplastne grafitne elektrode pripravljene z metodo nanosa plasti v aerosolu so primerne za EK detekcijo številnih kemikalij.

Ključne besede: grafitna elektroda; elektrokemijska detekcija; metoda nanašanja plasti v aerosolu; priprava pri sobni temperaturi; poliimidna folija

* Corresponding Author's e-mail: hana.ursic@ijs.si, danjela.kuscer@ijs.si

1 Introduction

The amount of research on electrochemical (EC) sensors is increasing owing to the requirement for the

point-of-care and on-site detection of various compounds such as pharmaceuticals, pesticides, toxins and heavy metals [1]–[8]. These are widely utilized in agri-

How to cite:

M. Šadl et al., "Aerosol-Deposition-Derived Graphite Thick Films for Electrochemical Sensors", Inf. Midem-J. Microelectron. Electron. Compon. Mater., Vol. 54, No. 3(2024), pp. 177–186

culture and the food industries as well as in environmental and biomedical applications. The applications for disposable EC sensors dictate many requirements: good selectivity and sensitivity for a broad range of EC active species, reproducibility of the results, miniature and portable systems, ease of use and cost-effective production with easy scale-up possibilities [8]–[11].

The EC sensors consist of three electrodes, i.e., the counter, reference and working electrode (WE). In disposable EC sensors the electrodes are integrated on selected substrates, commonly by screen printing and the subsequent firing of the deposited layers at elevated temperatures. The WE is a key component and should have high electrical conductivity and a high specific surface area.

Screen printing is the most commonly used method for depositing films that are typically a few tens of μm thick. It is a mature, commercially available technology, which offers patterning of the structures with good reproducibility on laboratory and industrial scales [11]–[14].

Although the screen-printing method is widely adopted, there are some challenges that need to be considered. In printing techniques, the ink or paste consists of a solid material dispersed in an organic vehicle. To obtain good functional properties of the thick film, the organic vehicle must be removed during the processing. To remove the organic vehicle and to densify the thick film, a temperature of a few hundred $^{\circ}\text{C}$ is needed [14], [15]. Due to the degradation of carbon in air, annealing at higher temperatures requires an inert atmosphere [16]. However, high-temperature curing can lead to electrode-substrate incompatibilities, which significantly limit the choice of substrate materials. To avoid this shortcoming, the EC active materials should be deposited at low temperature and without additives.

The aerosol deposition (AD) method, sometimes known as powder aerosol deposition, enables the direct deposition of functional materials in the form of micrometre-sized dry powders without the use of additives [17]. The deposition mechanism is based on the impact of the particles, and the film's consolidation occurs at room temperature, due to the high kinetic energy of the sprayed particles [18]–[21]. AD is a room-temperature process that enables the integration of functional materials on low-melting point and flexible substrates [22]–[25]. As a result, AD offers good material compatibility. It is generally used for the deposition of ceramic films, but metals can also be deposited. However, research on metal deposition is still in its beginnings. So far, the following materials have been deposited using AD: Cu [26], [27], Ag [28], [29], Al [30],

[31], Fe [32] Fe-based amorphous alloys [33], $(\text{Bi,Sb})_2\text{Te}_3$ [34], [35], rare-earth magnets [36], [37] and graphite [38].

Carbon-based materials are commonly used as the WE in EC sensors. They are non-toxic, low-cost, have high electrical conductivity and allow the detection of various compounds such as pharmaceuticals, pesticides, toxins and heavy metals [39]–[43].

In this study we processed a few- μm -thick graphite films on a polyimide substrate by AD at room temperature and without any post-deposition curing. The graphite thick films were structurally and microstructurally characterized using contact profilometry, X-ray diffraction, atomic force microscopy and scanning electron microscopy. Their EC properties were investigated by cyclic voltammetry. The purpose was to study the properties of graphite thick films prepared by a relatively new AD method and to assess the suitability of the aerosol-deposited thick films for use in EC applications.

2 Materials and methods

A commercially available graphite powder (graphite flake, 99.8 %, 043209, Alfa Aesar) was sieved through a mesh (with 80- μm openings) and vacuum dried at 80 $^{\circ}\text{C}$, before being aerosol deposited (AD) onto the substrate. A commercially available polyimide (PI) foil (Kapton HN, DuPont, DE, USA) with a thickness of 125 μm was used as a substrate. The AD equipment was provided by InVerTech, Germany. A schematic of the AD setup is shown in [44]. During the AD the process parameters (Table 1) were kept constant. After the film's deposition the thick-film samples were cleaned by gently blowing them with air.

Table 1: Process parameters used during the AD.

Process parameter	Value
Pressure in the deposition chamber	90 mbar
Pressure in aerosol chamber	0.6 mbar
Nozzle geometry (slit size)	$(0.5 \cdot 10) \text{ mm}^2$
Carrier gas species	N_2
Gas flow rate	$1 \text{ L} \cdot \text{min}^{-1}$
Distance between nozzle and substrate	5 mm
Sweep speed	$5 \text{ mm} \cdot \text{s}^{-1}$

The particle size distribution of the initial graphite powder was determined in isopropanol using a light-scattering laser granulometer (S3500, Microtrac, PA, USA).

The X-ray diffraction (XRD) analysis was performed with a benchtop X-ray diffractometer (MiniFlex 600-C, Rigaku, Japan) using Cu-K α radiation. Diffraction patterns were recorded in the Bragg–Brentano geometry using a silicon strip detector (D/teX Ultra) in a 2θ range of 10° – 60° with a step of 0.01° and 0.06 s/step. The software X'Pert HighScore Plus 3.0e (PANalytical, Almelo, The Netherlands) was used to analyse the XRD patterns and strip the Cu-K α_2 component.

The microstructures of the graphite powder and the surface of the graphite thick films were analysed using a field-emission scanning electron microscope (FE-SEM, JSM 7600F, Jeol, Japan), equipped with secondary electron and backscattered electron detectors. Before the analysis, the graphite powder was spread on the carbon tape.

The topography of the graphite thick films was analysed using contact stylus profilometry (DektakXT, Bruker, MA, USA) and atomic force microscopy (AFM, MFP-3D, Asylum Research, CA, USA). The thickness and root-mean-square surface roughness (R_q) of the thick films were evaluated from a line profile measured with a contact profilometer using the software Vision64 (Bruker, MA, USA). The thickness was evaluated from the step height of the film after curvature removal using a quadratic polynomial. R_q was evaluated from the 2-mm roughness profile (length of 2 mm) obtained after filtering the total profile using Gaussian regression (cut off 0.8 mm). In the AFM analysis a Si tip on a Si/Al cantilever with a diameter of ~ 7 nm (AC240TSR3, Asylum Research, CA, USA) was used for scanning in AC topography mode. The root-mean-square surface roughness R_q^{AFM} was also evaluated from the AFM map scans (with dimensions $80\text{ }\mu\text{m} \times 80\text{ }\mu\text{m}$).

The sheet resistance (R_s) of the thick films was measured using the four-point probe technique, with the probes arranged equidistantly in a line. The R_s of the thick film was calculated from the measured voltage drop between the two inner probes and the current. A correction factor of 0.795 was used [45].

EC experiments were performed using a potentiostat-galvanostat (Multi Autolab M 204, Methrom, The Netherlands) controlled by Nova 2.1.5 software. A conventional three-electrode cell configuration was used. The graphite thick films processed by AD were used as the WE, together with a conventional Ag/AgCl reference electrode and a platinum-sheet counter electrode (both from Methrom). The measurements were carried out in deaerated solutions at 25°C . Cyclic voltammograms were measured between -0.2 V and 0.6 V at a constant scan rate (ν) of 20, 50, 100, 200 and $500\text{ mV}\cdot\text{s}^{-1}$. The measurements were performed in a 0.1-M phos-

phate buffer solution (PBS) used as an electrolyte and in a 0.005-M equimolar solution of $\text{Fe}(\text{CN})_6^{3-/4-}$ (HCF) as a redox probe dissolved in the PBS. The voltammograms measured at $100\text{ mV}\cdot\text{s}^{-1}$ were characterized to determine the capacitive current (i_{cap}) in the PBS, the peak-to-peak separation (ΔE_{pp}) and the cathodic-to-anodic peak current ratio ($i_{\text{pc}}/i_{\text{pa}}$) in HCF. From the measurements at different scan rates, the electrochemically active surface area was determined from the slope of the linear dependence of the peak current as a function of the square root of the scan rate using the Randles–Ševčík equation. It was normalised using the geometric surface area to obtain a real electrochemically active surface area (A_{eCSA}) [9]. Cyclic voltammograms recorded at different scan rates were also used to determine a standard heterogeneous electron-transfer-rate constant (k^0) using the Nicholson method [46], in which the k^0 of a quasi-reversible reaction is related to a dimensionless kinetic parameter (ψ), calculated as a function of ΔE_{pp} at different scan rates. The electrodes were also used to determine operating potential window (OPW), which was assessed based on the qualitative inspection of a series of cyclic voltammograms, obtained by incrementally increasing or decreasing the vertex potential of the sweep range in 0.05-V increments. The limits of the OPW are identified as the potential at which the current intensity was in the same range as the peak current of the redox probe.

The mechanical stability of the graphite thick films was additionally tested by immersing and rinsing them in organic solvents, i.e., methanol, ethanol and acetone.

3 Results

The graphite powder, which resulted in few-micrometer-thick films, was analysed using laser granulometry and SEM. The volumetric particle size distribution of the graphite powder measured by laser granulometry is shown in Figure 1(a). The distribution is monomodal with the particle size ranging between $1.6\text{ }\mu\text{m}$ and $148\text{ }\mu\text{m}$. The median (d_{50}) particle size is $16.6\text{ }\mu\text{m}$, represented by an orange vertical line. For the successful AD of ceramics, the typically reported particle size is between $0.2\text{ }\mu\text{m}$ and $2\text{ }\mu\text{m}$ [18]. Also for the AD of metals, the particle size window for a successful deposition is between $1\text{ }\mu\text{m}$ and $10\text{ }\mu\text{m}$ [30], [47]. However, in our case the AD of graphite powder was successful using much larger particles than typically used in AD. In the literature, there are not many reports that show a successful AD using particles with d_{50} larger than $10\text{ }\mu\text{m}$. These cases are limited to Nd-Fe-B magnets [37], MAX phase materials [48] and glass [49].

The SEM micrographs, taken with a secondary-electron detector in Figure 1(b, c), reveal the morphology of the graphite powder. Figure 1(b) shows large, agglomerated particles with round-shaped surfaces. The agglomerates exceed 40 μm in diameter (red dashed

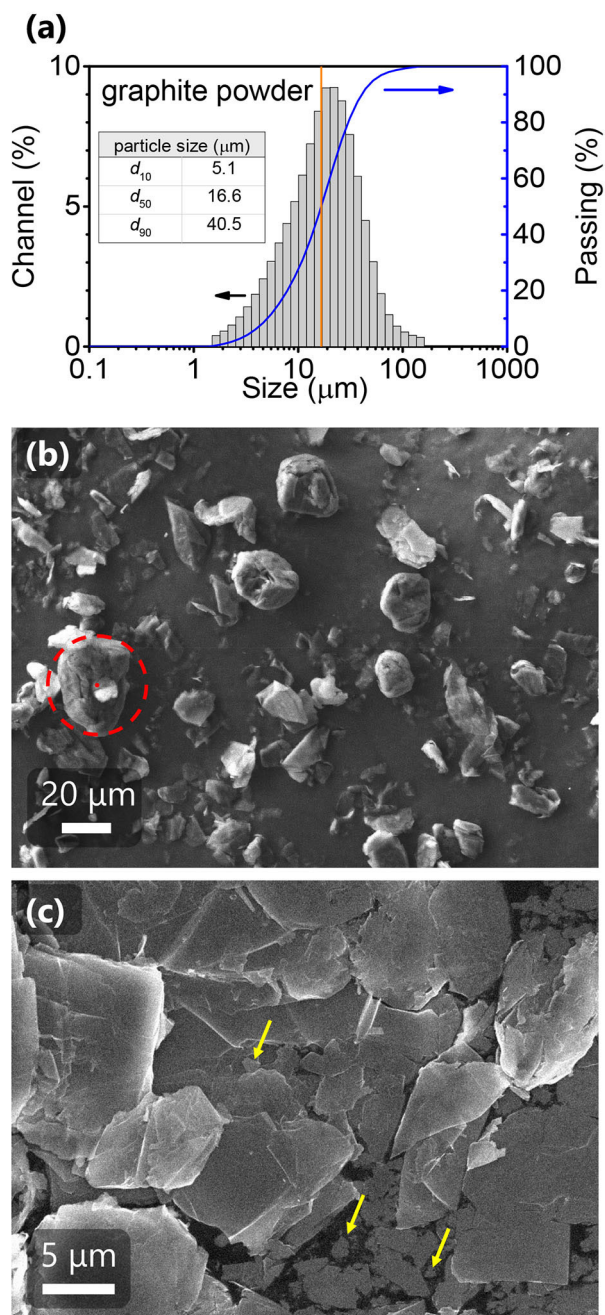


Figure 1: Analysis of the graphite powder. (a) Volumetric particle size distribution (grey) and cumulative curves (blue) evaluated from the laser granulometry. The vertical orange line represents the median (d_{50}) particle size. The d_{10} , d_{50} and d_{90} are also displayed in the inset table. (b, c) SEM images taken with a secondary-electron detector. The red dashed circle with diameter of 40 μm marks a large agglomerate, while the smallest particles, around 1 μm , are marked with yellow arrows.

circle). The agglomeration is in agreement with the laser granulometry data (Figure 1(a)). On the other hand, Figure 1(c) shows particles that have an irregular shape, including plate-like surfaces that indicate the easy cleavage of the graphite flake-type particles. The smallest particles are of the order of 1 μm .

The AD of the graphite powder on a PI substrate was successful, resulting in good adhesion of the film to the substrate and defect-free appearance of the film's surface, as seen in Figure 2(a). A line scan across the deposited film is shown in Figure 2(b) and reveals an even film thickness of 4.4 μm . The root-mean-square roughness (R_q) reaches 0.68 μm , which is at least 3-times higher than reported for Al_2O_3 films and ceramic-metal (Al_2O_3 -Al) multilayered thick films prepared by AD [18], [30]. A high surface roughness indicates a high specific surface area, which is advantageous in EC sensing applications. Note that after the AD the graphite film is still susceptible to abrasion. The sheet resistance (R_s) of 27 Ω/sq confirmed sufficient conductivity of the film for the EC measurement. The resistance is comparable to that of screen-printed conductive carbon films [50].

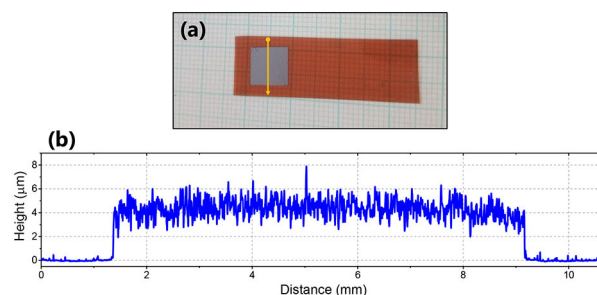


Figure 2: (a) Photograph of the deposited graphite thick film on a PI substrate. The orange line represents the position of the line scan. (b) Line profile measured by contact profilometry.

The XRD patterns of the graphite powder and deposited thick films are shown in Figure 3. Both powder and film contain a graphite phase (PDF 075-2078) [51], with the most prominent reflection (002) at 2θ of 26.5° . Note that the powder also contains a trace amount of some other graphite phase, which overlaps with the (002) reflection. After the deposition, the peak position of the graphite phase does not change and the peak width does not increase. This shows that there is no crystallite size reduction and build-up of microstrain due to the impacting particles, which is typically observed in the deposition of ceramic thick films [23], [52]. The XRD pattern of the graphite film also contains additional peaks and an increased background level arising from the PI substrate.

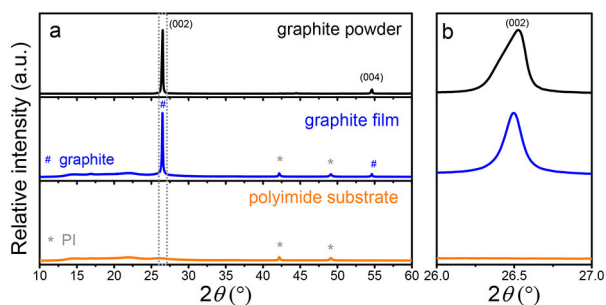


Figure 3: XRD patterns of the graphite powder (black), graphite thick film (blue) and blank PI substrate (orange). (a) XRD patterns in 2θ range 10° – 60° , (b) close-up view of the region of the most intense graphite peak.

The surface topography of the graphite thick films was analysed using AFM (Figure 4) and SEM (Figure 5). Figure 4(a, b, c) shows the AFM height, deflection and tapping amplitude modes, respectively. The height image (Figure 4(a)) shows obvious craters, which contribute to the high R_q^{AFM} , reaching $0.48\ \mu\text{m}$. Both the AFM and SEM images reveal irregularly shaped particles. An interesting observation is the straight features (yellow arrows in Figure 4 and Figure 5(b)) that resemble sharp-edged particles, which indicates the flake-like nature of the deposited graphite film. From the SEM surface view, good particle compaction can be observed. In particular, the SEM image taken with a backscattered-electron detector (Figure 5(b)) reveals no clear pores or voids between the deposited particles. The backscattered-electron detector is very appropriate for evaluating the film's homogeneity as it gives a high contrast between the compact and porous regions.

An EC analysis of the graphite thick-film WE was made by cyclic voltammetry (Figure 6). The voltammogram measured in the PBS shows a low background with an i_{cap} of $0.114\ \text{mA}$, determined as the difference between cathodic and anodic currents at $0.2\ \text{V}$. For the characterization of the voltammogram recorded in HCF, we determined the anodic (i_{pa}) and cathodic peak currents (i_{pc}), which were corrected with capacitive currents measured in the PBS at the same potentials. The currents observed in both the PBS and HCF are higher than those observed for commercially available, screen-printed electrodes [9], or screen-printed graphite-based WEs [53], [54]. From the $i_{\text{pc}}/i_{\text{pa}}$ ratio of 0.99 , we can confirm the good reversibility of the redox process. From the anodic (E_{pa}) and cathodic peak potentials (E_{pc}), we determined an ΔE_{pp} of $176\ \text{mV}$ as the absolute difference between the two values, indicating that this redox couple exhibits a quasi-reversible behaviour at the graphite electrode prepared by AD [54].

The EC response of the WE at different scan rates is shown in Figure 7(a). According to the Randles-Ševčík

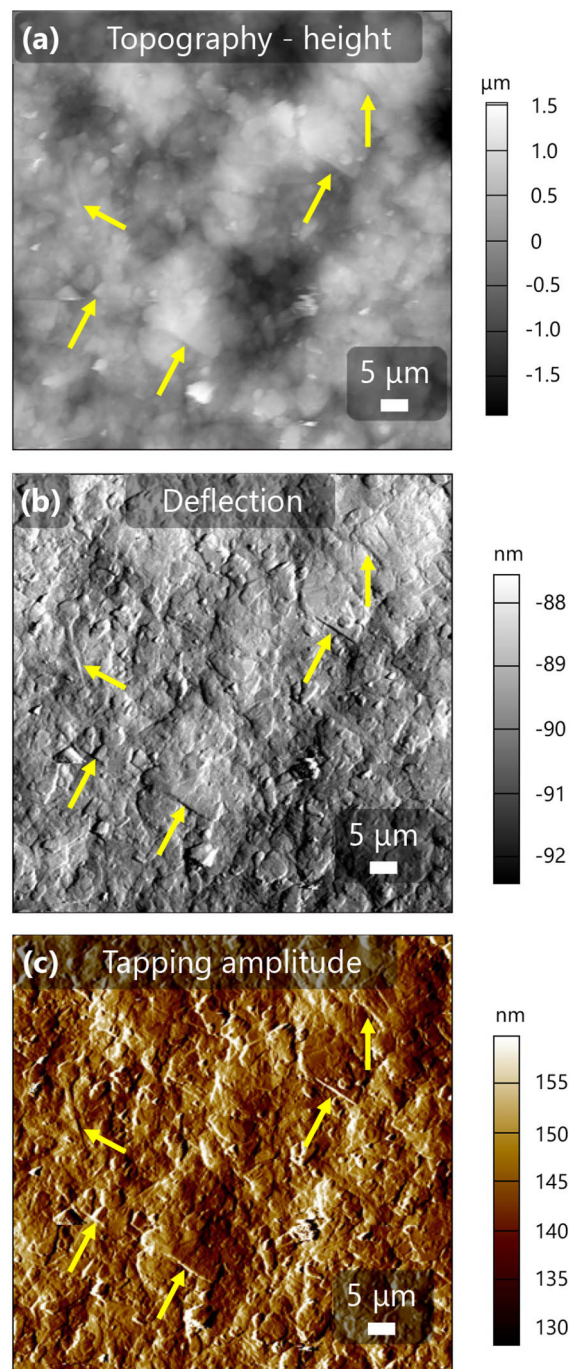


Figure 4: AFM map scans of the surface of graphite thick films. (a) height, (b) deflection, and (c) tapping amplitude. Yellow arrows designate sharp edges of the flake-like particles.

equation, the peak current is proportional to A_{ecsa} , which can in turn be calculated from the slope of the linear relationship between i_{pc} or i_{pa} and square root of the scan rate, shown in Figure 7(b). The data shows good linearity for both peak currents, but slightly different slopes. A_{ecsa} was calculated for both peaks, and their average value was $1.44 \pm 0.06\ \text{cm}^2/\text{cm}_{\text{geo}}^2$. This value is higher than the screen-printed graphite electrode

($0.79 \text{ cm}^2/\text{cm}_{\text{geo}}^2$) [54]. The increase in A_{ecsa} could be attributed to the high surface roughness of the graphite thick films prepared by AD.

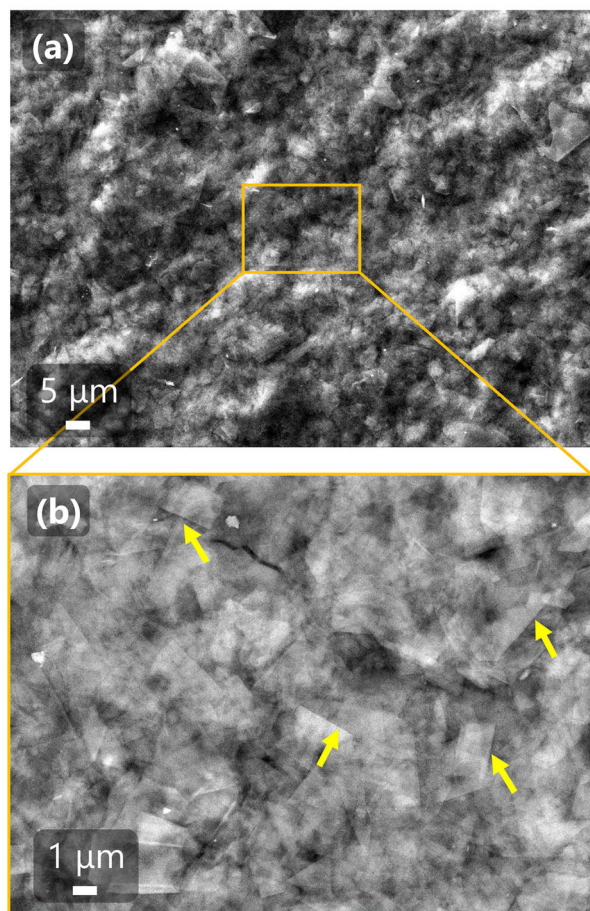


Figure 5: The SEM images of the graphite thick film in surface view. The micrographs in (a) and (b) were taken with secondary-electron and backscattered-electron detector, respectively. Yellow arrows designate sharp edges of flake-like particles.

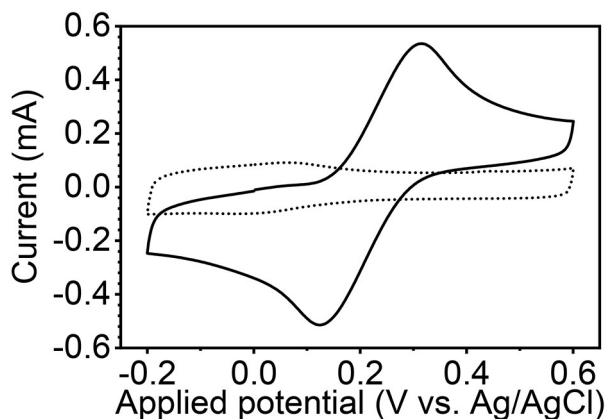


Figure 6: Cyclic voltammograms at $100 \text{ mV} \cdot \text{s}^{-1}$ of PBS (dotted line) and HCF (full line) at graphite thick-film WE.

Since the ΔE_{pp} of the quasi-reversible process changes with the scan rate, we used cyclic voltammograms measured at different scan rates to plot how a dimensionless kinetic parameter Ψ varies with the inverse square root of the scan rate, as shown in Figure 7(c). A k^0 of $1.9 \cdot 10^{-3} \text{ cm} \cdot \text{s}^{-1}$ was then calculated from the slope by the Nicholson method at $v = 20\text{--}500 \text{ mV} \cdot \text{s}^{-1}$ ($\Delta E_{\text{pp}} = 122\text{--}354 \text{ mV}$). Although the ΔE_{pp} at the highest scan rate used exceeds the range for which the Nicholson method is valid, all points show good linearity. Compared to values reported by Trachioti et al. [54] for graphite screen-printed electrodes, we obtained similar k^0 values. To determine in which potential range the

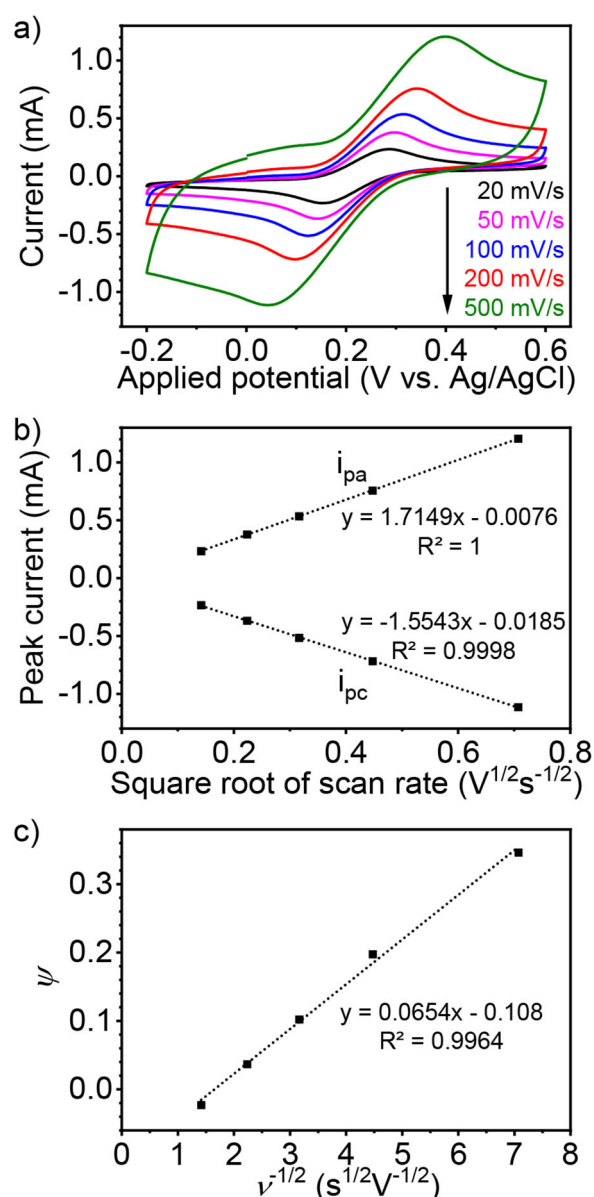


Figure 7: (a) Cyclic voltammograms of various scan rates of HCF for graphite thick-film WE, (b) plot of cathodic and anodic peak currents of HCF as a function of the square root of the scan rate, (c) plot of Ψ vs. $v^{-1/2}$ for the reduction of HCF.

electrode has a stable response, we also determined its OPW, which is from -0.9 V to 1.2 V. Electrode stability in the anodic direction makes it very suitable for the detection of phenolic compounds such as bisphenol A [6], dihydroxybenzene isomers such as hydroquinone, catechol and resorcinol [7], parabens [55], quinolone antibiotics [56], organohalides [57], as well as 4-nitrophenol and dopamine [58]. The graphite thick films were also mechanically stable and did not degrade or delaminate from the substrate when immersed in and rinsed with methanol, ethanol or acetone. Therefore, the films can also be used for the detection of analytes that require non-aqueous electrolytes. We can conclude that AD graphite thick films are applicable as working electrodes in EC sensors for the detection of various organic compounds.

4 Conclusions

To avoid high temperatures in the fabrication of EC sensors, the AD method was used to process graphite thick films on PI substrates. The initial graphite powder consists of flake-type particles with an irregular shape that form large agglomerates. The powder particle size distribution shows a rather large d_{50} particle size of $16.6\ \mu\text{m}$, which is rarely reported for the AD method. However, AD was successful and resulted in $\sim 4\text{-}\mu\text{m}$ -thick films with a defect-free appearance and an R_q of $0.68\ \mu\text{m}$. The SEM revealed good particle compaction of the film surface. The XRD patterns showed no reduction in the crystallite size and no increase in the microstrain after deposition. The graphite is therefore not subjected to the same deposition mechanism that is typical for ceramics. An EC analysis by cyclic voltammetry showed good reversibility of the redox process for graphite working electrodes with a large, real A_{ecs} of $1.44\ \text{cm}^2/\text{cm}_{\text{geo}}^2$ and a k^0 of $0.0019\ \text{cm}\ \text{s}^{-1}$, comparable to those reported for graphite in the literature. A reasonable OPW between -0.9 V and 1.2 V also enables their use as working electrodes for the EC detection of a broad range of chemicals.

5 Acknowledgments

This work was funded by the Slovenian Research and Innovation Agency (research project N2-0212, J2-3049, and research core funding P2-0105), Ministry of Higher Education, Science and Innovation of Republic Slovenia (C3360-23-252004, M-ERA.NET) and the Jožef Stefan Institute Director's fund 2017-ULTRACOOL. The authors thank K. Spanou, N. Suban and V. Fišinger for assistance in the laboratory.

6 Conflict of interest

The authors declare no conflict of interest. The founding sponsors had no role in the design of the study; in the collection, analyses, or interpretation of data; in the writing of the manuscript, and in the decision to publish the results.

7 References

1. J. Baranwal, B. Barse, G. Gatto, G. Broncova, and A. Kumar, "Electrochemical Sensors and Their Applications: A Review," *Chemosensors*, vol. 10, no. 9, p. 363, 2022, <https://doi.org/10.3390/chemosensors10090363>.
2. G. Maduraiveeran and W. Jin, "Nanomaterials based electrochemical sensor and biosensor platforms for environmental applications," *Trends Environ. Anal. Chem.*, vol. 13, pp. 10–23, 2017, <https://doi.org/10.1016/j.teac.2017.02.001>.
3. K. Ashley, "Developments in electrochemical sensors for occupational and environmental health applications," *J. Hazard. Mater.*, vol. 102, no. 1, pp. 1–12, 2003, [https://doi.org/10.1016/S0304-3894\(03\)00198-5](https://doi.org/10.1016/S0304-3894(03)00198-5).
4. Y. Wang, H. Xu, J. Zhang, and G. Li, "Electrochemical Sensors for Clinic Analysis," *Sensors*, vol. 8, no. 4, pp. 2043–2081, 2008, <https://doi.org/10.3390/s8042043>.
5. Z. Shi, L. Xia, and G. Li, "Recent Progress of Electrochemical Sensors in Food Analysis," *Chemosensors*, vol. 11, no. 9, p. 478, 2023, <https://doi.org/10.3390/chemosensors11090478>.
6. A. C. de Sá et al., "Flexible Carbon Electrodes for Electrochemical Detection of Bisphenol-A, Hydroquinone and Catechol in Water Samples," *Chemosensors*, vol. 8, no. 4, p. 103, 2020, <https://doi.org/10.3390/chemosensors8040103>.
7. M. M. I. Khan, M. A. Yousuf, P. Ahamed, M. Alaudin, and N. T. Tonu, "Electrochemical Detection of Dihydroxybenzene Isomers at a Pencil Graphite Based Electrode," *ACS Omega*, vol. 7, no. 33, pp. 29391–29405, 2022, <https://doi.org/10.1021/acsomega.2c03651>.
8. J. P. Metters, R. O. Kadara, and C. E. Banks, "New directions in screen printed electroanalytical sensors: an overview of recent developments," *Analyst*, vol. 136, no. 6, p. 1067, 2011, <https://doi.org/10.1039/c0an00894j>.
9. R. O. Kadara, N. Jenkinson, and C. E. Banks, "Characterisation of commercially available electrochemical sensing platforms," *Sensors Actuators, B Chem.*, vol. 138, no. 2, pp. 556–562, 2009, <https://doi.org/10.1016/j.snb.2009.01.044>.

10. R. Umaphathi, S. M. Ghoreishian, S. Sonwal, G. M. Rani, and Y. S. Huh, "Portable electrochemical sensing methodologies for on-site detection of pesticide residues in fruits and vegetables," *Coord. Chem. Rev.*, vol. 453, p. 214305, 2022, <https://doi.org/10.1016/j.ccr.2021.214305>.
11. C. E. Banks, C. W. Foster, and R. O. Kadara, *Screen-Printing Electrochemical Architectures*. Cham: Springer International Publishing, 2016.
12. R. A. Dorey, *Ceramic Thick Films for MEMS and Microdevices*. Oxford: Elsevier, 2012.
13. D. Kuscer, "Screen Printing," in *Encyclopedia of Materials: Technical Ceramics and Glasses*, vol. 1, Elsevier, 2021, pp. 227–232, <https://doi.org/10.1016/B978-0-12-803581-8.12082-X>.
14. M. Kosec, D. Kuscer, and J. Holc, "Processing of Ferroelectric Ceramic Thick Films," in *Multifunctional Polycrystalline Ferroelectric Materials*, Dordrecht: Springer, 2011, https://doi.org/10.1007/978-90-481-2875-4_2.
15. A. Mishra et al., "Effect of annealing temperature on the performance of printable carbon electrodes for perovskite solar cells," *Org. Electron.*, vol. 65, pp. 375–380, 2019, <https://doi.org/10.1016/j.orgel.2018.11.046>.
16. F. Cataldo, "A study on the thermal stability to 1000 °C of various carbon allotropes and carbonaceous matter both under nitrogen and in air," *Fullerenes, Nanotub. Carbon Nanostructures*, vol. 10, no. 4, pp. 293–311, 2002, <https://doi.org/10.1081/FST-120016451>.
17. M. Schubert et al., "Powder aerosol deposition method — novel applications in the field of sensing and energy technology," *Funct. Mater. Lett.*, vol. 12, no. 05, p. 1930005, 2019, <https://doi.org/10.1142/s1793604719300056>.
18. D. Hanft, J. Exner, M. Schubert, T. Stöcker, P. Fuierer, and R. Moos, "An overview of the Aerosol Deposition method: Process fundamentals and new trends in materials applications," *J. Ceram. Sci. Technol.*, vol. 6, no. 3, pp. 147–181, 2015, <https://doi.org/10.4416/JCST2015-00018>.
19. J. Akedo, "Room Temperature Impact Consolidation (RTIC) of Fine Ceramic Powder by Aerosol Deposition Method and Applications to Microdevices," *J. Therm. Spray Technol.*, vol. 17, no. 2, pp. 181–198, 2008, <https://doi.org/10.1007/s11666-008-9163-7>.
20. M. Linz et al., "Revealing the Deposition Mechanism of the Powder Aerosol Deposition Method Using Ceramic Oxide Core–Shell Particles," *Adv. Mater.*, p. 2308294, 2023, <https://doi.org/10.1002/adma.202308294>.
21. R. Saunders, S. D. Johnson, D. Schwer, E. A. Patterson, H. Ryou, and E. P. Gorzkowski, "A Self-Consistent Scheme for Understanding Particle Impact and Adhesion in the Aerosol Deposition Process," *J. Therm. Spray Technol.*, vol. 30, no. 3, pp. 523–541, 2021, <https://doi.org/10.1007/s11666-021-01164-4>.
22. N. H. Khansur, U. Eckstein, L. Benker, U. Deisinger, B. Merle, and K. G. Webber, "Room temperature deposition of functional ceramic films on low-cost metal substrate," *Ceram. Int.*, vol. 44, no. 14, pp. 16295–16301, 2018, <https://doi.org/10.1016/j.ceramint.2018.06.027>.
23. M. Šadl et al., "Energy-storage-efficient 0.9Pb(Mg_{1/3}Nb_{2/3})O₃–0.1PbTiO₃ thick films integrated directly onto stainless steel," *Acta Mater.*, vol. 221, p. 117403, 2021, <https://doi.org/10.1016/j.actamat.2021.117403>.
24. M. Šadl, A. Lebar, J. Valentincic, and H. Ursic, "Flexible Energy-Storage Ceramic Thick-Film Structures with High Flexural Fatigue Endurance," *ACS Appl. Energy Mater.*, vol. 5, no. 6, pp. 6896–6902, 2022, <https://doi.org/10.1021/acsaem.2c00518>.
25. M. Šadl et al., "Multifunctional flexible ferroelectric thick-film structures with energy storage, piezoelectric and electrocaloric performance," *J. Mater. Chem. C*, vol. 11, no. 29, pp. 10058–10068, 2023, <https://doi.org/10.1039/D3TC01555F>.
26. D. W. Lee, O. Y. Kwon, W. J. Cho, J. K. Song, and Y. N. Kim, "Characteristics and Mechanism of Cu Films Fabricated at Room Temperature by Aerosol Deposition," *Nanoscale Res. Lett.*, vol. 11, no. 1, 2016, <https://doi.org/10.1186/s11671-016-1378-9>.
27. N. H. Khansur et al., "Enhanced Electromechanical Response and Thermal Stability of 0.93(Na_{1/2}Bi_{1/2})TiO₃–0.07BaTiO₃ Through Aerosol Deposition of Base Metal Electrodes," *Adv. Mater. Interfaces*, vol. 93, p. 2100309, 2021, <https://doi.org/10.1002/admi.202100309>.
28. Y.-H. Kim, J.-W. Lee, H.-J. Kim, Y.-H. Yun, and S.-M. Nam, "Silver metallization for microwave device using aerosol deposition," *Ceram. Int.*, vol. 38, pp. S201–S204, 2012, <https://doi.org/10.1016/J.CERAMINT.2011.04.083>.
29. M.-Y. Cho et al., "Formation of silver films for advanced electrical properties by using aerosol deposition process," *Jpn. J. Appl. Phys.*, vol. 57, no. 11S, p. 11UF05, 2018, <https://doi.org/10.7567/JJAP.57.11UF05>.
30. M. Šadl, U. Tomc, and H. Ursic, "Investigating the Feasibility of Preparing Metal–Ceramic Multi-Layered Composites Using Only the Aerosol-Deposition Technique," *Materials*, vol. 14, no. 16, p. 4548, 2021, <https://doi.org/10.3390/ma14164548>.
31. V. Regis, M. Šadl, G. Brennecka, A. Bradeško, U. Tomc, and H. Uršič, "Investigation of Structural and Electrical Properties of Al₂O₃/Al Composites

- Prepared by Aerosol Co-Deposition," *Crystals*, vol. 13, no. 5, p. 850, 2023, <https://doi.org/10.3390/cryst13050850>.
32. N. Leupold, S. Denneler, G. Rieger, and R. Moos, "Powder Treatment for Increased Thickness of Iron Coatings Produced by the Powder Aerosol Deposition Method and Formation of Iron–Alumina Multilayer Structures," *J. Therm. Spray Technol.*, vol. 30, no. 3, pp. 480–487, 2020, <https://doi.org/10.1007/s11666-020-01098-3>.
33. J. Kwon, H. Park, I. Lee, and C. Lee, "Effect of gas flow rate on deposition behavior of Fe-based amorphous alloys in vacuum kinetic spray process," *Surf. Coatings Technol.*, vol. 259, pp. 585–593, 2014, <https://doi.org/10.1016/j.surfcoat.2014.10.026>.
34. S. Baba, L. Huang, H. Sato, R. Funahashi, and J. Akedo, "Room-temperature fast deposition and characterization of nanocrystalline $\text{Bi}_{0.4}\text{Sb}_{1.6}\text{Te}_3$ thick films by aerosol deposition," *J. Phys. Conf. Ser.*, vol. 379, no. 1, p. 012011, 2012, <https://doi.org/10.1088/1742-6596/379/1/012011>.
35. S. Baba, H. Sato, L. Huang, A. Uritani, R. Funahashi, and J. Akedo, "Formation and characterization of polyethylene terephthalate-based $(\text{Bi}_{0.15}\text{Sb}_{0.85})_2\text{Te}_3$ thermoelectric modules with CoSb_3 adhesion layer by aerosol deposition," *J. Alloys Compd.*, vol. 589, pp. 56–60, 2014, <https://doi.org/10.1016/j.jallcom.2013.11.180>.
36. S. Sugimoto, T. Maeda, R. Kobayashi, J. Akedo, M. Lebedev, and K. Inomata, "Magnetic properties of Sm-Fe-N thick film magnets prepared by the aerosol deposition method," *IEEE Trans. Magn.*, vol. 39, no. 5, pp. 2986–2988, 2003, <https://doi.org/10.1109/TMAG.2003.816715>.
37. S. Sugimoto et al., " $\text{Nd}_2\text{Fe}_{14}\text{B}/\text{Fe}_3\text{B}$ nanocomposite film fabricated by aerosol deposition method," *J. Alloys Compd.*, vol. 408–412, pp. 1413–1416, 2006, <https://doi.org/10.1016/j.jallcom.2005.04.044>.
38. C.-W. Ahn et al., "Microstructure and electrochemical properties of graphite and C-coated LiFePO_4 films fabricated by aerosol deposition method for Li ion battery," *Carbon N. Y.*, vol. 82, pp. 135–142, 2015, <https://doi.org/10.1016/j.carbon.2014.10.043>.
39. S. Michalkiewicz, A. Skorupa, and M. Jakubczyk, "Carbon materials in electroanalysis of preservatives: A review," *Materials*, vol. 14, no. 24, 2021, <https://doi.org/10.3390/ma14247630>.
40. T. Gan and S. Hu, "Electrochemical sensors based on graphene materials," *Microchim. Acta*, vol. 175, no. 1–2, pp. 1–19, 2011, <https://doi.org/10.1007/s00604-011-0639-7>.
41. A. C. Power, B. Gorey, S. Chandra, and J. Chapman, "Carbon nanomaterials and their application to electrochemical sensors: a review," *Nanotechnol. Rev.*, vol. 7, no. 1, pp. 19–41, 2018, <https://doi.org/10.1515/ntrev-2017-0160>.
42. E. Asadian, M. Ghalkhani, and S. Shahrokhian, "Electrochemical sensing based on carbon nanoparticles: A review," *Sensors Actuators B Chem.*, vol. 293, pp. 183–209, 2019, <https://doi.org/10.1016/j.snb.2019.04.075>.
43. Annu, S. Sharma, R. Jain, and A. N. Raja, "Review—Pencil Graphite Electrode: An Emerging Sensing Material," *J. Electrochem. Soc.*, vol. 167, no. 3, p. 037501, 2020, <https://doi.org/10.1149/2.0012003JES>.
44. M. Šadl, U. Tomc, U. Prah, and H. Ursic, "Protective Alumina Coatings Prepared by Aerosol Deposition on Magnetocaloric Gadolinium Elements," *Inf. MIDEM - J. Microelectron. Electron. Components Mater.*, vol. 49, no. 3, pp. 177–182, 2019, <https://doi.org/10.33180/InfMIDEM2019.306>.
45. I. Stojanoska et al., "Indium-zinc-oxide thin films produced by low-cost chemical solution deposition: Tuning the microstructure, optical and electrical properties with the processing conditions," *Heliyon*, vol. 9, no. 9, p. e19744, 2023, <https://doi.org/10.1016/j.heliyon.2023.e19744>.
46. I. Lavagnini, R. Antiochia, and F. Magno, "An Extended Method for the Practical Evaluation of the Standard Rate Constant from Cyclic Voltammetric Data," *Electroanalysis*, vol. 16, no. 6, pp. 505–506, 2004, <https://doi.org/10.1002/elan.200302851>.
47. D.-W. Lee et al., "Experimental and numerical study for Cu metal coatings at room temperature via powder spray process," *Surf. Coatings Technol.*, vol. 353, pp. 66–74, 2018, <https://doi.org/10.1016/j.surfcoat.2018.08.075>.
48. S. S. Manokhin, V. Y. Barinov, and O. A. Golosova, "Aerosol Deposition of MAX Phase-Based Coatings onto High-Temperature Nickel Alloy," *Int. J. Self-Propagating High-Temperature Synth.*, vol. 28, no. 3, pp. 210–212, 2019, <https://doi.org/10.3103/S1061386219030087>.
49. S. Choi, J.-H. Lim, E.-Y. Kang, H. Kim, Y.-M. Kong, and D.-Y. Jeong, "Deposition behavior of glass thick film formation on substrates with different hardness by aerosol deposition," *J. Asian Ceram. Soc.*, vol. 9, no. 3, pp. 1128–1136, 2021, <https://doi.org/10.1080/21870764.2021.1943155>.
50. M. Hatala, P. Gemeiner, M. Hvojník, and M. Mikula, "The effect of the ink composition on the performance of carbon-based conductive screen printing inks," *J. Mater. Sci. Mater. Electron.*, vol. 30, no. 2, pp. 1034–1044, 2019, <https://doi.org/10.1007/s10854-018-0372-7>.
51. "Int. Centre Diffraction Data (ICDD) PDF-4+ / Web 2023." 2023, <https://www.icdd.com/assets/files/2023-PDF-4-Web-Flyer.pdf>.

52. J. Exner, M. Schubert, D. Hanft, J. Kita, and R. Moos, "How to treat powders for the room temperature aerosol deposition method to avoid porous, low strength ceramic films," *J. Eur. Ceram. Soc.*, vol. 39, no. 2–3, pp. 592–600, 2019, <https://doi.org/10.1016/j.jeurceramsoc.2018.08.008>.
53. M. Dekleva et al., "An innovative pretreatment protocol to eliminate silver contamination-induced voltammetric interference on graphite-glass working electrode," *Electrochem. commun.*, vol. 162, p. 107707, 2024, <https://doi.org/10.1016/j.elecom.2024.107707>.
54. M. G. Trachioti, A. C. Lazanas, and M. I. Prodromidis, "Shedding light on the calculation of electrode electroactive area and heterogeneous electron transfer rate constants at graphite screen-printed electrodes," *Microchim. Acta*, vol. 190, no. 7, p. 251, 2023, <https://doi.org/10.1007/s00604-023-05832-w>.
55. A. Pop, I. Birsan, C. Orha, R. Pode, and F. Manea, "Carbon-Based Electrode for Parabens Detection," vol. 10, no. 9, pp. 1228–1236, 2016, <https://doi.org/10.5281/zenodo.1127017>.
56. P. K. Jiwanti, B. Y. Wardhana, L. G. Sutanto, and M. F. Chanif, "A Review on Carbon-based Electrodes for Electrochemical Sensor of Quinolone Antibiotics," *ChemistrySelect*, vol. 7, no. 15, 2022, <https://doi.org/10.1002/slct.202103997>.
57. W. Duan, M. R. Baez-Gaxiola, M. Gich, and C. Fernández-Sánchez, "Detection of chlorinated organic pollutants with an integrated screen-printed electrochemical sensor based on a carbon nanocomposite derived from bread waste," *Electrochim. Acta*, vol. 436, p. 141459, 2022, <https://doi.org/10.1016/j.electacta.2022.141459>.
58. A. M. Abdel-Aziz, H. H. Hassan, and I. H. A. Badr, "Activated Glassy Carbon Electrode as an Electrochemical Sensing Platform for the Determination of 4-Nitrophenol and Dopamine in Real Samples," *ACS Omega*, vol. 7, no. 38, pp. 34127–34135, 2022, <https://doi.org/10.1021/acsomega.2c03427>.



Copyright © 2024 by the Authors.
This is an open access article distributed under the Creative Commons

Attribution (CC BY) License (<https://creativecommons.org/licenses/by/4.0/>), which permits unrestricted use, distribution, and reproduction in any medium, provided the original work is properly cited.

Arrived: 19. 04. 2024

Accepted: 18. 06. 2024

Low Power CMOS Full Adder Cells based on Alternative Logic for High-Speed Arithmetic Applications

Sriram Sundar Subramanian¹, Mahendran Gandhi²

¹*Department of Electronics & Communication Engineering, CARE College of Engineering, Tiruchirappalli, Tamilnadu, India*

²*Department of Electronics & Communication Engineering, Syed Ammal Engineering College, Ramanathapuram, Tamilnadu, India*

Abstract: As the demand for computational capabilities continues to grow, the design and optimization of arithmetic circuits have more crucial in modern digital systems. The efficient operations of these arithmetic circuits heavily depend on the performance of fundamental modules such as Full Adders (FA). In addition to addressing typical challenges, designing full adder circuits using alternative logic offers unique advantages that are vital for the developing landscape of digital system. This paper presents two FAs based on alternative structures using modified Double Pass-Transistor Logic (DPL) for fast computing. The proposed Multiplexer based alternative structure differs from other conventional structures by concurrently generating both the carry signal and the sum signal, significantly reducing the overall propagation time. In addition to that multiplexers are controlled by external signals, the proposed structures provide full swing outputs. Also the modified DPL improves the signal integrity and noise immunity. The proposed circuits' performances were compared with other conventional logic and few hybrid adders. In comparison with other logics, various type of simulation results indicate that the proposed FA-2 exhibits improved performance in terms of average power, average delay, and average power-delay product (PDP). Our proposed FA-2 shows performance improvement over conventional CMOS for Power, Delay, and PDP, with values of 3.304%, 69.017%, and 74.602%, respectively. Full adders were simulated under different supply voltages and process corners to measure the reliability and robustness. Noise tolerances of full adder circuits were calculated using Average Noise Threshold Energy (ANTE) methodology.

Keywords: Full Adder, Alternative Logic, Multiplexer, Double Pass Transistor, Low Power

Celice CMOS z nizko porabo energije na osnovi alternativne logike za hitre aritmetične aplikacije

Izveček: Ker povpraševanje po računskih zmogljivostih še naprej narašča, sta načrtovanje in optimizacija aritmetičnih vezij v sodobnih digitalnih sistemih vedno bolj pomembna. Učinkovito delovanje teh aritmetičnih vezij je močno odvisno od delovanja temeljnih modulov, kot so popolni seštevalniki (FA). Oblikovanje vezij polnih seštevalnikov z uporabo alternativne logike poleg reševanja tipičnih izzivov ponuja tudi edinstvene prednosti, ki so ključne za razvijajočo se okolje digitalnih sistemov. V tem članku sta predstavljena dva FA, ki temeljita na alternativnih strukturah z uporabo modificirane logike dvojnega prehoda in tranzistorja (DPL) za hitro računanje. Predlagana alternativna struktura, ki temelji na multipleksorju, se od drugih običajnih struktur razlikuje po tem, da hkrati generira tako prenosni signal kot celotni signal, kar znatno skrajša skupni čas širjenja. Poleg tega multiplekserje nadzorujejo zunanji signali, predlagane strukture pa zagotavljajo polne nihajne izhode. Prav tako spremenjeni DPL izboljša celovitost signala in odpornost proti šumu. Delovanje predlaganih vezij smo primerjali z drugimi konvencionalnimi logičnimi in hibridnimi seštevalniki. V primerjavi z drugimi logikami rezultati kažejo, da predlagani FA-2 izkazuje izboljšano zmogljivost v smislu povprečne moči, povprečne zakasnitve in povprečnega produkta moči in zakasnitve (PDP). Naš predlagani FA-2 kaže izboljšanje zmogljivosti v primerjavi s konvencionalnim CMOS za moč, zakasnitev in PDP z vrednostmi 3,304 %, 69,017 % in 74,602 %. Popolni seštevalniki so bili simulirani pod različnimi napajalnimi napetostmi in procesnimi koti, da bi izmerili zanesljivost in robustnost. Šumne tolerance polnih seštevalnikov so bile izračunane z uporabo metodologije ANTE (Average Noise Threshold Energy).

Ključne besede: popolni seštevalnik; alternativna logika; multiplekser; dvojni prehodni tranzistor; nizka poraba energije

*Corresponding Author's e-mail: s.sriramsundar@gmail.com, vishnumahendran2010@gmail.com

How to cite:

S. S. Subramanian et al., "Low Power CMOS Full Adder Cells based on Alternative Logic for High-Speed Arithmetic Applications", Inf. Midem-J. Microelectron. Electron. Compon. Mater., Vol. 54, No. 3(2024), pp. 187–200

1 Introduction

The widespread usage of portable battery-operated electronic devices has made the adoption of VLSI circuits more important [1]. Present electronic hardware is designed for high performance operation. Energy efficiency and operating speed are considered as the important parameters for portability of any system. The increasing semiconductor market for portable devices demands for low-power building components to enable long-lasting battery-powered systems. Furthermore, the trend towards increasing circuit complexity and operating frequencies in high-performance applications necessitates the designing of high-speed circuit components [2]. Power dissipation in conventional CMOS (C-MOS) circuits is classified as Dynamic power dissipation ($P_{dynamic}$) and Static power dissipation (P_{static}). The main sources of power consumption are due to short circuit path, increased switching and various leakage currents. Short circuit power ($P_{short-dynamic}$) due to both p-channel and n-channel MOS transistors are active at the same time during transitions, Switching power $P_{switch-dynamic}$ is associated with charging/discharging at node/load capacitance and leakage power due reverse leakage current and sub-threshold currents. The total power dissipation (P_{Tot}) [3] can be expressed using equations 1 and 2.

$$P_{Tot} = P_{short-dynamic} + P_{switch-dynamic} + P_{static} \quad (1)$$

$$P_{Tot} = I_{sc} V_{dd} + \alpha C_L V_{dd} V_s f_{clk} + I_{static} V_{dd} \quad (2)$$

Among these, $P_{switch-dynamic}$ is treated as the major component for P_{Tot} . In above equation 2, I_{sc} indicates the short circuit current, C_L is the node/load parasitic capacitance, α denotes average number of switchings that have occurred in particular time period, V_s is the voltage swing (typically equivalent to V_{dd}), f_{clk} denotes clock frequency and I_{static} is the static current. PDP metric is always used to measure the energy expended in performing a specific action and serves as a vital performance parameter while evaluating optimization for a circuit component designed, implemented and tested under varying technologies, wide range of operating frequencies, and setups. Full adder cells are essential components in digital system design to perform binary addition, which is fundamental for performing arithmetic operations and data processing in digital circuits. Application Specific Integrated Circuits (ASIC), Microprocessors and DSP processors depends on efficient arithmetic cells for specific computations like convolution and advanced filtering [4]. Full Adder (FA) is widely used as one the main module to construct such arithmetic cells. Full Adder cell play a significant role in controlling the critical path of complicated arithmetic operations including, division, multiplication ex-

ponentiation, and more [5]. Moreover, in various data processing applications such as digital signal processing, cryptography, and data compression, full adder cells facilitate the computation and manipulation of binary data efficiently.

Despite their importance, full adder cells have several challenges in their design and implementation. Some of these challenges are achieving fast computation, minimizing power consumption, robustness for process variations, better noise tolerance, and optimizing area utilization in integrated circuits. So meeting these requirements are important for realizing the full adder cells to construct high-performance digital systems.

The integrated circuits (ICs) performance is limited by the effectiveness of arithmetic processes within the cell. The choice of circuits for implementing adder cells depends on various performance metrics. Different ways of designing logic tend to focus on one aspect of performance but may neglect the other. The PDP of the FA cell impacts the complete system performance. Considering this, designing an energy efficient FA cell with minimal propagation delay has become crucial for modern digital systems [2].

Improving performance according to Moore's law requires more than just advancing fabrication technology; it also involves focusing on other factors, particularly implementing a suitable circuit design [6]. Various logic styles and techniques have been developed for arithmetic cells, which reduce the total cost and improving the whole performance of ICs. Minimizing the V_{dd} is a prominent approach for decreasing power consumption; however it results in slower circuit's speed and reduces the driving capacity of circuits. Many static logic styles such as pass transistor logic (PTL) and C-CMOS logic structures are play a vital role in constructing the low power FA cells. The C-CMOS FA cell structures are more robust, and it facilitates transistor sizing which allows scaling of different voltages to guarantee the proper functionality [7].

Many investigations have been published on optimizing low-power and high speed full-adders. These papers explore various conventional logic styles, such as C-CMOS [8], CMOS Transmission Gate (CMOS TG) [9], Pseudo nMOS [10], PTL [11], Cascode Voltage Switch Logic (CVSL) [12], Complementary PTL (CPL) [13], Differential Cascode Voltage Switch Logic (DCVL)[14], DCVL with the pass-gate tree (DCVSPG)[13], Double Pass transistor logic style (DPL) [15], Swing-Restored PTL (SRPL) [16], Swing-Restored CPL (SR-CPL)[17], Energy Economized PTL (EEPL) [18], and as well as different logic structures for building the adder module.

In recent days, researchers focus on the hybrid design approach that incorporates features from multiple logic styles. Yingtao et al. [19] introduced a 12-transistor low power hybrid FA cell using MUX logic and it is capable of reduced switching activity, charge recycling capability along with reduced short circuit power consumption. Pankaj et al. [20] proposed a novel FA cell by modifying the internal logic structure and this circuit is significantly reducing the PDP.

Naseri et al [21] introduced 6 low power hybrid FA cells by altering the EXOR/EXNOR logic gate structure for high-speed applications. The novel structures overcome the drawbacks of conventional logic by removing the inverter logic in the critical path. Also it replacing the positive feedback at the output terminal. Mehedi et al. [22] proposed a hybrid Full Adder for full voltage swing using a scalable XOR-XNOR block designed for large word-length architectures. They highlighted that many FA cells performing well as 1-bit adder but extending them for wide word length is more difficult. Jyoti et al. [23] recommended a high-speed 20-transistor hybrid FA (HFA) structure using three distinct elements for arithmetic applications.

Sharmila et al. [24] proposed a novel FA cell based on reversible logic. They conveyed that proposed FA cell more useful in designing the current-mode logic circuits. Authors highlighted that information retention and inverse computation are feasible in reversible logic. So that in recent years' researchers prefers reversible logic for low-power VLSI circuit design. Azeem et. al [25] introduced a high performance 14-T HFA using PTL and GDI logic for arithmetic applications. They pointed out that hybrid styles are most preferable for implementing FA cell in recent years. Rahimi et. al [26] introduced a high performance 9-Transistors Full Adder cell based on pseudo dynamic logic for low power arithmetic applications. Since the circuit has reduced number of internal nodes which are connected with ground, it is more energy efficient than C-CMOS, CMOS TG, PTL and DPL.

The objective of this research is to combine the benefits of multiple logic designs to construct the hybrid FA cell. The proposed hybrid methods can leverage the strengths of each logic design technique while mitigating their respective limitations. This integration can improve the FA cell's performance in terms of speed, power efficiency, and noise tolerance compare to other conventional structures.

2 Full adder using alternative logic

The alternative style full adder cell gives a different approach compared to the conventional full adder cir-

cuits. This alternative logic structure employs a unique internal logic using the multiplexers. The Boolean functions $A+B$, $A.B$, $A\oplus B$ and $\overline{A\oplus B}$ are selected from the two distinct multiplexers to produce the output signals. Such designs are aims to achieve the delay balance between the Sum and Carry signals. Furthermore, PTL are the powerless/groundless logic structures and they are used to build power efficient full adder cell using alternative logic. The focus on optimizing power consumption and reducing propagation delays discriminates this alternative full adder logic cell. This differentiation makes it a potential improvement over other conventional designs for building low-power arithmetic circuits

Aguirre [27] proposed an Alternate Full Adder cell using Multiplexer for High Speed Application is illustrated in Figure 1. This structure comprises of three distinct modules. The Block 1 generates the logic output of $A+B$, $A.B$, $A\oplus B$ and $\overline{A\oplus B}$ simultaneously. So it apparently lessens the propagation delay of Carry signal present in the conventional full adder logic. Block 2 and Block 3 are the two independent 2X1 multiplexers evaluate the Sum(S_0) and Carry(C_0) from the outputs obtained from Block 1. Unlike Conventional Full Adder circuit, the alternative full adder cell evaluates the Sum(S_0) and Carry(C_0) outputs with relatively equal propagation delay.

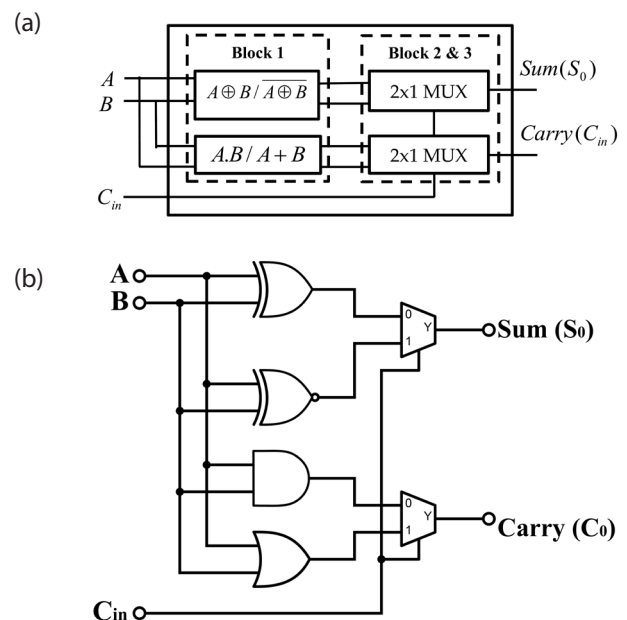


Figure 1: (a&b) : Full Adder Structure using Multiplexer based Alternative Logic

Referring to the FA functionality from the Table 1, we can observe that Sum (S_0) signal is chosen from logic values $A\oplus B$ and $\overline{A\oplus B}$ with the help of third input C_i . When $C_i=0$, multiplexer-1 will chose $A\oplus B$ logic value

and $C_i=1$, multiplexer-1 will chose $\overline{A \oplus B}$ logic value for Sum (S_o).

Table 1: 1-bit Full adder circuit logic table

Inputs			Block 1 Outputs				Outputs	
A	B	C_i	A XOR B	A XNOR B	A.B	A+B	Block 2 Sum (S_o)	Block 3 Carry (C_o)
0	0	0	0	1	0	0	0	0
0	0	1	0	1	0	0	1	0
0	1	0	1	0	0	1	1	0
0	1	1	1	0	0	1	0	1
1	0	0	1	0	0	1	1	0
1	0	1	1	0	0	1	0	1
1	1	0	0	1	1	1	0	1
1	1	1	0	1	1	1	1	1

Similarly, the multiplexer-2 chose one of the output from A.B or A+B logic for the Carry(C_o) based on the third input C_i . In both Sum (S_o) and Carry(C_o) generation cases, third input C_i will be act as control signal for the multiplexers 1 & 2. Selecting the sum and carry from Multiplexer simultaneously will significantly reduce the overall propagation delay. So alternative full adder structures are widely used to construct the high speed datapath circuits. The alternative logic configuration has the following features.

- The signals internally generated are not utilized to control the output of the multiplexer. Alternatively, the third input signal ' C_i ' controls the mux output and produces maximum voltage swing without any additional delay. This apparently lessens the total propagation delay of the FA circuit.
- In submicron fabrication technologies, diffusion capacitances of source/drain terminals act as an important role. In alternative logic, C_i is connected only with few transistors Gate terminal and it is not connected with any of the source/drain of the transistors. This configuration significantly reduces the load capacitance of the C_i input. Therefore critical path propagation time for C_i is minimized. So large module's overall propagation delay can be reduced.
- The outputs signal's (S_o and C_o) propagation delay could be varied by adjusting size of the logic gates (XOR/XNOR and AND/OR) separately present in the Block 1. This characteristic is beneficial in scenarios where the skew between incoming signals is critical, such as in wave pipelining. Additionally, it helps to maintain propagation delay balancing at the output port. It reduces the risk of glitches in cascaded structures.

3 Hybrid full adders using modified DPL

As the technology moving into sub-micron level, many novel circuit styles and structures were introduced recently to overcome the limitations of the C-CMOS logics. PTL is a fundamental digital circuit style, depends on MOS transistors as pass gates to implement logical functions. PTL circuits are designed by either NMOS or PMOS transistor. This difference from the C-CMOS design, which uses both NMOS and PMOS transistors, makes PTL simpler and potentially better. But the choice is typically based on the technology process and optimization goals. Usually the PTL circuits are constructed by connecting the pass gates to obtain complex logic functions. Multiplexers, demultiplexers, flip-flops, and other digital circuit's modules can be implemented using pass transistor configurations. PTL has gained attraction due to its low power consumption, and ability to operate at high speeds.

Even though PTL circuits are simpler than other conventional styles, it is also have some challenges in implementation. Signal degradation due to the resistance introduced by the pass switches is recognized as one of the main issue faced by PTL. As signals pass through multiple stages of pass gates, the total resistance can lead to a significant reduction in signal levels. Threshold drop is another concern present in the PTL circuits. The voltage drop caused the each pass transistor can influence change in the logical threshold levels. While the voltage drop isn't a big problem in nMOS logic, it can cause issues in CMOS by making both p and n transistors conduct simultaneously. This incident seriously affects the circuit's noise margin and overall reliability. Always pairing the nMOS transistor with a pMOS is a complex solution to achieve the necessary full swing in output voltage. Figure 2 depicts the EX-OR gate

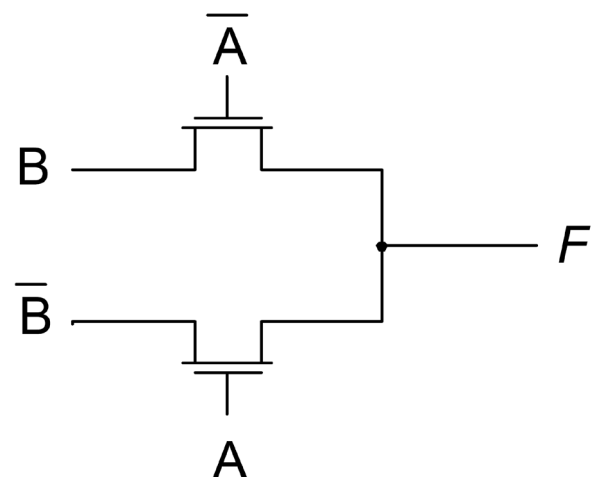


Figure 2: EX-OR Logic Gate implementation using PTL

($F = A'.B + A.B' = A \oplus B$) implementation through NMOS pass transistor logic. Figure 3 depicts the Threshold drop at the output terminal of the PTL gate.

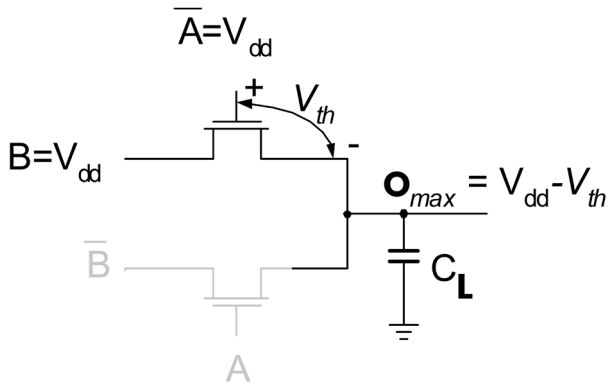


Figure 3: Threshold drop at output of the pass-transistor gate

The introduction of new CMOS logic families, such as CPL and DPL using pass-transistor circuits, aimed to improve both speed and power efficiency. Employing CPL in Digital circuit design not only resulted in an efficient implementation but also fast logic operation due to higher logic functionality and lower input capacitance. However, lower supply voltage CPL implementation, it is essential to consider the challenges posed by speed degradation and noise margin. These issues are arising due to discrepancy between logic threshold voltage and fluctuation of input signal levels caused by process variations. Also, CPL facing the threshold voltage drop problem while the signal passing via series of pass-transistors and its voltage was lessened by one V_T (threshold voltage drop). In the modern CPL versions, the “threshold drop” issue is addressed by using a special inverter that could restore the signal amplitude to its maximum potential. Since the signal restoration in CPL is not depending on the load present at the output port, signal restoration is done quickly during the signal transition with less amount of power.

DPL is another modified CPL style designed to fulfill the drawbacks of CPL in reduced supply voltage configurations. DPL was initially developed to address the ‘threshold drop’ issues in CPL and provide an alternative style to PTL. It is implemented with dual-stage architecture, using both NMOS and PMOS transistors in parallel for each pass gate, effectively eliminating the ‘threshold drop.’ Therefore, there is no need for level-restoring inverters after each logic block, improves speed of DPL. As mentioned previously, DPL gates improve the overall circuit performance at lower supply voltages by employing the both nMOS and PMOS transistors. Due to the symmetrical structure of DPL, load at the input side is equally distributed between all the

inputs. The XOR/XNOR gates designed by DPL exhibits perfect symmetry. With the help of dual transmission property and symmetrical arrangement, the DPL works effectively in wave pipelined circuits [28]. In DPL, dual current path is created due to the structure of the parallelly connected NMOS transistors and PMOS transistors for each input signal’s combinations and produces very small equivalent resistance compared with other conventional logic structures.

As reported by Uming Ko et al. [29], DPL was the highly energy-efficient logic methodology compared to other discussed logics. DPL can more effectively tackle challenges such as signal degradation and threshold drop, resulting in improved signal integrity and driving capability. DPL is well-suited for applications requiring improved signal integrity, minimal signal degradation, and better driving capability. Its dual-stage architecture makes it advantageous for high-speed digital circuits, memory cells, arithmetic units, and other scenarios where noise margins are more critical. Though DPL has many advantages, it is facing certain drawbacks such as Complexity and Area Overhead due to dual-stage architecture. Figure 4 depicts the AND and NAND Logic Gates using DPL. In this paper, we proposed two FA cells built using alternative structure by DPL to enhance noise margins, increase the operating speed and decrease power dissipation.

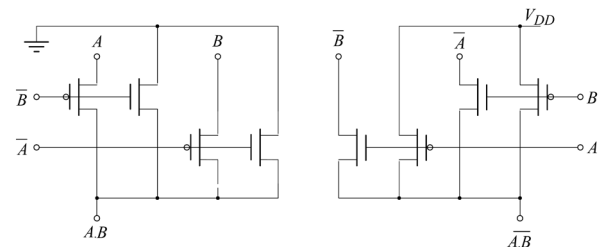


Figure 4: AND and NAND Logic Gates using DPL

Figure 5 shows the Proposed Full Adder 1 based on alternative logic using DPL. The Full Adder circuit is realized through the Alternative logic structure using DPL. In this structure, $A \oplus B$ and $\overline{A \oplus B}$ were obtained through two DPL circuits. For example, $F = A'.B + A.B' = A \oplus B$ and $A'.B / A.B'$ is obtained through both NMOS and PMOS which ensures Good Logic 1/0 is delivered through the pass switch. Similarly, all the sum of product terms for $A \oplus B$ and $\overline{A \oplus B}$ were obtained in the first stage through both NMOS and PMOS transistor to get the better voltage swing. Since $A \oplus B$ and $\overline{A \oplus B}$ were generated in parallel, there is negligible delay difference between them. Unlike CPL, $A \oplus B$ and $\overline{A \oplus B}$ operate at full swing levels, and there is no need for swing restoration logic at the $A \oplus B$ and $\overline{A \oplus B}$ nodes.

The subsequent stage is the two parallel 2x1 multiplexers obtained through alternative logic. Sum and Carry of the FA circuit is generated by those multiplexers with almost equal propagation delay.

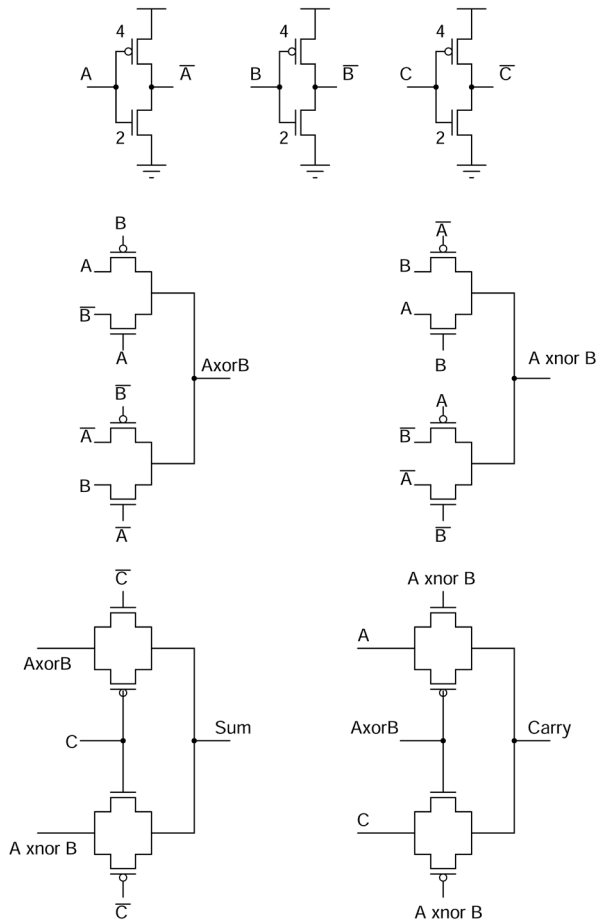


Figure 5: Proposed alternative logic based Full Adder 1 using DPL

In the Sum structure the multiplexer is controlled by the third input C which is not an internally generated signal. So that it can produce full voltage swing output at the Sum terminal with less propagation delay. At the same time, the Carry signal is produced by second multiplexer where either $A \oplus B$ and $\overline{A \oplus B}$ will act as control signal to select the input. Since $A \oplus B$ and $\overline{A \oplus B}$ are internally generated by the circuits, the Carry signal has slightly smaller voltage swing than Sum signal with small amount of additional delay. The second proposed circuit will overcome this issue by not using the internally generated signals for controlling the multiplexers.

Figure 6 shows the Proposed Hybrid Full Adder 2 based on alternative logic using DPL based on alternative logic using DPL. In the first stage, logical values $A \oplus B$ and $\overline{A \oplus B}$ are obtained using DPL and like similar way and

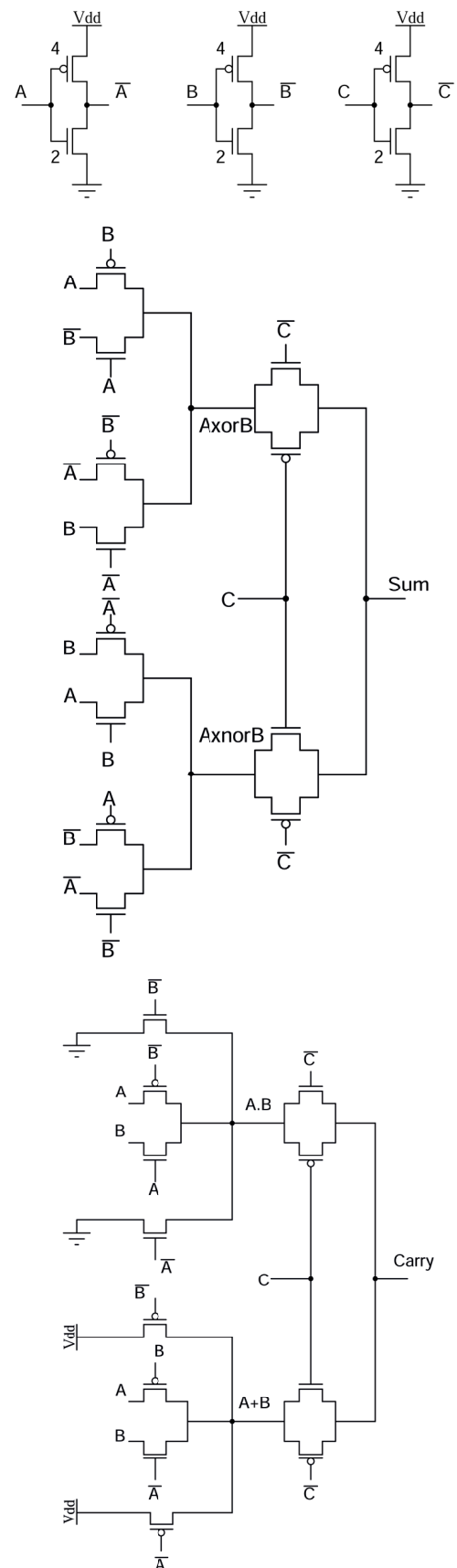


Figure 6: Proposed Hybrid Full Adder 2 based on alternative logic using DPL

obtained through modified DPL. Similar to proposed FA 1, the second proposed adder also generates all the sum of product terms in parallel with full voltage swing.

Since $A \oplus B$, $\overline{A \oplus B}$, $A + B$ and $A.B$ outputs obtained in parallel manner, there is no significant propagation delay difference among them. Also, they are generated through DPL, signal restoration is not required. In the $A.B$ and $A + B$ network, we have included two additional NMOS/PMOS transistors in which connections of their source terminals with either ground/ V_{dd} supply to enable quick discharging/charging of the node. The second stage is the two parallel multiplexers similar to proposed FA 1. But here the Sum and Carry multiplexers are controlled by third input signal rather than internally generated signal. So the Sum and Carry output will be at full voltage swing without any additional delay.

4 Simulation environment, results and discussions

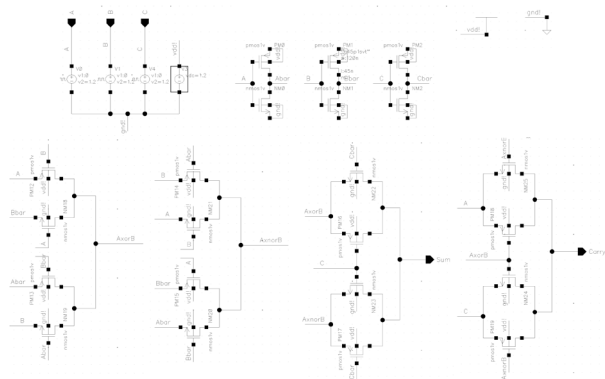


Figure 7: Proposed FA Cell 1 schematic design

Figure 7 and Figure 8 show the proposed full adders schematics designed in cadence virtuoso schematic editor. Figure 9 and Figure 10 depict the transient analysis waveforms of the proposed Full Adders obtained by using Analog Design Environment L tool. Figure 11 and Figure 12 show the layouts obtained through Cadence Layout XL tool for the proposed Full Adder Cells. Table 2 illustrates the comparison results of Min and Max delay, Average delay, Power, PDP, transistor count and area requirement for each FA cell using several conventional and novel full adder styles discussed in our literature namely C-CMOS [8], CMOS TG [9], Pseudo nMOS [10], PTL [11], CVSL [12], CPL [13], DCVL [14], DCVSPG [13], DPL [15], SRPL [16], SR-CPL [17], EEPL [18], Naseri (HFA-22T) [21], Mehedi [22], Jyoti [23], Sharmila [24], Azeem [25], Rahimi [26], Proposed Logic 1 and Proposed Logic 2. Since proposed full adders are designed using DPL

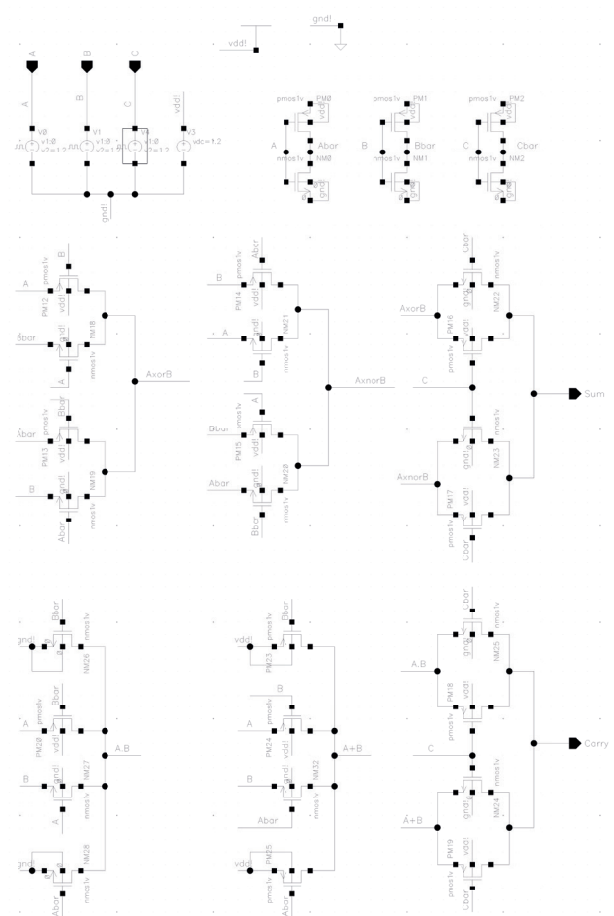


Figure 8: Proposed Full Adder 2 schematic design

and they ensure the full voltage swing output in all the conditions. In the proposed full adder 1 carry signal is produced by internally generated signals, the voltage swing for carry is little lower than the carry signal produced by proposed full adder 2. Additional inclusion of transistors in the $A \oplus B$, $\overline{A \oplus B}$, $A + B$ and $A.B$ logic modules significantly reduces the switching time by quickly charge/discharge the internal nodes. The fast switchings make the proposed circuits better suited for constructing arithmetic circuits and DSP processors etc. for real-time applications.

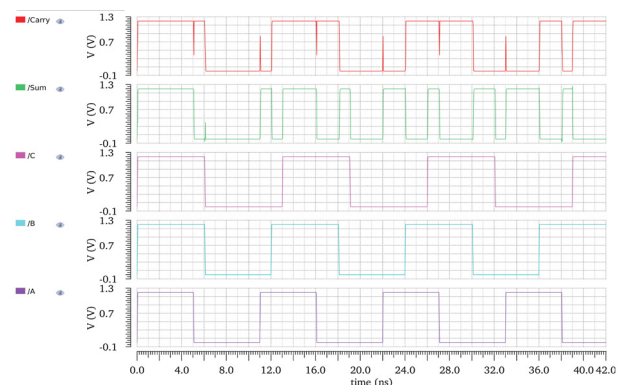


Figure 9: Proposed FA 1 Transient Analysis waveform

From the Table 2, we observed that average delay of proposed logic 2 is 165.81ps and it is smaller than all other logics. Rahimi [26] and Mehedi [22] full adder cells average delay are 172.62ps and 173.37ps respectively. In power dissipation part, EEPL consumes 323.05 μ W power and it is the lower than all other logics. Our proposed logic 2 and Naseri (HFA-22T) [21] consumes average power of 350.82 μ W and 355.94 μ W respectively. While considering the PDP, proposed full adder 2 has 0.0582pJ and followed by Mehedi [22] and Rahimi [26].

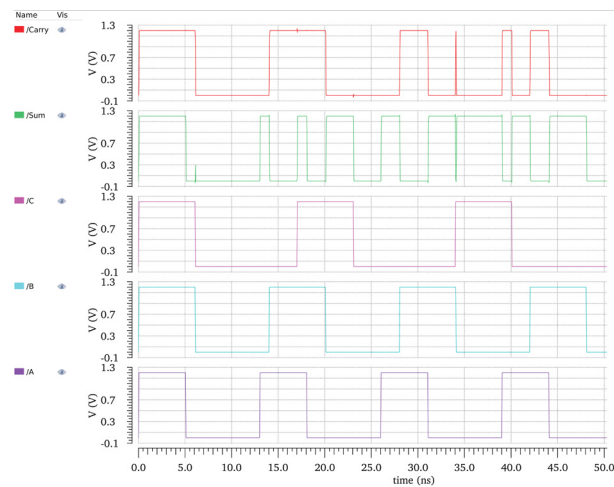


Figure 10: Proposed FA 2 Transient Analysis waveform

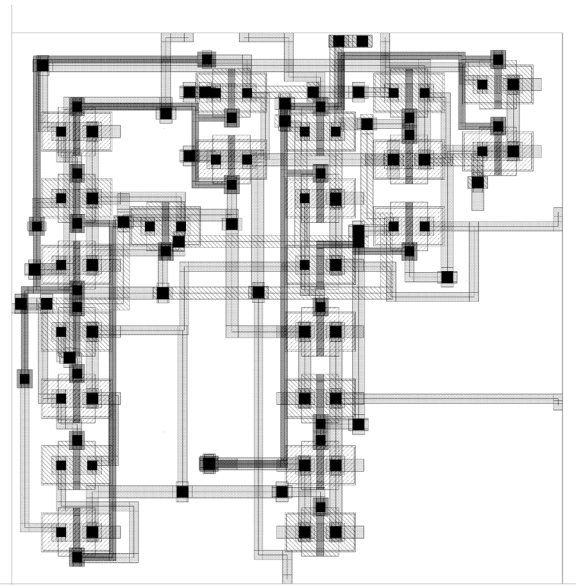


Figure 11: Proposed Full Adder 1 Layout

From previous literatures we observed that, mux based alternative structures and DPL significantly reduces the propagation delay. Also DPL consumes lesser power compared to other conventional logic, due to reduced switching activity. Observed results from Table 2 shows that our proposed logics based on Multiplexer and DPL significantly reduces the power and propagation delay.

Table 2: Comparison of simulation results of various FA cells in 45nm technology

S. No.	Name of the FA Cell	Delay (ps)			Avg. Power (μ W)	Avg. PDP (pJ)	Transistors Count	Area (μm^2)
		Avg. Delay	Maximum Delay	Minimum Delay				
1	Conventional CMOS	280.25	341.35	227.99	362.41	0.1016	28	18.85
2	CMOS TG	321.09	410.38	268.16	394.36	0.1266	16	11.63
3	Pseudo nMOS	332.95	434.29	307.86	476.27	0.1586	18	13.54
4	12-Transistor	289.55	366.38	245.22	395.62	0.1146	12	8.08
5	PTL	256.09	319.58	225.00	412.27	0.1056	16	11.17
6	CPL	294.97	381.92	249.80	408.56	0.1205	32	20.25
7	SR-PL	271.71	334.36	223.80	372.03	0.1011	28	18.86
8	SR-CPL	244.772	280.92	186.98	338.79	0.0829	26	16.33
9	DPL	198.00	264.68	174.18	378.23	0.0749	48	30.63
10	CVSL	245.10	315.24	216.51	395.07	0.0968	27	17.70
11	DCVL	228.28	296.29	197.42	380.48	0.0869	30	20.46
12	DCVSPG	214.85	276.04	178.97	366.96	0.0788	28	18.71
13	EEPL	352.12	448.03	292.12	323.05	0.1138	32	20.81
14	Naseri (HFA-22T) [21]	188.69	237.92	159.35	355.94	0.0672	22	14.32
15	Mehedi [22]	173.37	220.14	144.25	369.623	0.0641	22	13.68
16	Jyoti [23]	199.68	249.22	166.18	365.67	0.0730	20	13.85
17	Sharmila [24]	221.65	280.32	186.80	399.12	0.0885	27	17.57
18	Azeem [25]	208.15	258.34	173.33	396.05	0.0824	14	9.04
19	Rahimi [26]	172.62	216.91	144.63	373.49	0.0645	9	5.59
20	Proposed Logic 1	176.51	217.04	145.38	384.39	0.0678	22	14.04
21	Proposed Logic 2	165.81	204.00	136.56	350.82	0.0582	30	20.19

The lower PDP of the proposed full adder 2 more useful in constructing the energy efficient high speed circuits for portable devices. Figure 14 and Figure 15 show the graphical comparison of Average value of Delay, Power and PDP for the various full adder cells.

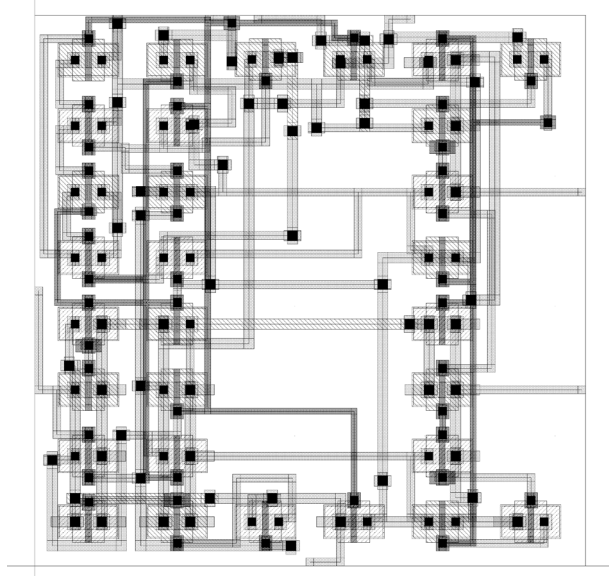


Figure 12: Proposed Full Adder 2 Layout

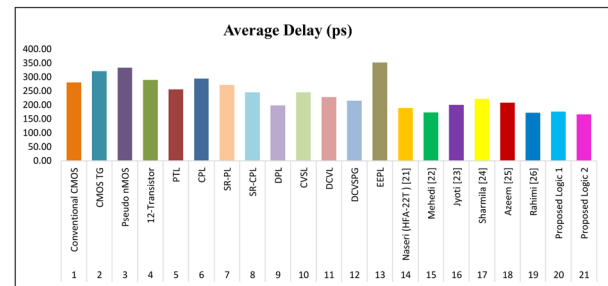


Figure 13: Average Delay Comparison of Various FA cells

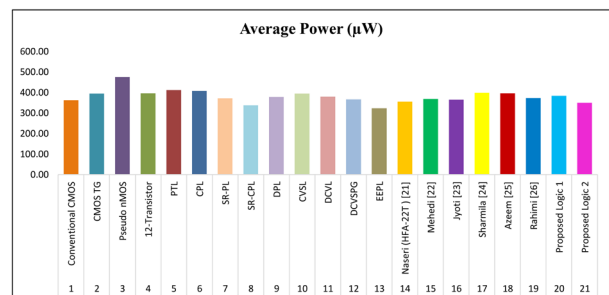


Figure 14: Average Power Comparison of Various FA cells

Table 3: Proposed FA 2 performance improvements with other logics

Sl. No.	Name of the FA Cell	% of Improvement for Proposed Logic 2			
		Avg. Delay	Avg. Power	Avg. PDP	Area
1	Conventional CMOS	69.017	3.304	74.602	-6.667
2	CMOS TG	93.644	12.410	117.677	-42.381
3	Pseudo nMOS	100.797	35.760	172.602	-32.929
4	12-Transistor	74.626	12.769	96.924	-59.964
5	PTL	54.445	17.517	81.500	-44.667
6	CPL	77.891	16.459	107.171	0.286
7	SR-PL	63.866	6.045	73.771	-6.583
8	SR-CPL	47.620	-3.430	42.556	-19.137
9	DPL	19.414	7.812	28.742	51.714
10	CVSL	47.820	12.615	66.467	-12.330
11	DCVL	37.671	8.455	49.312	1.339
12	DCVSPG	29.571	4.601	35.532	-7.333
13	EEPL	112.363	-7.916	95.553	3.048
14	Naseri (HFA-22T) [21]	13.797	1.459	15.456	-29.089
15	Mehedi [22]	4.555	5.360	10.159	-32.232
16	Jyoti [23]	20.426	4.234	25.525	-31.429
17	Sharmila [24]	33.674	13.767	52.076	-12.973
18	Azeem [25]	25.532	12.892	41.715	-55.208
19	Rahimi [26]	4.106	6.463	10.834	-72.298
20	Proposed Logic 1	6.453	9.569	16.640	-30.464

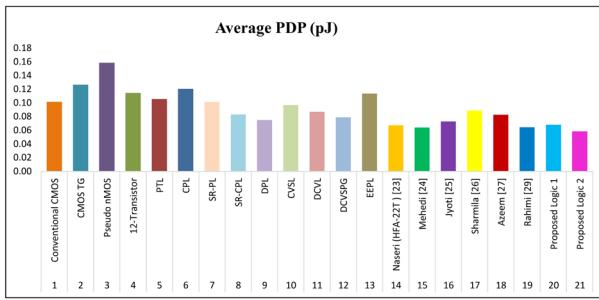
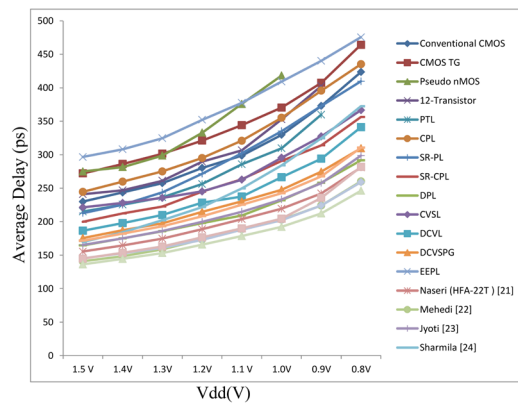
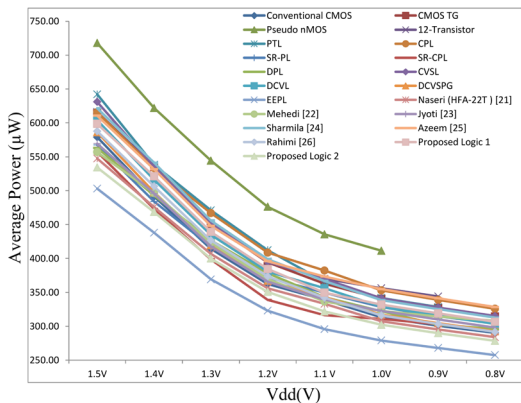


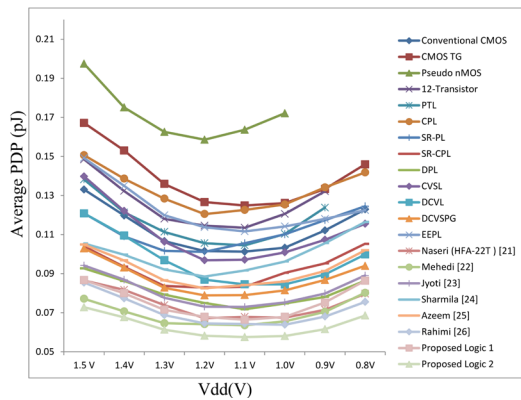
Figure 15: Average PDP Comparison of Various FA cells



(a) Delay



(b) Power



(c) PDP

Figure 16: FA Cells simulation results for different V_{DD} levels

Table 3 shows the proposed full adder cells performance improvement in various parameters. Since proposed full adder 2 is constructed with 30 transistors, the area requirement is significantly more than other logics. While comparing with other parameters, the proposed FA cell 2 is superior to other logics. The full adder cells efficiency and robustness can be analysed by varying the bias voltage (V_{DD}). To perform this, bias voltage is adjusted from 1.8V to 0.8V with 45nm CMOS technology and transient outputs were analysed.

Other than Pseudo nMOS, 12-Transistor and PTL, all the full adders are producing correct output in this range. Pseudo nMOS producing correct output up to 1V and 12-Transistor and PTL are producing correct output up to 0.9V. Our proposed full adders 1 and 2 are producing the output without any signal degradation upto 0.9V supply voltage and small degradation present in the 0.8V supply voltage.

In this paper, we analysed average value of power, delay and PDP of all the FA cells by varying the supply voltage. Figure 16 illustrates the FA Cells simulation results for different V_{DD} levels. From the figures, we can understand that as the V_{DD} decreases, the propagation delay increases, and power dissipation decreases. However, the PDP value initially decreases, and after reaching the voltage level of 1.2 to 1.1, it begins to increase.

Experimental observations showed that proposed full adder 2 along with Mehedi [22] and Rahimi [26] full adders PDP values are almost equal for the V_{DD} ranging from 1.0V to 1.3 V which makes these full adders suitable for operating at wide range of power supply values. Also it is observed that lessening V_{DD} causes the drop in power consumption and rise in propagation delay. The PDP value is decreased while reducing supply voltage (V_{DD}) up to 1.1 V to 1.0V range and then it begins to increase.

In the field of IC design, the attention to process corners holds significant importance as it allows designers to assess the reliability and robustness of the designed circuits under diverse manufacturing conditions. By Investigating various Process Corners will help to identify the key challenges associated with vital performance parameters such as Speed, Power Consumption, and etc. This analysis assures that the proposed design meets required specifications under the influence of different operating conditions. Nominal - Nominal (NN) or Typical - Typical (TT), Slow - Slow (SS), Fast - Slow (FS), Slow - Fast (SF) and Fast - Fast (FF) are the process corners present to analyse the circuits. In Cadence ADE, various Process Corners were chosen, and simulations were carried out to determine the Average Delay, Power, and Power-Delay Product. These simulations were

performed to determine the circuit's feasibility under various environments. Figure 17 depicts the performance of FA cells for different process corners. In the FF process corner setup, all the FA cells operate with minimal delay and consume more power. Alternatively, in the SS process corner setup, FA cells operate with increased propagation delay and lower power. Proposed Full adder 2 achieved lowest PDP of 0.0321pJ and 0.0582pJ in FF and TT corners. Naseri (HFA-22T) [21] achieved minimum PDP 0.051129pJ in FS process corner. Mehedi [22] full adder achieved 0.0621pJ in SF process corner. Rahimi [26] full adder achieved 0.0815pJ in SS process corner.

Noise tolerance is an imperative property for any integrated circuits to ensure reliable operation, maintain

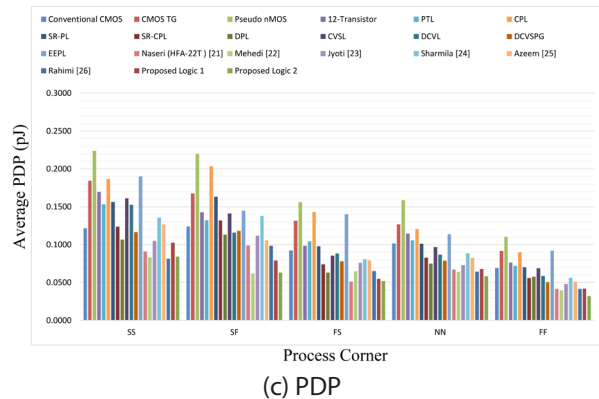
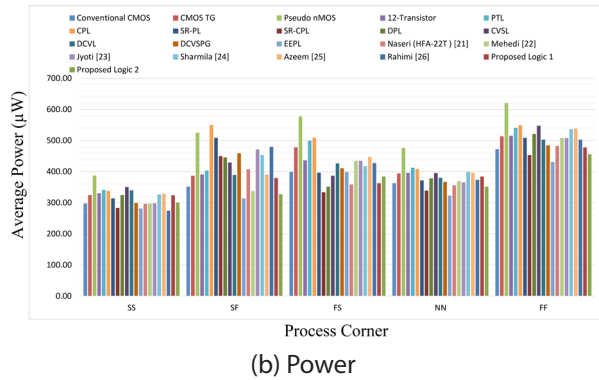
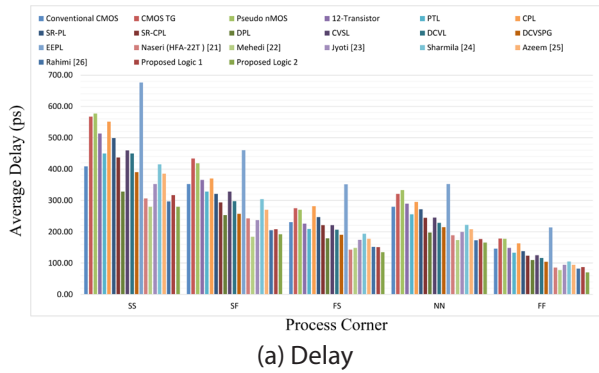


Figure 17: Various Process Corners vs Delay, Power and PDP

signal integrity, and prevent performance degradation due to various external factors. Designing any ICs with strong noise tolerance is the key factor to the overall success and correct functionality of electronic devices. Noise tolerance parameter will help to evaluate the ability of digital circuits to withstand to the influences of the noise signal. Both CPL and DPL offer better noise immunity compared to other logics. Differential operations due to Complementary pairs of Pass Transistors present in the CPL provide inherent noise immunity. DPL further improves the noise immunity by double passing of signals. This means that signals pass through the gates twice (i.e same logic implemented by two different logic gates), effectively amplifying the signal and minimizing the impact of noise.

Noise pulses with high amplitude and significantly large width in ICs may create unwanted switching, potentially causing the circuit to malfunction. In this article, Katopis [30] Noise Immunity Curve (NIC) was obtained to evaluate the noise tolerance of different Full adder circuits in response to noise input. A logical error will occur at the locus point (T_n , V_n) for the gate, where T_n represents the noise pulse duration and V_n represents the noise pulse's amplitude.

Average Noise Threshold Energy (ANTE) metric [31] is the quantitative value of noise tolerance and it is computed from the NIC.

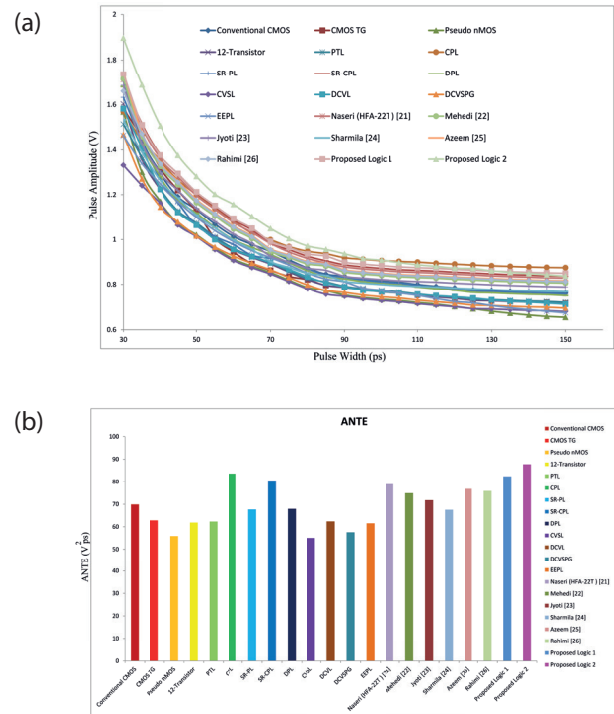


Figure 18: (a) NIC for various FA Cells (b) ANTE for various FA Cells

$$ANTE = E(V_n^2 T_n) \quad (3)$$

$$ANTE = (V_1^2 T_1 + V_2^2 T_2 + \dots V_n^2 T_n) / n \quad (4)$$

Figure 18 shows that NIC plot and ANTE for full adder circuits discussed in this paper. The higher ANTE value represents that the circuit has better Noise immunity. The proposed full adder 2 and full adder 1 have the ANTE value of 87.72 and 82.32. As we discussed earlier, the our DPL based logics have better noise immunity than other logics.

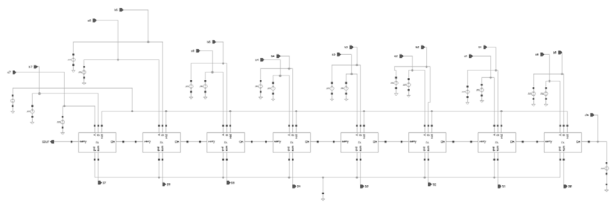


Figure 19: 8 bit Parallel Adder using proposed full adder 2

The functionality verification of our proposed full adder 2 for higher order bits is done by designing a 8-bit parallel adder (Ripple Carry Adder). Figure 19 shows that the 8-bit parallel adder implementation using cadence virtuoso schematic editor. The 8-RCA has average delay, power and PDP of 1485.68ps, 3690.618μW and 0.589613pJ.

5 Conclusion

In this paper, two novel full adder structures based alternative logic using double pass transistor have been proposed. The alternative logic is implemented by separate XOR/XNOR structure to increase speed of the circuit. Our proposed Full Adder cells performances are compared with 19 various conventional adders including C-CMOS, CMOS TG, PTL and recently reported hybrid full adders. The various simulations were performed by Cadence EDA tools with 45nm CMOS technology. The proposed FA Cell 2 has minimum of 10.16% improvement with respect to PDP value. The average delay of the proposed full adder 2 is minimal than all other logics and the average power of the proposed full adder 2 is superior to that of all other logics, except for EEPL. All the FA cells were simulated under different supply voltage ranges from 0.8V to 1.5V and our proposed full adders performed well in those conditions. Simulations were conducted in various process corners and our proposed full adder 2 shows highest performance with respect to PDP in NN and FF process corners. In other process corners, both the full adders have lower PDP value than most of the logics. The noise

immunity of circuits is measured using NIC and ANTE and our proposed full adder 2 has highest ANTE value. Also both the full adders are less susceptible to noise when simulated by a noise pulse width 150ps and below. Our proposed designs offer practical insights into improve the circuit performance in developing the modern electronic systems. Also they pave the way for the realizing faster and energy-efficient computing structures in various domains such as digital signal processing, communication systems, and embedded computing. Additionally, the robust performance of our FA cell across different supply voltages and process corners ensures their suitability for diverse applications in both high-performance computing and low-power embedded systems. Further investigation can be done by exploring various optimization techniques to improve the performance and efficiency of the proposed full adders. Also, investigating full adder cells compatibility for emerging semiconductor technologies, such as advanced CMOS nodes or alternative materials, may provide the insights for future computing systems.

6 Conflict of Interest

The authors declare no conflict of interest.

7 References

1. Mehedi Hasan, Abdul Hasib Siddique, Abdal Hoque Mondol, Mainul Hossain, Hasan U. Zaman and Sharnali Islam, "Comprehensive study of 1-Bit full adder cells: review, performance comparison and scalability analysis", SN Applied Sciences 3:644 (2021).
<https://doi.org/10.1007/s42452-021-04640-2>.
2. M. Aguirre-Hernandez and M. Linares-Aranda, "CMOS Full-Adders for Energy-Efficient Arithmetic Applications," in IEEE Transactions on Very Large Scale Integration (VLSI) Systems, vol. 19, no. 4, pp. 718-721, April 2011.
<https://doi.org/10.1109/TVLSI.2009.2038166>
3. Neil H. E. Weste and David Money Harris, "CMOS VLSI Design- A Circuits and Systems Perspective", Fourth Edition, Pearson Publication, 2010.
4. Thiruvengadam Rajagopal and Arvind Chakrapani, "A Novel High-Performance Hybrid Full Adder for VLSI Circuits", Circuits, Systems, and Signal Processing 40, 5718–5732 (2021).
<https://doi.org/10.1007/s00034-021-01725-6>.
5. Mingyan Zhang, Jiangmin Gu and Chip-Hong Chang, "A novel hybrid pass logic with static CMOS output drive full-adder cell," 2003 IEEE International Symposium on Circuits and Systems

- (ISCAS), Bangkok, Thailand, pp. V-317 – V-320, 2003.
<https://doi.org/10.1109/ISCAS.2003.1206266>
6. B. C. Devnath and S. N. Biswas, "An Energy-Efficient Full-Adder Design Using Pass-Transistor Logic," 2019 2nd International Conference on Innovation in Engineering and Technology (ICIET), Dhaka, Bangladesh, 2019, pp. 1-6.
<https://doi.org/10.1109/ICIET48527.2019.9290550>.
7. M. Rahimi and M.B. Ghaznavi-Ghouschi, "A fanout-improved Parallel Prefix Adder with full-swing PTL cells and Graded Bit Efficiency", Microelectronics Journal, vol. 113, 2021.
<https://doi.org/10.1016/j.mejo.2021.105086>.
8. Nan Zhuang and Haomin Wu, "A New Design of the CMOS Full Adder" IEEE Journal of Solid-State Circuits, vol. 27, no. 5, May 1992.
<https://doi.org/10.1109/4.133177>.
9. Zarin Tabassum, Meem Shahrin, Anika Ibnat, Tawfiq Amin, "Comparative Analysis and Simulation of Different CMOS Full Adders Using Cadence in 90 nm Technology" 2018 3rd International Conference for Convergence in Technology (I2CT), Pune, India, Apr 06-08, 2018.
<https://doi.org/10.1109/I2CT.2018.8529482>.
10. Fang Lu and Henry Samueli, "A High-Speed CMOS Full-Adder Cell using a New Circuit Design Technique – Adaptively-Biased Pseudo-Nmos Logic", IEEE International Symposium on Circuits and Systems, pp. 563-565, May 1990.
<https://doi.org/10.1109/ISCAS.1990.112118>
11. Reto Zimmermann and Wolfgang Fichtner, "Low-Power Logic Styles: CMOS Versus Pass-Transistor Logic" IEEE Journal of Solid-State Circuits, vol. 32, no. 7, July 1997.
<https://doi.org/10.1109/4.597298>.
12. K.T. Lau, "Digital IC functions with Differential Cascode Voltage Switch Circuits", IEEE Transactions on Consumer Electronics, vol 34, Issue: 4, November 1988.
<https://doi.org/10.1109/30.9901>.
13. Lixin Gao, "High Performance Complementary Pass Transistor Logic Full Adder", 2011 International Conference on Electronic & Mechanical Engineering and Information Technology, pp. 4306 – 4309, August, 2011.
<https://doi.org/10.1109/EMEIT.2011.6023114>
14. Fang-shi Lai and Wei Hwang, "Design and Implementation of Differential Cascode Voltage Switch with Pass-Gate (DCVSPG) Logic for High-Performance Digital Systems", IEEE Journal of Solid-State Circuits, vol 32, Issue:4, pp. 563 – 573, April 1997.
<https://doi.org/10.1109/4.563678>.
15. M. Suzuki, N. Ohkubo, T. Shinbo, T. Yamanaka, A. Shimizu, K. Sasaki and Y. Nakagome, "A 1.5-ns 32-b CMOS ALU in double pass-transistor logic", IEEE Journal of Solid-State Circuits, vol. 28, no. 11, pp. 1145-1151, November 1993.
<https://doi.org/10.1109/4.245595>
16. A. Parameswar, H. Hara and T. Sakurai, "A swing restored pass-transistor logic-based multiply and accumulate circuit for multimedia applications", IEEE Journal of Solid-State Circuits, vol 31, Issue: 6, pp. 804 – 809, June 1996.
<https://doi.org/10.1109/4.509866>.
17. T. Bhagyalaxmi, S. Rajendar, S. Srinivas, "Power-Aware Alternative Adder Cell Structure Using Swing Restored Complementary Pass Transistor Logic at 45nm Technology", 2nd International Conference on Nanomaterials and Technologies (CNT 2014), Procedia Materials Science, vol 10, 789 – 792, 2015.
<https://doi.org/10.1016/j.mspro.2015.06.02>
18. Minkyu Song, Geunsoon Kang, Seongwon Kim, Euro Joe and Bongsoon Kang, "Design of a low power 7-bit serial counter with Energy economized pass-transistor logic (EEPL)", ICECS'96, Proceedings of Third International Conference on Electronics, Circuits and Systems, October 1996.
<https://doi.org/10.1109/ICECS.1996.584563>.
19. Yingtao Jiang, Abdulkarim Al-Sheraidah, Yuke Wang, Edwin Sha, and Jin-Gyun Chung, "A Novel Multiplexer-Based Low-Power Full Adder", IEEE Transactions on Circuits and Systems—II: Express Briefs, vol. 51, no. 7, pp. 345-348, July 2004.
<https://doi.org/10.1109/TCSII.2004.831429>.
20. Pankaj Kumar and Rajender Kumar Sharma, "Low voltage high performance hybrid full adder", Engineering Science and Technology, an International Journal, vol 19, Issue 1, Pages 559-565, March 2016.
<https://doi.org/10.1016/j.jestch.2015.10.001>
21. Hamed Naseri and Somayeh Timarchi, "Low-Power and Fast Full Adder by Exploring New XOR and XNOR Gates", IEEE Transactions on Very Large Scale Integration (VLSI) Systems, vol: 26, Issue: 8, pp. 1481 – 1493, August 2018.
<https://doi.org/10.1109/TVLSI.2018.2820999>.
22. Mehedi Hasan, Md. Shahbaz Hussain, Mainul Hossain, Mohd. Hasan, Hasan U. Zaman and Sharnali Islam, "A high-speed and scalable XOR-XNOR-based hybrid full adder design", Computers & Electrical Engineering, vol. 93, July 2021.
<https://doi.org/10.1016/j.compeleceng.2021.107200>.
23. Jyoti Kandpal, Abhishek Tomar and Mayur Agarwal, "Design and implementation of 20-T hybrid full adder for high-performance arithmetic applications", Microelectronics Journal, vol 115, September 2021.
<https://doi.org/10.1016/j.mejo.2021.105205>.

24. S. Sharmila Devi and V. Bhanumathi, "Design of reversible logic based full adder in current-mode logic circuits", *Microprocessors and Microsystems*, vol 76, July 2020.
<https://doi.org/10.1016/j.micpro.2020.103100>
25. Azeem Mohammed Abdul , N.V.S.S. Prasanna, K.V. Harish Kumar and K. Banu Teja, "14-T hybrid full adder design and its implementation for high-performance arithmetic applications", *Materials Today: Proceedings*, vol 69, Part 2, Pages 454-458, 2022.
<https://doi.org/10.1016/j.matpr.2022.09.137>.
26. Parisa Rahimi, Myasar Tabany and Seyedali Pourmoafi "A Novel Low Power and High Speed 9-Transistors Dynamic Full-Adder Cell Simulation and Design", 2023 IEEE Symposium on Computers and Communications (ISCC), page 1287-1292, 2023.
<https://doi.org/10.1109/ISCC58397.2023.10217831>.
27. M. Aguirre and M. Linares, "An alternative logic approach to implement high-speed low-power full adder cells," in *Proc. SBCCI*, Florianopolis, Brazil, pp. 166–171, Sep. 2005.
<https://doi.org/10.1109/SBCCI.2005.4286851>.
28. Rajesh S . Parthasarathy and Ramalingam Sridhar, "Double Pass-Transistor Logic for High Performance Wave Pipeline Circuits", *Proceedings Eleventh International Conference on VLSI Design*, Chennai, India, 04-07 January 1998.
<https://doi.org/10.1109/ICVD.1998.646655>.
29. Uming Ko, Poras T. Balsara, and Wai Lee, "Low-Power Design Techniques for High-Performance CMOS Adders," *IEEE Transactions on VLSI Systems*, Vol. 3, No. 2, June 1995.
<https://doi.org/10.1109/92.386232>.
30. G. A. Katopis, "Delta-I noise specification for a high-performance computing machine," in *Proceedings of the IEEE*, vol. 73, no. 9, pp. 1405-1415, Sept. 1985.
<https://doi.org/10.1109/PROC.1985.13301>.
31. Sriram Sundar S, Mahendran G, "CMOS full adder cells based on modified full swing restored complementary pass transistor logic for energy efficient high speed arithmetic applications", *Integration*, Volume 95, 2024.
<https://doi.org/10.1016/j.vlsi.2023.102132>.



Copyright © 2024 by the Authors.
This is an open access article distributed under the Creative Commons Attribution (CC BY) License (<https://creativecommons.org/licenses/by/4.0/>), which permits unrestricted use, distribution, and reproduction in any medium, provided the original work is properly cited.

Arrived: 07. 02. 2024

Accepted: 24. 05. 2024

A Novel Method for 5Generation Multiple-Input, Multiple-Output Orthogonal Frequency-Division Multiplexing using Cauchy Evading Golden Tortoise Adaptive-Bi Directional-Long Short-Term Memory

Poornima Ramamoorthy^{1*}, Kalaivani Ramanathan²

¹Department of Electronics and Communication Engineering, SNS College of Technology, Coimbatore, Tamil Nadu, India.

²Department of Electronics and Communication Engineering, Erode Sengunthar Engineering College, Perundurai, Tamil Nadu, India.

Abstract: Multiple-Input Multiple Output Orthogonal Frequency Division Multiplexing (MIMO-OFDM), which could provide a large number of antennas, is one among the key technologies of 5G. For recovering the transmitted symbols at the receiver, a key role is played by the Channel Estimation (CE) in MIMO-OFDM. But it is indisputable recently. Hence, a novel method for 5G MIMO-OFDM CE using Cauchy Evading Golden Tortoise Adaptive-Bi Directional-Long Short-Term Memory (CEGTA-Bi-LSTM) is proposed. Primarily, input like text, video, and audio are given for the encoding process at the transmitter; in addition, it is encoded using the Gaussian Distribution-Low Density Parity Check (GD-LDPC) algorithm. Then, by employing Combined Bits-Quadrature Phase Shift Keying (CB-QPSK), the signal is modulated. Next, the output is inputted into the pulse shaping, which is conducted by deploying Truncated Linear-Raised Cosine Filter (TL-RCF). The pulse-shaped signal is fed into the pilot insertion phase where the reference signal is inserted. Afterward, the signal is inputted into the Entropy-Inverse Fast Fourier Transform (E-IFFT) phase. Next, the output from the E-IFFT passes through the channel with AWGN noise; also, it is given to the receiver phase in which the reverse process of the transmitter occurs. Then, from the receiver output, the channel is estimated. The proposed CEGTA-Bi-LSTM is implemented using MATLAB simulation. The experimental results show that, the proposed method decrease the Mean Squared Error (MSE) by 0.7%, 1.6%, 2.6% lower than Bi-directional Long Short-Term Memory (Bi-LSTM), Long Short-Term Memory (LSTM), Least Squares (LS), and Minimum Mean Square Error (MMSE) respectively.

Keywords: MIMO-OFDM; 5G; Channel Estimation; transmitter

Nova optimizacijska metoda izogibanja zlati želvi za oceno MIMO OFDM 5G kanala

Izveček: Več vhodni in več izhodni ortogonalni frekvenčni multiplekser (MIMO-OFDM), ki lahko zagotovi veliko število anten, je ena od ključnih tehnologij 5G. Za obnovitev poslanih simbolov v sprejemniku ima pri MIMO-OFDM ključno vlogo ocenjevanje kanala (CE). Predlagana je nova metoda za 5G MIMO-OFDM CE z uporabo izogibanja zlati želvi (CEGTA-Bi-LSTM). Vhodni podatki, kot so besedilo, video in zvok, so v prvi vrsti dani za postopek kodiranja na oddajniku; poleg tega se kodirajo z algoritmom Gaussian Distribution-Low Density Parity Check (GD-LDPC). Nato se signal modulira z uporabo kombiniranega bitno-kvadraturnega faznega premikanja ključev (CB-QPSK). Izhodni signal se vnese v oblikovanje impulzov, ki se izvede z uporabo skrajšanega linearnega dvignjenega kosinusnega filtra (TL-RCF). Impulzno oblikovani signal se vodi v fazo vstavljanja pilotnega signala, v katero se vstavi referenčni signal. Po entropijski obratni Fourierova transformaciji (E-IFFT), preide signal skozi kanal s šumom AWGN; prav tako se posreduje v fazo sprejemnika, v kateri se izvede obraten postopek kot pri oddajniku. Nato se na podlagi izhoda sprejemnika oceni kanal. Eksperimentalni rezultati kažejo, da predlagana metoda zmanjša srednjo kvadratno napako (MSE) za 0,7 %, 1,6 % in 2,6 % v primerjavi z dvosmernim dolgotrajnim spominom (Bi-LSTM), dolgotrajnim spominom (LSTM), najmanjšo kvadratno napako (LS) in najmanjšo srednjo kvadratno napako (MMSE).

Ključne besede: MIMO-OFDM; 5G; ocenjevanje kanala; oddajnik

* Corresponding Author's e-mail: poornima7654@outlook.com

How to cite:

P. Ramamoorthy et al., "A Novel Method for 5Generation Multiple-Input, Multiple-Output Orthogonal Frequency-Division Multiplexing using Cauchy Evading Golden Tortoise Adaptive-Bi Directional-Long Short-Term Memory", Inf. Midem-J. Microelectron. Electron. Compon. Mater., Vol. 54, No. 3(2024), pp. 201–213

1 Introduction

An antenna technology, which includes a huge number of antennas at the Base Station (BS), for serving various User Terminals (UTs) is termed a MIMO [1]. Users can be served by MIMO in the same time-frequency resources; hence, (A) spectrum efficiency, (B) energy efficiency, (C) spatial resolution, along with (D) network coverage can be enhanced. For the 5G and future wireless communication networks, it is considered as an optimistic technique owing to its merits [2]. High Spectral Efficiency (SE), high data rate, and low latency are encompassed in 5G networks; in addition, they could connect more different devices, make businesses and industries more efficient and give consumers access to more information faster than ever before [3]. Besides, Wireless network suffers from certain challenges, namely frequency-selective fading, and dispersion. Dynamic tolerance of fading and dispersion is the key reason behind OFDM [4, 5]. In next-generation wireless communication systems, for tackling the ever-growing demands for higher SE, fusing massive MIMO with OFDM is a solution [6]. CE is required to obtain the signal transmission exactly in MIMO-OFDM. In wireless systems, CE is a challenging problem owing to the noise effect and time-varying of wireless channels [7]. Thus, the '2' CE methodologies like pilot tone-centric CE approach and blind or semi-blind CE are wielded to deal with this [8]. For acquiring the minimal mean square error, the pilot sequence and tones were optimized in the pilot tone estimation system; in addition, the system's estimation accuracy is liable to noise along with inter-carrier interference [9]. In the target cell, data of different users are sequentially detected by the blind or Semi-blind estimator along with formulates a constrained minimization issue for each user [10]. Some of the conventional approaches based on neural networks are fairly complex; also, require a large number of parameters to be trained with large datasets in DL [11]. Moreover, a lot of computational resources are required by a few machines learning-based algorithms. For estimating the relevant channel state, these approaches are not perfect. Thus, this paper proposes a new method for 5g MIMO-OFDM CE using the CEGTA-Bi-LSTM framework.

1.1 Problem statement

For solving the problem of CE, prevailing research methodologies have many ideas but still improvements are needed. Existing research methodologies have some drawbacks, which are described as follows,

- Least Squares (LS) estimation has comparatively higher estimation error owing to its low cost devoid of any prior statistical information concerning the channel, although it is hugely deployed for acquiring channel estimates.

- During ISI mitigation, the cyclic prefix's usage to avoid Inter Symbol Interference (ISI) introduces a loss in the SNR of the received signal.
- Most of the baseline CE techniques use QAM for signal modulation. However, the disadvantages of such a technique are that it is more prehensible to noise. Due to this QAM, the receiver is more difficult compared to receivers of other modulations for the process of secure transmission.
- CE models used in existing frameworks require prior knowledge of channel statistics. This makes the optimal channel predictor highly complex.

1.2 Objectives

In the existing CE model, the aforementioned loopholes can be overcome by proposing a novel method for 5G MIMO-OFDM CE using the CEGTA-Bi-LSTM framework. The research objectives of the proposed framework are listed as follows,

- For secure transmission between multipath channels, a GD-LDPC encoding model is introduced to encode the input.
- To propose a CB-QPSK modulation method for reducing the SER.
- A TL-RCF is utilized to alleviate ISI and prevents information loss.
- To model a novel DL-based CE technique by considering statistical channel properties with low estimation error using CEGTA-Bi-LSTM.

The remaining part is arranged as: the related works to the proposed methodology are elucidated in section 2; the proposed research methodology is delineated as in section 3; the experimental perusal is exhibited in section 4; the paper is winded up with the future work in section 5.

2 Related work

In 2021, Mashhadi & Gunduz, [12] recommended a neural network (NN)-centric joint pilot design and downlink CE system for Frequency Division Duplex (FDD) MIMO-OFDM systems. For frequency-aware pilot design, fully connected layers were deployed. By assigning pilots across subcarriers non-uniformly, the pilot overhead was effectively minimized. Channel statistics were required by the deployed CE. It made the presented method highly complicated.

In 2019, Kansal et al., [13] presented an innovative solution, which fuses OFDMA technologies with multi-user massive MIMO technology. Source encoding, channel encoding, interleaving, and modulation were included here. The highest SE was offered by the technique.

When weighed against the Fast Fourier Transform (FFT), this system grounded on the fractional Fourier transform (FRFT) provides lower SNR of 8–13 dB.

In 2019, Mehrabi et al., [14] developed a fresh DL-centric Decision-Directed-CE (DD-CE) for tracking fading channels and detecting data for longer packets even in fast vehicular environments and studied DD-CE systems. This technique profited from an easy receiver design, which didn't depend on the fading channel's precise statistical model. The requirement for Doppler rate estimation was removed by the system's ability, which was challenging for highly dynamic vehicular environments.

In 2022, et al., [15] recommended a fresh sort of pilot sequences with diverse modulation orders to enhance spectrum efficiency. In MIMO-OFDM systems, the developed variable pilot-assisted CE was espoused with lower along with higher-order modulations. As per the simulation outcomes, for MIMO-OFDM systems' BER performance, this technique had 1–2 dB SNR gains. This system's CE was verified just in a single field; thus, unreliable CE might be offered.

In 2021, Cheng et al., [16] presented a combined time-variant Carrier Frequency Offset (CFO) along with frequency-selective channel response estimation for MIMO-OFDM for mobile users. The MIMO-OFDM's signal model was presented; in addition, as per the maximal likelihood criterion, the joint estimator was derived. When analogized to the grid search-centric technique, this system had lower computational complexity. However, it was deployed at higher mobile speeds.

In 2020, Mata & Boonsrimuang, 2020 [17] developed an effectual CE technique for a massive MIMO-OFDM system. The discrete Fourier transform estimator (DFE), which appraised the MIMO channels accurately, was deployed. It had elevated estimation accuracy along with superior BER with lower-complexity MIMO data detection. A lower transmission data rate of 32.5 Mbps was acquired.

In 2020, SURIAVEL RAO & Malathi, [18] explored a cyclic prefix-centric estimation system for carrier frequency offset, which was estimated in fusion with an actual evolutionary Cuckoo Search technique centered on the received carrier phase angle together with cyclic prefix information for efficient optimization. As per the outcomes, noise estimation along with compensation was enhanced. But, for facilitating the system's self-learning ability, this system had complex computations.

In 2021, Gao et al., [19] constructed an uplink transmission scheme in crowded linked cell-free massive

MIMO-OFDM with fewer orthogonal pilots. For detecting active User Equipment (UEs), pilot phase shift hopping patterns were wielded for the pilot transmission. In median and 95%-likely performance, the minimal SE was enhanced among active UEs. But it was not reliable since it was apt just for crowded cell-free massive MIMO-OFDM systems.

In 2021, Riadi et al., [20] developed a least squares CE (LSCE) in the Uplink transmission for Massive MIMO in 5G wireless communications merged with Orthogonal Frequency Division Multiplexing together with higher-order M-ary quadrature amplitude modulation (M-QAM) modulation. As per the simulation outcomes, the MMSE along with Zero-Forcing (ZF) detectors' performance was just less than 1 dB. Several antennas were deployed; thus, various RF modules were caused.

In 2022, Jothi & Chandrasekar, [21] introduced a MIMO-OFDM multimedia model with very low power consumption, which offered superior energy-efficacy. For delivering augmented QoS, the MIMO methodology was fused into an OFDM for multimedia wireless communication. The system's superiority lies in the 40% augmentation of processing time along with the 94% enhancement in energy efficiency at 25W in the 35th iteration. This system was not feasible since the system acquired low outcomes.

3 Proposed channel estimation using CEGTA-BI-LSTM in 5G

Owing to the DL's better potential, it has been employed for CE. Nevertheless, it is indisputable that the foundation of the overall network-level performance is

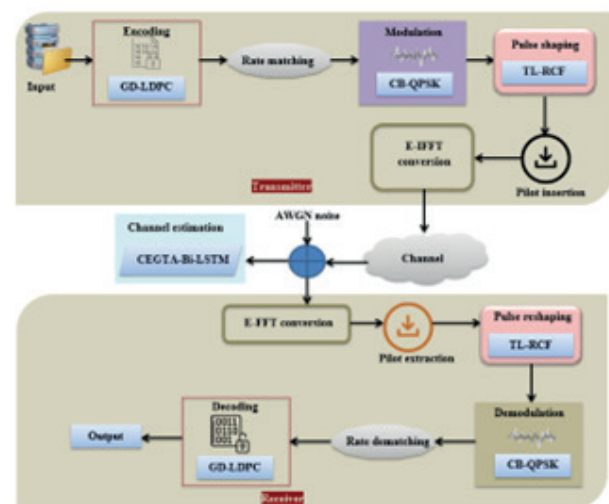


Figure 1: Proposed architecture for the channel estimation in 5G.

set by the processing employed in the physical layer. Hence, this paper proposes a new technique of MIMO-OFDM CE using CEGTA-Bi-LSTM in 5G wireless communication. In Figure 1, the proposed methodology's block diagram is depicted.

3.1 Transmitter

Here, the input file is given as input. Next, in the transmission process, the encoding, rate matching, modulation, Pulse shaping, Pilot insertion, and E-IFFT conversion occurs.

3.1.1 Input

Primarily, the input files from public resources are inputted into the proposed structure. It is equated as,

$$\zeta = \{\zeta_1, \zeta_2, \zeta_3, \dots, \zeta_b\} \text{ or } \zeta_a, a = 1, 2, 3, \dots, b \quad (1)$$

Here, the total number of inputs is signified as ζ_a and the input file with b number of inputs is depicted as a .

3.1.2 Encoding

The input (ζ_a) is given as a matrix form to the encoding phase. Here, by employing the GD-LDPC, the inputs are encoded. For transmitting the data securely, encoding is deployed. A large message block is divided into several code blocks with a length of the code block in the LDPC model. Zeros will be padded at the end of the message if the last block is less than the length. This makes the sparsity matrix more complex. Thus, the GD function, which calculates the distribution between each input message bit and appends 0's and 1's based on the distribution function, is deployed to overcome this drawback. Thus, the complexity of obtaining a sparse matrix is minimized; in addition, makes the encoding more reliable. Primarily, let the parity check

matrix of input (ζ_a) be (ψ). The parity matrix (ψ) is equated as,

$$\psi = \begin{bmatrix} 1 & 0 & 1 & 1 & 0 \\ 1 & 1 & 0 & 0 & 1 \\ 0 & 1 & 1 & 0 & 1 \\ \vdots & \vdots & \vdots & \vdots & \vdots \\ 1 & 0 & 0 & 1 & 0 \end{bmatrix} \quad (2)$$

The Gaussian distribution (GD) for the parity matrix (\mathcal{J}) is equated as,

$$\mathcal{J}_{v \times \omega} = \frac{1}{D} \exp \left(\frac{-(\psi - \mu_m)}{2\sigma_s^2} \right) \quad (3)$$

$$D = \sqrt{2\pi\sigma_s^2} \quad (4)$$

Here, the normalization constant is depicted as D , the mean is signified as μ_m , and the variance is delineated as σ_s . From the GD parity matrix (\mathcal{J}), the generator matrix (ξ) is given by,

$$\xi = |v : \omega| \quad (5)$$

Here, the input vector is signified as v , and the parity vector of the parity matrix is depicted as ω . Hence, the GD-LDPC block is equated as,

$$\xi \Theta \psi^T = 0 \quad (6)$$

Here, the transpose of the parity check matrix is signified as ψ^T . ϖ implies the output of the encoding phase using GD-LDPC. The pseudo-code for the proposed GD-LDPC is shown below.

PSEUDO CODE FOR GD-LDPC:

Input: Input files (ζ_a)

Output: Encoded bits (ϖ)

Begin

Initialize input vector (v), parity vector (ω), normalization constant (D), and maximum iteration (J_{max})

Evaluate target

Set iteration $J = 1$

While ($J \leq J_{max}$) **do**

Assume the parity check matrix (ψ)

Generate GD for the parity check matrix,

$$\mathcal{J}_{v \times \omega} = \frac{1}{D} \exp \left(\frac{-(\psi - \mu_m)}{2\sigma_s^2} \right)$$

Compute generator matrix

Evaluate GD-LDPC block, $\xi \Theta \psi^T = 0$

Compute target

If ($target \neq reached$) {

Set $J = J + 1$

} Else {

Terminate

} End if

End while

Return encoded bits (ϖ)

End

3.1.3 Rate Matching

In the process of encoding (ϖ), the completed bits are inputted into the rate-matching phase for the process of extracting the exact set of bits to be transmitted within a given transmission time interval. Here, by employing rate matching, the range of bits to be transferred is performed. The rate matching (R_m) is equated as,

$$R_m = R_c^{-1} \cdot (\varpi + 4) \quad (7)$$

Here, the code rate is depicted R_c^{-1} , the number of bits is signified as m , along with the encoded bits are delineated as ϖ .

3.1.4 Modulation

Here, after rate matching, the exact set of bits (R_m) obtained is mapped with CB-QPSK by utilizing the modulation block. The message signals cannot be transmitted over long distances since they have a very low frequency. Hence, modulation is essential. QPSK has a higher information transmission rate over other modulation techniques regarding which the QPSK has less bandwidth. One complex symbol as two binary bits is signified as QPSK. Thus, the QPSK receiver is more complex. The separated bits at the bit splitter are combined to mitigate such complexity. Next, for generating a Quadrature phase shift component, those combined mapped bits are multiplied with the same carrier. Primarily, the signals ($R_m(k)$) concerning time (k) are equated as,

$$R_m(k) = \sqrt{\frac{2\phi}{\lambda}} \cos(2\pi\gamma_x k + \hbar_c), c = 1, 2, 3, 4, \dots \quad (8)$$

$$\hbar_c = (2c - 1) \frac{\pi}{4} \quad (9)$$

Here, the energy per symbol is signified as ϕ , the angles of bits are depicted as \hbar_c , the symbol duration is delineated as λ , and the frequency of the carrier (x) is mentioned as γ_x . Hence, the two-dimensional signals space with unit basis functions $\alpha_1(k)$ and $\alpha_2(k)$ are equated,

$$\alpha_1(k) = \sqrt{\frac{2}{\lambda}} \cos(2\pi\gamma_x k), 0 \leq k \leq \lambda \quad (10)$$

$$\alpha_2(k) = \sqrt{\frac{2}{\lambda}} \sin(2\pi\gamma_x k), 0 \leq k \leq \lambda \quad (11)$$

The combined bits (CB)(\Re) in QPSK in the factorial form are expressed as,

$$\Re = \frac{c!}{l!(c-l)!} \quad (12)$$

$$l = \delta_{c1}(k)\alpha_1(k) + \delta_{c2}(k)\alpha_2(k) \quad (13)$$

$$\delta_{c1} = \sqrt{\phi} \cos \hbar_c \quad (14)$$

$$\delta_{c2} = \sqrt{\phi} \sin \hbar_c \quad (15)$$

Here, the combination of the QPSK signal is signified as l , the first signal is delineated as δ_{c1} , and the second signal is depicted as δ_{c2} . Thus, signal-space 4 points are encompassed in the signal constellation, which is given by,

$$\left(\pm \sqrt{\frac{\phi}{2}}, \pm \sqrt{\frac{\phi}{2}} \right) \quad (16)$$

Here, the total energy is equally split between the two carriers. Q_p implies the modulated QPSK's output.

3.1.5 Pulse Shaping

The phase shifting output (Q_p) is inputted into the pulse shaping phase, which is wielded to avoid Inter-Symbol-Interference (ISI). TL-RCF technique is deployed. Pulse-shaping filter employed for modelling the transmitted input suited for the communication channel by limiting the bandwidth of transmission is termed the RCF. By limiting the bandwidth during transmission, the ISI caused by the channel could be kept in control. Timing jitter is caused since the RCF suffers from the problem of in-band ripple and out-of-band attenuation. By using a Truncated Linear (TL) function, the above-said downside can be surpassed to map the range between

0 and 1. Primarily, by employing the TL function ($\aleph_v, 0$), the modulated output (Q_p) is truncated, which is equated as,

$$\aleph_v(Q_p) = \min \left(1, \max \left(0, \left(\frac{1+\nu}{2\nu} \right) + \frac{|Q_p|}{\nu} \right) \right) \quad (17)$$

Here, the roll-off area in the frequency domain is signified as ν . Next, a filter process is a performance by the

truncated signal ($\aleph_v(Q_p)$) where the Raised Cosine (RC) filter ($\wp_r(j)$) is given by,

$$\varphi_r(j) = \begin{cases} 1, \text{ for } |j| < 2N_0 - N \\ \cos^2 \left[\frac{\pi |j| + N - 2N_0}{4(N - N_0)} \right], \text{ for } 2N_0 - N < j < N \\ 0, \text{ for } |j| > N \end{cases} \quad (18)$$

Here, the frequency is signified as j , the minimum Nyquist bandwidth is depicted as N_0 , the transmission bandwidth depicted as N , surplus bandwidth is expounded as $N - N_0$, from this, signal Raised Cosine falls

above bandwidth N_0 of the truncated signal ($\mathfrak{S}_v(Q_p)$)

.The time domain ($\varphi_r(k)$) or impulse response of the RC filter is given by,

$$\varphi_r(k) = \sin c \left(\frac{k}{V_0} \right) \left[\frac{\cos(2\pi\eta k)}{1 - \left(\frac{2\eta k}{V_0} \right)^2} \right] \quad (19)$$

Here, the roll-of-factor is signified as η , and the bit interval is depicted as V_0 .

3.1.6 Pilot Insertion

The filtered output ($\varphi_r(k)$) is inputted into the pilot insertion phase. Here, pilot signals, which are deployed as the reference signal for communication purposes, are inserted; in addition, it is utilized to avoid noise. The estimation of frequency response at the pilot position () is given by

$$\ell = (\varphi_r(k))^{-1} f_{pi} \quad (20)$$

Here, the received pilot vector is signified as f_{pi} .

3.1.7 E-IFFT Conversion

Next, for transforming the input as of the frequency domain to the time domain, the input bit (ℓ) undergoes E-IFFT since it offers a simple way to modulate data onto orthogonal subcarriers. However, FFT is restricted to the range of input to be transformed. Thus, tapering functions, namely the Entropy model is defined to compensate for spectral leakage. Hence, the input bit is evaluated in the entropy model, which is given by,

$$F = \ell_1 \log_s \left(\frac{1}{\ell_1} \right) + \ell_2 \log_s \left(\frac{1}{\ell_2} \right) + \dots \quad (21)$$

Next, compute the entropy model with IFFT, ($p(y)$) which is given by,

$$p(y) = \sum_{q=0}^{W-1} F(q) S_W^{qy} \quad (22)$$

$$S_W^{qy} = e^{2\pi i q y / W} \quad (23)$$

Here, the input signal with range (q) is depicted as $F(q)$, the FFT length is signified as W , the periodicity factor is mentioned as S_W^{qy} , and the number of outputs is delineated as y .

3.1.8 Communication

The time domain signal ($p(y)$) pass through the OFDM channel; in addition, for mimicking the effect of many random processes that occur in nature, AWGN noise is added to the channel. The output of the channel (S_i) is given by,

$$S_i = p(y) + N_s, i = 1, 2, \dots, n \quad (24)$$

Here, the noise is depicted as N_s , and the total number of outputs is signified as n .

3.2 Receiver

The receiver receives the input (S_i) from the transmitter. In the transmitter, the operations are inversely done on the receiver block. Fast Fourier transform, Pilot extraction, Pulse reshaping, Demodulation, Rate dematching, and Decoding are done to retrieve the input data at the receiver. Finally, the original message can be viewed by the user. Next, by employing the transmitter phase and receiver phase, the process of CE takes place.

3.3. Channel Estimation

The proposed CEGTA-Bi-LSTM made the CE. Bi-LSTM is a DL neural network having the sequence information in both forward and backward directions with proper sigmoid activation function known as Adaptive Piecewise Linear Unit (APLU). This function can approximate any continuous function on a compact set which overcomes the gradient vanishing problem and improves the performance of CE. Several iterations are caused due to the random initialization of weight values; in addition, makes the estimation not static. Hence, for optimizing the network parameters, the CEGTO is proposed, which improves the performance of CE. The female beetle changes its position during the movement towards the golden male beetle. Now, there is a possibility of trapping in the local optimal solution by the female beetles. Thus, the protective strategies' efficacy for deterring predators may degrade. To update the female beetle solution, the Cauchy mutation strategy is utilized to preserve the details and also to preserve

the beetles falling to the local solution. Moreover, to prevent the protective strategies, an evading mechanism is introduced. To enhance the search capability of the golden tortoises, the Cauchy mutation strategy is briefly illustrated. Initially, the proposed CEGTO model divides the original population into '2' subpopulations in the evading mechanism. Next, two leaders with competitive fitness scores but low position proximity are identified. In Figure 2, the structure for the CEGTA-Bi-LSTM is shown.

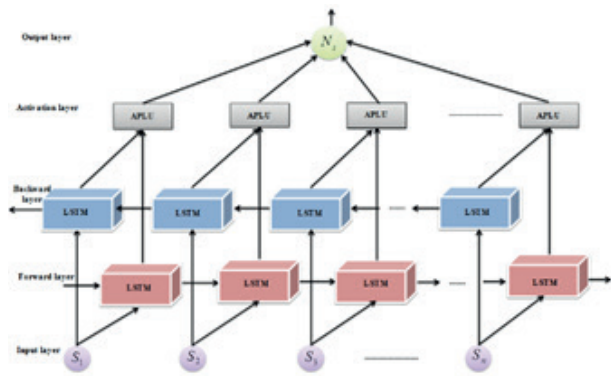


Figure 2: Architecture of the CEGTA-Bi-LSTM model.

Primarily, the received output (S_i) is inputted to the input layer of the proposed methodology. Next, initialize the weight values using the CEGTO [22] algorithm for the further process. The weight values are considered as golden tortoise beetles. Next, the initialized weight values are divided in to set of populations grounded on the best and worst velocity and position of the beetles using an evading process, which is given as follows,

$$g_{ul}^{v+1} = N * g_{ul}^v - d_1 * e_1 * (\varsigma_u - P_{ul}^v) - d_2 * e_2 * (\varepsilon - P_{ul}^v) \quad (25)$$

$$\varepsilon = \frac{z_1 + z_2 + z_3}{3} \quad (26)$$

$$P_{ul}^{v+1} = P_{ul}^v + g_{ul}^{v+1} \quad (27)$$

Here, the velocities of the u^{th} beetle during the v^{th} and $(v + 1)^{th}$ iteration of weight values are signified as g_{ul}^{v+1} and g_{ul}^v , the positions of the u^{th} beetle of weight values during the v^{th} and $(v + 1)^{th}$ iterations in the L^{th} dimension are depicted as P_{ul}^v and P_{ul}^{v+1} , the random vectors are signified as e_1 and e_2 , the acceleration constants are mentioned as d_1 and d_2 , the personal worst experience is expounded as ς_u , the mean solution of '3' global worst individuals is delineated as ε , and the iterations are depicted as z_1 , z_2 and z_3 . Moreover, the fitness of the two golden tortoises beetle group is computed. Accuracy is considered as fitness. For further process,

the best velocity and best position beetles are utilized; in addition, low position proximity is also identified. In

the u^{th} beetle, the x^{th} parameter's initial value ($\chi_{u,1}^x$) at problem generation with L dimensions are given by,

$$\chi_{u,1}^x = \chi_{min}^{x_{max}^u} \quad (28)$$

Here, the real-valued amounts uniformly distributed between the upper and lower bound of x^{th} parameter are depicted as χ_{min}^x and χ_{max}^x , and the lower bound parameter of the u^{th} beetle is mentioned as χ_{min}^u . Next, by employing '2' operators like the switching color operator along with the survival operator, the proposed system can be done.

a. Switching color operator

For mating with the golden beetle, the female beetle changes its position displaying an attractive golden color together with reproducing the next generation.

Hence, the number of mature beetles' (F_u^T) generated using the Cauchy mutation is given as,

$$F_u^T = B_u^T + Q_z \cdot (B_{gc_1}^T - (B_{best}^T + B_{best}^T \cdot \text{Cauchy}(0,1))) \quad (29)$$

$$Q_z = (f_i g_i \cdot \cos(t_i) + f_j g_j \cos(t_j)) + (t \cdot \beta) \quad (30)$$

Here, the current female beetle's position in generation (T) is signified as B_u^T , which moves towards the golden male beetle $B_{gc_1}^T$ in generation (T) that has a golden color with a value determined by the color switching operator (Q_z), a randomly generated integer is depicted as gc_1 , the solution with the best fitness at the generation (T) is mentioned as B_{best}^T , the normal random functions of beetles are delineated as f_i , g_i , f_j , g_j , a random number is depicted as t , the wavelength is denoted as β , and the angles of beetles are depicted as t_i and t_j .

b) Survival Operator

In the eggs laid by the tortoise beetles, a few beetle eggs will survive owing to their protective strategies' efficacy in deterring predators. The survival operator is equated as,

$$\begin{cases} Bee_1 = \Omega \chi_1 + (1 - \Omega) \cdot (\chi_1 - \sigma_1) \\ Bee_2 = \Omega \chi_2 + (1 - \Omega) \cdot (\chi_2 - \sigma_2) \end{cases} \quad (31)$$

Where, the random number generator is signified as Ω , the randomly chosen solutions are depicted as χ_1 and

χ_2 , and the variables are delineated as σ_1 and σ_2 . (γ) implies the output of the CEGTO algorithm. It calculates

the forward layer hidden sequence (\vec{h}_p) and a back-

ward layer hidden sequence (\vec{h}_p) [23] from the opposite direction, which is given as follows,

$$\vec{h}_p = G(U_{\vec{h}\gamma}\gamma_n + U_{\vec{h}\vec{h}}\vec{h}_{n-1} + o_{\vec{h}}) \quad (32)$$

$$\vec{h}_p = G(U_{\vec{h}\gamma}\gamma_n + U_{\vec{h}\vec{h}}\vec{h}_{n-1} + o_{\vec{h}}) \quad (33)$$

PSEUDO CODE FOR CEGTA-Bi-LSTM:

Input: Received output (S)

Output: Channel estimated output (N_γ)

Begin

Initialize weight values, random number generator (Ω), and maximum iteration (P_{max} 0)

//Input layer

Initialize the weight values using CEGTO algorithm

Set iteration $P = 1$

While ($P \leq P_{max}$ 0) **do**

Perform Evading process,

$$\mathcal{G}_{uL}^{v+1} = N * \mathcal{G}_{uL}^v - d_1 * e_1 * (\zeta_u - P_{uL}^v) - d_2 * e_2 * (\varepsilon - P_{uL}^v)$$

Evaluate fitness for both the population

If ($fitness \neq best$) {

Generate initial value

// switching color operator

Generate the number of mature beetles using Cauchy mutation,

$$F_u^T = B_u^T + Q_Z \cdot (B_{gc_1}^T - (B_{best}^T + B_{best}^T \cdot Cauchy(0,1)))$$

//survival operator

Surviving of some beetles,

$$\begin{cases} Bee_1 = \Omega \chi_1 + (1 - \Omega) \cdot (\chi_1 - \sigma_1) \\ Bee_2 = \Omega \chi_2 + (1 - \Omega) \cdot (\chi_2 - \sigma_2) \end{cases}$$

} Else {

Set $P = P + 1$

End if

End while

Return survived beetles (γ)

Perform forward layer hidden sequence (\vec{h}_p)

Perform backward layer hidden sequence (\vec{h}_p)

Evaluate output layer with APLU activation function,

$$g_w = W_f [U_{r\vec{h}}\vec{h}_p + U_{r\vec{h}}\vec{h}_p + o_r]$$

Return the channel estimated output

End

Here, the forward input-hidden weight along with backward input-hidden weight matrices are depicted

as $U_{\vec{h}\gamma}$ and $U_{\vec{h}\vec{h}}$, the previous forward and backward hid-

den sequence is signified as \vec{h}_{n-1} and \vec{h}_{n-1} , the bias vectors in both directions are mentioned as $o_{\vec{h}}$ and $o_{\vec{h}}$, and the hidden layer is delineated as G . Hence, the encoded vector (g_w) is formed by the concatenation of the final forward layer and backward layer output with APLU activation function is given by,

$$g_w = W_f [\vec{h}_p, \vec{h}_p] \quad (34)$$

The above equation can also be written as,

$$g_w = W_f \left[U_{r\bar{h}} \vec{h}_p + U_{r\bar{h}} \vec{h}_p + o_r \right] \quad (35)$$

$$W_f = \text{ReLU}(h_p) + \sum_{e=1}^l F_e \max.(0, -h_p + H_e) \quad (36)$$

Here, the APLU activation function is depicted as W_f , the real numbers are signified as F_e and H_e , the total bias vectors are mentioned as o_r , the total of forward and backward layer hidden sequence is expounded as h_p , and the forward weight and backward weight matrices are embodied as $U_{r\bar{h}}$ and $U_{r\bar{h}}$. Hence, the output of the CE phase is given by,

$$N_s = S - p(y) \quad (37)$$

Here, the output of the channel estimator is depicted as N_s . The pseudo-code for the proposed CEGTA-Bi-LSTM is shown on the previous page.

By employing CEGTA-Bi-LSTM, the CE process is done. Thus, to prove the model's effectiveness, the evaluation of this proposed methodology is necessary. The result section is explained further.

4 Results and discussions

Here, a new technique of 5G MIMO-OFDM CE using CEGTA-Bi-LSTM is compared and analyzed. MATLAB is

Table 1: Performance analysis for the proposed GD-LDPC.

Algorithms	Text		Video		Audio	
	Encoding time (s)	Decoding time (s)	Encoding time (s)	Decoding time (s)	Encoding time (s)	Decoding time (s)
Proposed GD-LDPC	0.00575	0.00131	0.041	0.0498	0.04687	0.05571
LDPC	0.02507	0.01575	0.0531	0.0595	1.56224	0.0821
Huffman	0.08056	0.05668	0.0831	0.0981	1.71073	0.26549
Arithmetic	0.28189	0.55849	1.0743	0.1115	2.555	0.3
Run Length	0.92048	1.11424	2.2401	0.4472	7.22466	0.36

Table 2: Analysis of the proposed CB-QPSK with the existing algorithms.

Algorithms	Text		Video		Audio	
	BER (bits/sec)	PSNR (dB)	BER (bits/sec)	PSNR (dB)	BER (bits/sec)	PSNR (dB)
Proposed CB-QPSK	0.084058	58.00	0.09942	31.6	0.097	32.7
QPSK	0.120588	36.2	0.1542	26.1	0.12	26.9
PSK	0.144928	34.5	0.16415	23.9	0.155904	22.3
QAM	0.724638	33.9	0.17542	15.6	0.156827	16.2
FSK	1	17.7	0.354	10.6	1	10

the working platform for this proposed methodology. From publicly available sources, the dataset is taken. Text, video, and audio are the '3' sorts of inputs.

4.1 Performance analysis

Grounded on '3' phases like encoding phase, modulation phase, and CE phase, the CE model is analyzed.

4.1.1 Performance analysis for encoding phase

Here, regarding encoding and decoding time, the proposed GD-LDPC's performance is weighed against the prevailing Low-Density Parity Check (LDPC), Huffman, Arithmetic, and Run Length.

The proposed GD-LDPCs are weighed against the prevailing methodologies in Table 1. The GD-LDPC acquired the lowest encoding and decoding time of 0.00575 s and 0.00131 s for text. For encoding and decoding, the GD-LDPC acquired 0.041 s and 0.0981 s for videos; while, the prevailing LDPC, Huffman, Arithmetic, and Run Length attained (0.0531 s and 0.0595 s), (0.0831 s and 0.0981 s), (1.0743 s and 0.1115 s), and (2.2401 s and 0.4472 s). The GD-LDPC also achieves the lowest time for audio. When analogized to other inputs, the proposed attains the lowest encoding and decoding time for text.

4.1.2 Performance analysis for modulation phase

Here, grounded on modulation and demodulation for the metrics Bit Error Rate (BER) and Peak Signal-to-Noise Ratio (PSNR), the proposed CB-QPSK's per-

formance is analogized to the prevailing Quadrature Phase Shift Keying (QPSK), Phase Shift Keying (PSK), Quadrature Amplitude Modulation (QAM), together with Frequency Shift Keying (FSK).

In Table 2, the performance analysis is depicted. The CB-QPSK attains the lowest BER. When analogized to the prevailing methodologies, the CB-QPSK achieves 58 dB for PSNR.

Likewise, for video, the CB-QPSK attains the lowest BER and higher PSNR. The CB-QPSK acquires the PSNR of 32.7 dB, which is 58 dB, 10.4 dB, 16.5 dB, and 22.7 dB lower when contrasted with the prevailing QPSK, PSK, QAM, and FSK; in addition, the CB-QPSK acquires lowest BER of 0.097 dB. Hence, enhanced outcomes are attained by the CB-QPSK.

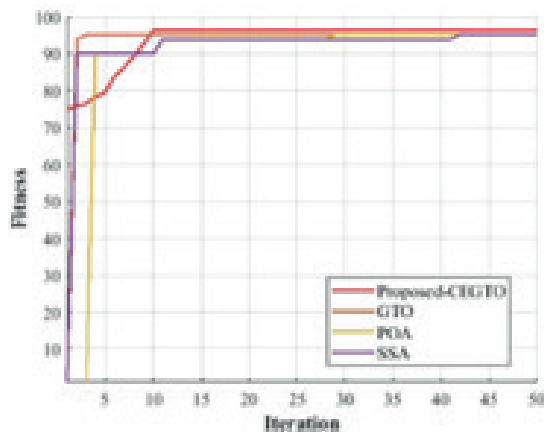


Figure 3: Fitness Vs iteration analysis.

4.1.3 Performance analysis for channel estimation

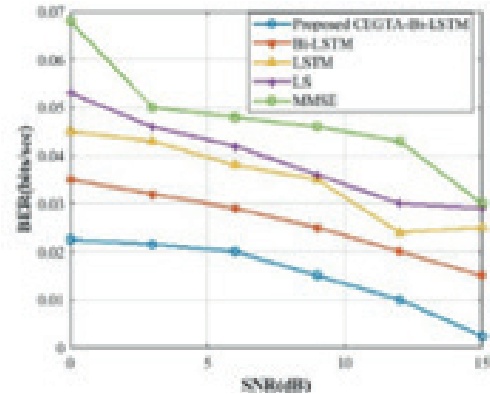
Here, grounded on PSNR, SE, Mean Squared Error (MSE), Symbol Error Rate (SER), and BER, the proposed CEGTA-Bi-LSTM's performance is analogized to the prevailing Bi-directional Long Short-Term Memory (Bi-LSTM), Long Short-Term Memory (LSTM), Least Squares (LS), and Minimum Mean Square Error (MMSE) centered on CE. In Figure 3, the fitness Vs iteration analysis for the proposed CEGTO is depicted.

4.1.3.1 Performance analysis for channel estimation

Here, regarding BER, MSE, PSNR, and SE, the CEGTA-Bi-LSTM's performance is weighed to the prevailing techniques.

In Figure 4, regarding (a) BER and (b) MSE, the CEGTA-Bi-LSTM's performance is analogized to the available methodologies. The proposed attains the BER and MSE values of 0.02 bits/sec and 3 at (5-10) SNR. The proposed algorithm attains the lowest BER and MSE values

(a)



(b)

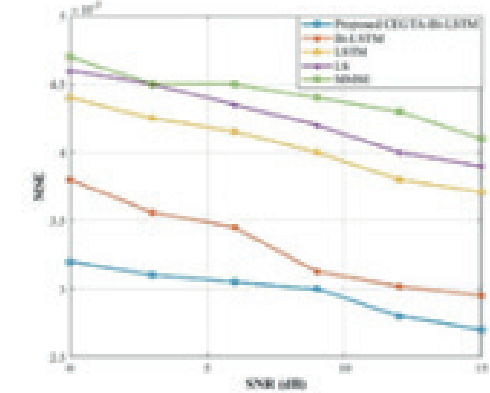


Figure 4: Performance analysis for the proposed algorithm with the existing algorithms based on (a) BER and (b) MSE.

at different SNR values. Hence, the CEGTA-Bi-LSTM is superior.

In Figure 5, regarding (a) PSNR, and (b) SE, the proposed CEGTA-Bi-LSTM's performance is evaluated with the available techniques. The CEGTA-Bi-LSTM attained the PSNR value approximately between 30dB and 35dB at (0-5) SNR; in addition, it acquired better results for the SE. The PSNR and SE values are better for all the SNR values.

4.1.3.2 Performance analysis for video data

Here, the CEGTA-Bi-LSTM's performance is evaluated with the prevailing systems grounded on BER, MSE, PSNR, and SE for video data.

The proposed technique is analyzed centered on (a) BER and (b) MSE in Figure 6. 0.05 to 0.1 at (10-15) SNR values; in addition, it attains enhanced outcomes for every SNR. Hence, the proposed system acquires superior outcomes for every metric.

In Figure 7, the proposed technique's performance is evaluated grounded on PSNR and SE. the proposed algorithm attains PSNR values approximately from 18

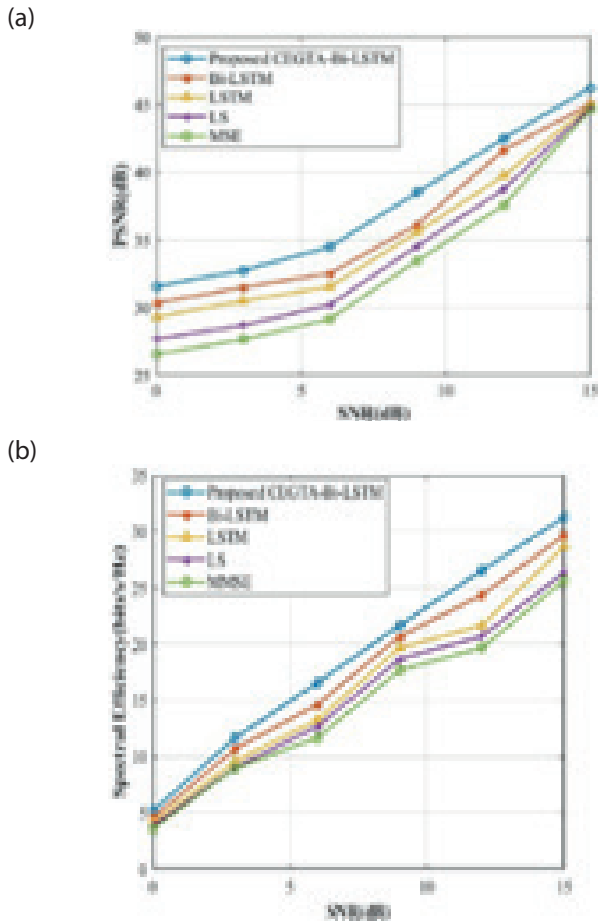


Figure 5: Graphical representation for the proposed algorithm with existing based on (a) PSNR and (b) SE.

to 26 dB at 0, 5, 10, and 15 SNRs, which is the highest PSNR value amongst the prevailing ones. The SE for the proposed algorithm is approximately 2 to 3 bits/s/Hz at 0 dB SNR value. At every SNR value, the proposed algorithm performed better.

5 Conclusion

This paper proposes a new technique of 5G MIMO-OFDM CE by utilizing CEGTA-Bi-LSTM. The transmitter, channel, and receiver are encompassed in the proposed technique. The proposed methodology's performance metrics are compared and analyzed grounded on the inputs like text, video, and audio. The proposed GD-LDPC is compared with existing algorithms in the encoding phase and attains an encoding and decoding time of 0.00575 s and 0.00131 s for text. The proposed CB-QPSK is compared with the existing algorithms in the modulation phase and attained a lower PSNR of 31.564 dB for video. The proposed CEGTA-Bi-LSTM achieves a lower BER of 0.029684 bits/sec for audio in the CE phase. But this work considered only CE whereas the rate of data transmission and channel capacity of

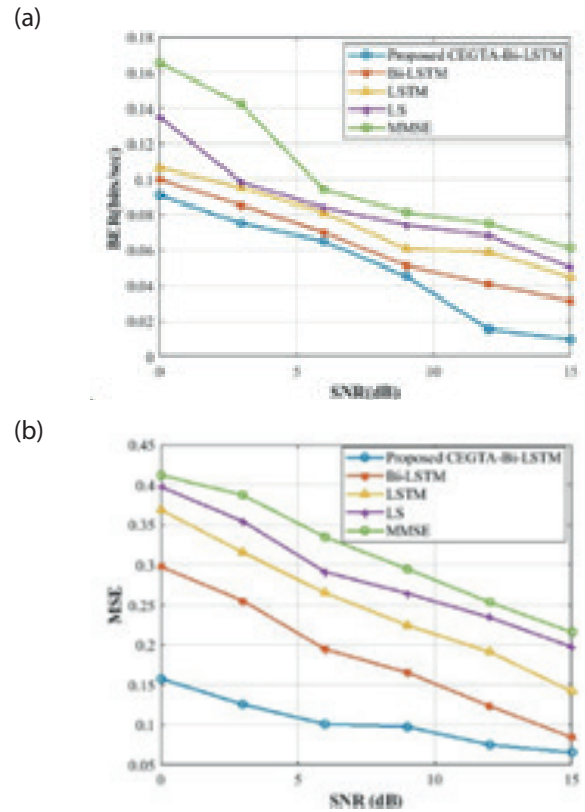


Figure 6: Performance analysis for the proposed with the existing based on (a) BER and (b) MSE.

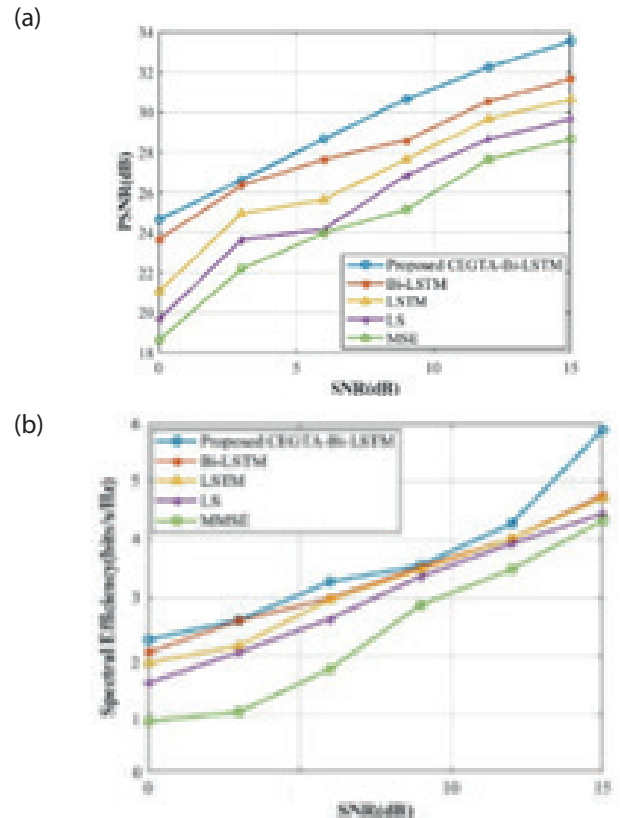


Figure 7: Graphical representation of (a) PSNR and (b) SE.

the system is not concentrated. In future, this work will be further enhanced by experimental implementation using LED and Optical Rx2 to improve transmission rate in channel estimation.

6 Acknowledgments

The author would like to express his heartfelt gratitude to Kalaivani Ramanathan for her guidance and unwavering support during this research.

7 Conflict of Interest

The authors declare that they have no known competing financial interests or personal relationships that could have appeared to influence the work reported in this paper.

8 References

1. X. Liu, W. Wang, X. Song, X. Gao, G. Fettweis, "Sparse channel estimation via hierarchical hybrid message passing for massive MIMO-OFDM systems," *IEEE Trans. Wireless Commun.*, 20, no. 11, pp. 7118–7134, 2021, <https://doi.org/10.1109/TWC.2021.3080923>
2. W. Ji, F. Zhang, L. Qiu, "Multipath Extraction Based UL/DL Channel Estimation for FDD Massive MIMO-OFDM Systems," *IEEE Access*, vol. 9, pp. 75349–75361, 2021, <https://doi.org/10.1109/ACCESS.2021.3081497>
3. R. Kanthavel, R. Dhaya and A. Ahilan, "AI-Based Efficient WUGS Network Channel Modeling and Clustered Cooperative Communication," *ACM Transactions on Sensor Networks*, vol. 18, no. 3, 2022, <http://dx.doi.org/10.1145/3469034>
4. S. Nandi, N. N. Pathak, A. Nandi, "A Novel Adaptive Optimized Fast Blind Channel Estimation for Cyclic Prefix Assisted Space-Time Block Coded MIMO-OFDM Systems," *Wireless Pers. Commun.*, vol. 115, no. 2, pp. 1317–1333, 2020. <https://doi.org/10.1007/s11277-020-07629-z>
5. Raghavendra, C.G., 2018. A novel approach to reduce the PMEPR of MCPC signal using random phase algorithm. *Informacije MIDEM*, 48(1), pp.63–70.
6. E. Balevi, A. Doshi, J. G. Andrews, "Massive MIMO channel estimation with an untrained deep neural network," *IEEE Trans. Wireless Commun.*, vol. 19, no. 3, pp. 2079–2090, 2020. <https://doi.org/10.1109/TWC.2019.2962474>
7. X. Cheng, R. Zayani, H. Shaiek, D. Roviras, "Inter-Numerology Interference Analysis and Cancellation for Massive MIMO-OFDM Downlink Systems," *IEEE Access*, vol. 7, pp. 177164–177176, 2019. <https://doi.org/10.1109/ACCESS.2019.2957194>
8. C. Venkateswarlu, N. V. Rao, "Optimal channel estimation and interference cancellation in MIMO-OFDM system using MN-based improved AMO model," *J. Supercomput.*, vol. 78, no. 3, 3402–3424, 2022. <https://doi.org/10.1007/s11227-021-03983-2>
9. M. Prabhu, B. Muthu Kumar and A. Ahilan, "Slime mould algorithm based fuzzy linear CFO estimation in wireless sensor networks," *IETE Journal of Research*, pp. 1–11, 2023, <https://doi.org/10.1080/03772063.2023.2194279>
10. X. Hong, J. Gao, S. Chen, "Semi-blind joint channel estimation and data detection on sphere manifold for MIMO with high-order QAM signaling," *J. Franklin Inst.*, vol. 357, no. 9, pp. 5680–5697, 2020. <https://doi.org/10.1016/j.jfranklin.2020.04.009>
11. P. Jiang, C. K. Wen, S. Jin, G. Y. Li, "Dual CNN-Based Channel Estimation for MIMO-OFDM Systems," *IEEE Trans. Commun.*, vol. 69, no. 9, pp. 5859–5872, 2021. <https://doi.org/10.1109/TCOMM.2021.3085895>
12. M. B. Mashhadi, D. Gunduz, "Pruning the Pilots: Deep Learning-Based Pilot Design and Channel Estimation for MIMO-OFDM Systems," *IEEE Trans. Commun.*, vol. 20, pp. 10, pp. 6315–6328, 2021, <https://doi.org/10.1109/TWC.2021.3073309>
13. L. Kansal, V. Sharma, J. Singh, "Multiuser Massive MIMO-OFDM System Incorporated with Diverse Transformation for 5G Applications," *Wireless Personal Commun.*, vol. 109, no.4, pp. 2741–2756, 2019. <https://doi.org/10.1007/s11277-019-06707-1>
14. M. Mehrabi, M. Mohammadkarimi, M. Ardakani, Y. Jing, "Decision Directed Channel Estimation Based on Deep Neural Network k-Step Predictor for MIMO Communications in 5G," *IEEE Journal on Selected Areas in Communications*, vol. 37, no. 11, pp. 2443–2456, 2019. <https://doi.org/10.1109/JSAC.2019.2934004>
15. Q. Wu, X. Zhou, C. Wang, H. Cao, "Variable pilot assisted channel estimation in MIMO-OFDM system with STBC and different modulation modes," *Eurasip Journal on Wireless Communications and Networking*, 1–13, 2022, <https://doi.org/10.1186/s13638-022-02126-2>
16. N. H. Cheng, K. C. Huang, Y. F. Chen, S. M. Tseng, "Maximum likelihood-based adaptive iteration algorithm design for joint CFO and channel estimation in MIMO-OFDM systems," *Eurasip Journal on Advances in Signal Processing*, 1–21, 2021. <https://doi.org/10.1186/s13634-020-00711-5>
17. T. Mata, P. Boonsrimuang, "An Effective Channel Estimation for Massive MIMO-OFDM System,"

- Wireless Personal Communications, vol. 114, no. 1, pp. 209–226, 2020.
<https://doi.org/10.1007/s11277-020-07359-2>
18. R. S. Suriavel rao, P. Malathi, "A low complex cuckoo search optimizer based OFDM carrier frequency offset estimation for 5G wireless technology," International Journal of Dynamics and Control, vol. 7, no. 3, pp. 1125–1134, 2019,
<https://doi.org/10.1007/s40435-019-00526-9>
 19. J. Gao, Y. Wu, Y. Wang, W. Zhang, F. Wei, "Uplink transmission design for crowded correlated cell-free massive MIMO-OFDM systems," Science China Information Sciences, vol. 64, no. 8, pp. 1–16, 2021.
<https://doi.org/10.1007/s11432-020-3103-3>
 20. A. Riadi, M. Boulouird, M. M. Hassani, "ZF and MMSE Detectors Performances of a Massive MIMO System Combined with OFDM and M-QAM Modulation," Wireless Personal Communications, vol. 116, no. 4, pp. 3261–3276, 2021.
<https://doi.org/10.1007/s11277-020-07848-4>
 21. S. Jothi, A. Chandrasekar, "An Efficient Modified Dragonfly Optimization Based MIMO-OFDM for Enhancing QoS in Wireless Multimedia Communication," Wireless Personal Communications, vol. 122, no. 2, 1043–1065, 2022.
<https://doi.org/10.1007/s11277-021-08938-7>
 22. O. Tarkhaneh, N. Alipour, A. Chapnevis and H. Shen, 2021. "Golden tortoise beetle optimizer: a novel nature-inspired meta-heuristic algorithm for engineering problems",
<http://dx.doi.org/10.2139/ssrn.4538126>
 23. G. Parimala and R. Kayalvizhi, Automatic Intrusion Detection Using Optimal Features with Adaptive Bi-Directional Long Short Term Memory. International Journal of Intelligent Systems and Applications in Engineering, vol. 12, no. 4s, pp.710-716. 2024,
<http://dx.doi.org/10.1109/conit51480.2021.9498552>



Copyright © 2024 by the Authors.
This is an open access article distributed under the Creative Commons Attribution (CC BY) License (<https://creativecommons.org/licenses/by/4.0/>), which permits unrestricted use, distribution, and reproduction in any medium, provided the original work is properly cited.

Arrived: 25. 01. 2024

Accepted: 03. 07. 2024

Preparation of Dielectric Layers for Applications in Digital Microfluidic Thermal Switches

Blaž Velkavrh^{1,2,3,*}, Urban Tomc², Matej Šadl¹, Victor Regis^{1,3}, Maja Koblar¹, Bianka Colarič², Andrej Kitanovski² and Hana Uršič^{1,3,*}

¹Jožef Stefan Institute, Electronic Ceramics Department, Ljubljana, Slovenia

²University of Ljubljana, Faculty of Mechanical Engineering, Ljubljana, Slovenia

³Jožef Stefan International Postgraduate School, Ljubljana, Slovenia

Abstract: In this work, we prepared dielectric layers of three different dielectric materials – Al_2O_3 , polyimide and epoxy-based photopolymer SU-8 and investigated their properties. Aerosol deposition method was used to prepare Al_2O_3 and polyimide layers, while spin-coating method was used for SU-8 layers. Microstructural analysis revealed dense layers with no anomalies. Temperature- and frequency-independent dielectric permittivity ϵ' was observed for Al_2O_3 and SU-8 layers, while there was slight downside trend with increasing temperature for polyimide layers. According to Young-Lippmann equation of electrowetting on dielectric (EWOD) effect, Al_2O_3 is considered to be the best due to highest ϵ' (~11) among all three materials, since it requires the lowest voltage to achieve certain droplet contact angle with EWOD.

Keywords: dielectric layers, aerosol deposition method, spin-coating method, microfluidics, thermal switch

Priprava dielektričnih plasti za uporabo v digitalnih mikrofluidnih toplotnih stikalih

Izvleček: V tem raziskavi smo pripravili dielektrične plasti iz treh dielektričnih materialov – Al_2O_3 , poliimid in fotopolimer na osnovi epoksida SU-8 ter raziskali njihove lastnosti. Za pripravo Al_2O_3 in poliimidnih plasti je bila uporabljena metoda nanašanja v aerosolu, za plasti SU-8 pa metoda nanašanja z vrtenjem. Mikrostrukturalna analiza je pokazala goste plasti. Pri plasteh Al_2O_3 in SU-8 smo opazili temperaturno in frekvenčno neodvisno dielektričnost ϵ' , medtem ko je pri poliimidnih plasteh viden rahlo padajoč trend z naraščajočo temperaturo. V skladu z Young-Lippmannovo enačbo učinka elektro-omočenja na dielektriku (EWOD) je Al_2O_3 zaradi najvišjega ϵ' (~11) smatran za najbolj ustrezen material za uporabo v EWOD, saj zahteva najnižjo napetost za doseganje določenega kontaktnega kota kapljice z EWOD.

Ključne besede: Dielektrične plasti, metoda nanašanja v aerosolu, metoda nanašanja z vrtenjem, mikrofluidika, toplotno stikalo

*Corresponding Author's e-mail: blaz.velkavrh@ijs.si, hana.ursic@ijs.si

1 Introduction

The manufacture of electronic, optical, and mechanical devices is experiencing a continuous trend of miniaturization, making devices small and compact, as well as increasing their power density and efficiency. One of the main techniques for manufacturing miniaturized electronic devices in large volumes is multilayer technology, where layered structures are deposited on

a substrate/board. These structures are prepared with additive processes and can consist of several conductive, semiconductive, or insulating dielectric layers with a typical thickness above 1 μm . The layers can be manufactured with different methods, for example powder-based technologies like screen-printing [1–3] and aerosol deposition (AD) [4–6], or solution-based like spin-coating method [7–9].

How to cite:

B. Velkavrh et al., "Preparation of Dielectric Layers for Applications in Digital Microfluidic Thermal Switches", Inf. Midem-J. Microelectron. Electron. Compon. Mater., Vol. 54, No. 3(2024), pp. 215–223

Advances in miniaturization have opened new problems of thermal management in small devices. With high power densities of compact devices, conventional heat sinks in combination with fans, heat pipes, or water cooling are insufficient to dissipate large amounts of heat to the ambient on a small scale. Potential solutions to improve thermal management on a smaller scale include thermal control devices, one of which is a digital microfluidic thermal switch based on electrowetting on dielectric (EWOD) effect [10–12]. Such a thermal switch requires a multilayer structure, consisting of a dielectric layer sandwiched between two electrode layers. The fabrication process of the dielectric layer has strong implications on its dielectric and thermal properties, which are a crucial factor in the performance of the thermal switch based on EWOD effect.

In this work, we investigated three different dielectric materials for EWOD applications. These three materials are alumina (Al_2O_3), polyimide, and epoxy-based photopolymer. Al_2O_3 was chosen due to its high electrical insulation, chemical inertness, and good mechanical properties [13–16]. On the other hand, dielectric polymers are low-cost materials with high electrical insulation [17]. The dielectrics were prepared in layer forms using AD (Al_2O_3 and polyimide) or spin-coating method (epoxy-based photopolymer) and their impacts on the voltage-dependent droplet contact angle were estimated by theoretical calculations.

2 Materials and methods

For preparation of dielectric layers, three different precursors were used, namely Al_2O_3 powder (A 16 SG, Almatiss, Germany), polyimide powder (P84 NT, Evonik, Germany) and epoxy-based photopolymer SU-8 (GM1070, Gersteltec, Switzerland). Al_2O_3 and polyimide layers were prepared with the AD method, while epoxy-based photopolymer SU-8 layers were prepared with the spin-coating method. For preparation of polyimide and epoxy-based photopolymer SU-8 layers, both precursors were used as received, while Al_2O_3 powder needed a pre-treatment to achieve a high deposition rate and homogeneous microstructure without large pores as reported in [14, 18].

Raw Al_2O_3 powder was first thermally pre-treated in a chamber furnace (Custom-made, Terna, Slovenia) at 1150 °C for 1 h with 5 K min⁻¹ heating and cooling rates, as suggested in [6, 14]. After thermal treatment, the powder was milled to obtain an appropriate particle size for AD, which is reported to be between 0.2 µm and 2 µm for the ceramic powders [4]. In our case, the d_{50} of the Al_2O_3 powder was 0.6 µm, as shown in Sup-

plementary material: Figure S1. The milling was performed in a planetary mill (PM400, Retsch, Germany) at 200 min⁻¹ for 4 h, using yttria-stabilized zirconia milling balls with isopropanol as a liquid medium.

For the preparation of dielectric layers, different substrates were chosen to optimize the deposition rate. Commercially available stainless-steel substrates (SS; no. 304, American Iron and Steel Institute) with a polished surface (A480: no. 8, American Society for Testing and Materials) were used for the ceramic Al_2O_3 dielectric layers, as it had previously been shown that a high deposition rate of the ceramic powder can be achieved on these substrates [19, 20]. For polyimide and epoxy-based photopolymer SU-8 layers, glass was used as a substrate. Cr/Au bottom electrodes with a thickness of ~100 nm were sputtered on the glass substrates by a magnetron sputtering (Cinquepascal SRL, Italy).

The AD equipment was provided by Invertech, Germany. The process parameters during the AD for both Al_2O_3 and polyimide powders are gathered in Table 1.

For the spin-coating process, a spin-coater (WS-650MZ-23NPPB, Laurell, USA) was used to prepare epoxy-based photopolymer SU-8 layers. For better adhesion of epoxy-based photopolymer SU-8 on a gold-sputtered glass substrate, an adhesion promoter Omni-Coat (G112850, Kayaku Advanced Materials, USA) was used. During the preparation process, samples were thermally treated with an electric heater (C-MAG HS 7, IKA, Germany), according to instructions in the technical datasheet of epoxy-based photopolymer SU-8 [21]. The deposition was performed once without any repetition. The whole process is schematically presented in Figure 1.

Table 1: Aerosol deposition process parameters.

Process parameters	Value
Pressure in aerosol chamber [mbar]	<10
Nozzle slit size [mm ²]	(0.5 × 10)
Carrier gas	N ₂
Gas flow rate [L min ⁻¹]	2 – 4
Nozzle-substrate distance [mm]	5
Sweep speed [mm s ⁻¹]	10

The thickness and root-mean-square roughness (R_q) of the prepared layers were evaluated from line profiles, measured with a contact profilometer (DektakXT, Bruker, USA). Thickness was determined from the step height of the layer, while R_q was evaluated with filtering the total profile using Gaussian regression with a cut-off 0.08 mm.

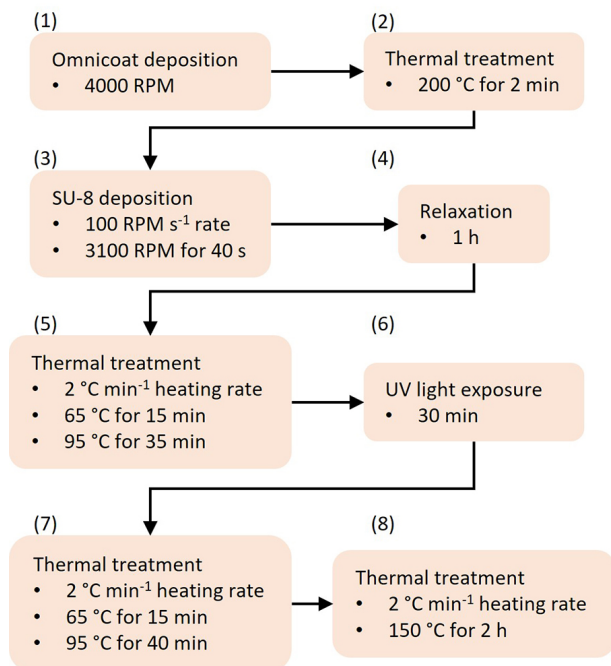


Figure 1: Schematic presentation of epoxy-based photopolymer SU-8 preparation process (after [21, 22]).

The topography images of the prepared dielectric layers were determined with the atomic force microscopes (AFM; Jupiter XR and MFP 3D, Asylum Research AFM, Oxford Instruments, USA). Images were scanned in AC air topography mode using tetrahedral platinum-coated silicon tips (OMCL-AC240TM-R3, Olympus, Japan). Prepared sample surfaces and their polished cross-sections were further investigated with scanning electron microscope (SEM; Verios G4 HP, Thermo Fisher Scientific, USA). To analyse the layers in cross-section, the samples were prepared by cutting, mounting in epoxy resin (EpoFixKit, Struers, Denmark), grinding, and fine polishing using a colloidal SiO₂ suspension (OP-S, Struers, Denmark).

For dielectric measurements, Au electrodes with a 0.5 mm diameter were sputtered on the top surface of prepared dielectric layers by a magnetron sputtering (Cinquepascal SRL, Italy). The temperature-dependent dielectric permittivity ϵ' and dielectric losses $\tan(\delta)$ were measured with Aixacct TF Analyzer 2000 (Aixacct Systems GmbH, Germany) and a HP 4284 A Precision LCR impedance meter (Hewlett-Packard, USA), using AC amplitude of 1 V at different frequencies during cooling in the temperature range from 100 °C to -30 °C. Theoretical voltage-dependent contact angles for a water droplet were calculated with a Young-Lippmann equation [11].

3 Results

Dielectric layers were prepared from ceramic Al₂O₃, polyimide and epoxy-based photopolymer SU-8. The microstructural and electrical properties are shown first. Later, to determine the influence of the dielectric layers on EWOD effect, the voltage-dependent contact angles for a water droplet were calculated.

3.1 Al₂O₃ layers prepared by the aerosol deposition method

Figure 2a shows a photograph of an Al₂O₃ layer on a stainless-steel substrate. AFM height and tapping amplitude images and SEM images in Figure 2b–2e revealed a layer surface with the root-mean-square roughness $R_q \approx 40$ nm. The concave depressions commonly found in aerosol-deposited layers can be found in the AFM height image (Figure 2b). These surface characteristics are formed by collision of powder particles with the surface layer during the AD process, as discussed previously in [23]. SEM layer-surface images (Figure 2d and 2e) revealed small powder particles with a size in the range of nanometres as part of the Al₂O₃ layer surface. A comparison of the particle size of the Al₂O₃ powder before AD (Supplementary material: Figure S1) with the particles in the layers indicates that Al₂O₃ particles break during the AD process, as previously discussed in [6]. The cross-section SEM image in Figure 2f revealed a dense 4 µm-thick Al₂O₃ layer on a stainless-steel substrate. No large defects or pores are observed, similar to Al₂O₃ layers, previously prepared by the same procedure and deposited on gadolinium substrates, as reported in [6]. Temperature-dependent ϵ' measurements are shown in Figure 3. The ϵ' remains constant at ~ 11 , independent of both temperature and frequency. The $\tan(\delta)$ slightly increases with increasing temperature but remains below 0.02 over the entire measurement range.

3.2 Polyimide layers prepared by the aerosol deposition method

Figure 4a shows a photograph of polyimide layer on a gold-sputtered glass substrate. AFM height and tapping amplitude images and SEM images in Figure 4b–4e revealed a rough layer surface with $R_q \approx 1.4$ µm. The concave depressions commonly found in AD layers are also visible in this case (Figure 4b), but they are deeper than in Al₂O₃, resulting in a higher surface roughness. In SEM images of the polyimide layer surface (Figure 4d and 4e), particles with a size of several tens to hundreds of nanometres can be seen. In the SEM images of the polyimide powder before AD (Supplementary material: Figure S2), a similar particle size was observed,

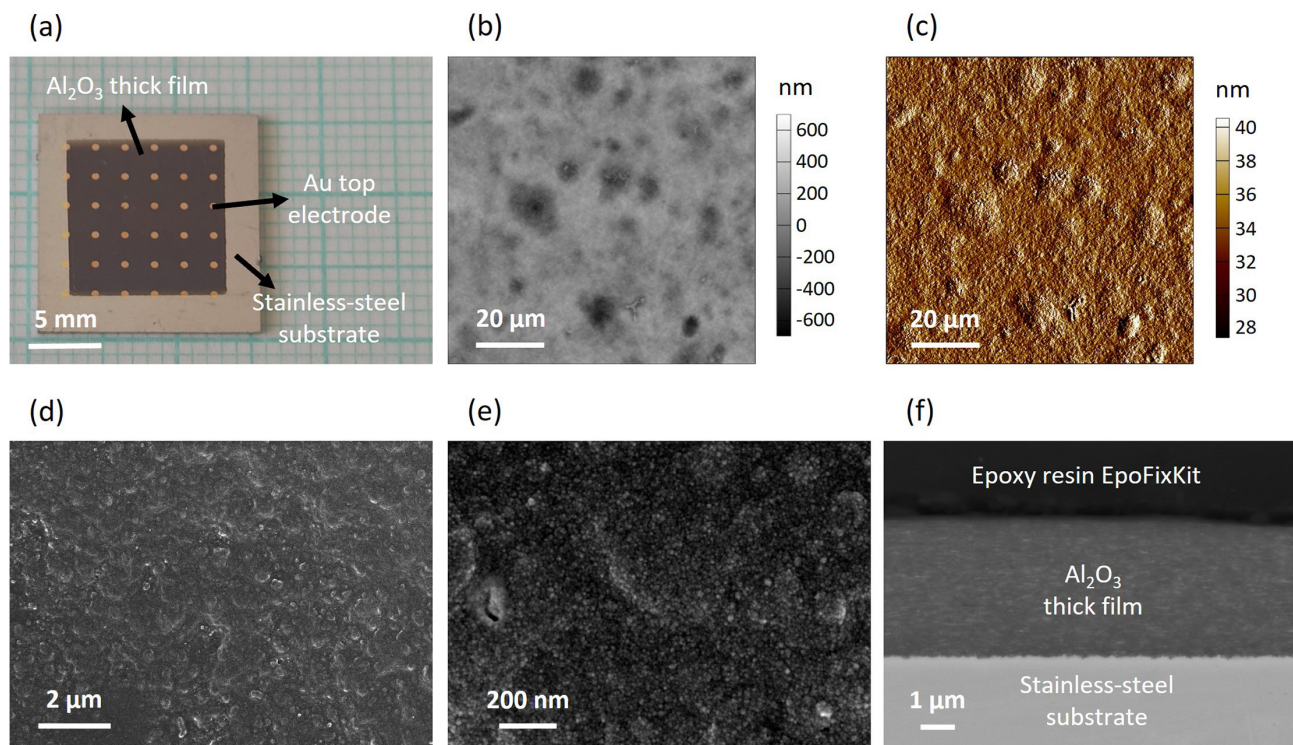


Figure 2: (a) Photograph of aerosol-deposited Al₂O₃ layer on stainless-steel substrate. AFM (b) height and (c) tapping mode amplitude images. SEM (d, e) surface and (f) cross-section images of the Al₂O₃ layer.

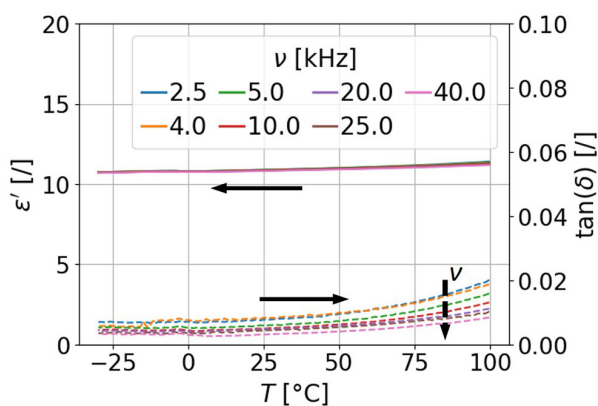


Figure 3: Temperature-dependent ϵ' and $\tan(\delta)$ of Al₂O₃ layer at different frequencies. The vertical black dashed arrow indicates increase in frequency.

but these particles were mainly agglomerated. Similar particle size before and after AD indicates that particles were not heavily fractured during the AD process, in contrast to ceramic Al₂O₃ particles. During AD, the agglomerates of polyimide particles break apart, while polyimide particles deform and stick together, resulting in the formation of dense polyimide layers. The cross-section SEM image of such a dense polyimide layer with a thickness $d \approx 19 \mu\text{m}$ is shown in Figure 4f. No large anomalies or pores are visible through the layer thickness. We can observe slight delamination of the bottom electrode from the glass substrate, which

is caused by mechanical forces arising from the curing process of the polymer epoxy-resin EpoFixKit during the cross-section sample preparation. Temperature-dependent ϵ' measurements are shown in Figure 5. The graph shows a slight downward trend of ϵ' with increasing temperature. No large frequency dependence is observed. On average, ϵ' remains at ~ 5.5 . The $\tan(\delta)$ slightly decreases with the increasing temperature but remains below 0.03 over the entire measurement range.

3.3 Epoxy-based photopolymer SU-8 layers prepared by spin-coating method

Figure 6a shows a photograph of epoxy-based photopolymer SU-8 layer on a gold-sputtered glass substrate. AFM height and tapping amplitude images as well as SEM surface images in Figure 6b–6e revealed a smooth layer surface with $R_q \approx 4 \text{ nm}$. While the SEM layer surface image at lower magnification (Figure 6d) does not reveal any details, SEM image at higher magnification (Figure 6e) shows small particles of epoxy-based photopolymer SU-8 with a size in nanometre range. The SEM cross-section image in Figure 6f revealed a dense layer with a thickness $d \approx 30 \mu\text{m}$ with no large anomalies or bubbles. Temperature-dependent ϵ' measurements are shown in Figure 7. The ϵ' remains constant at ~ 6.5 , independent of both temperature and frequency. The $\tan(\delta)$ slightly decreases

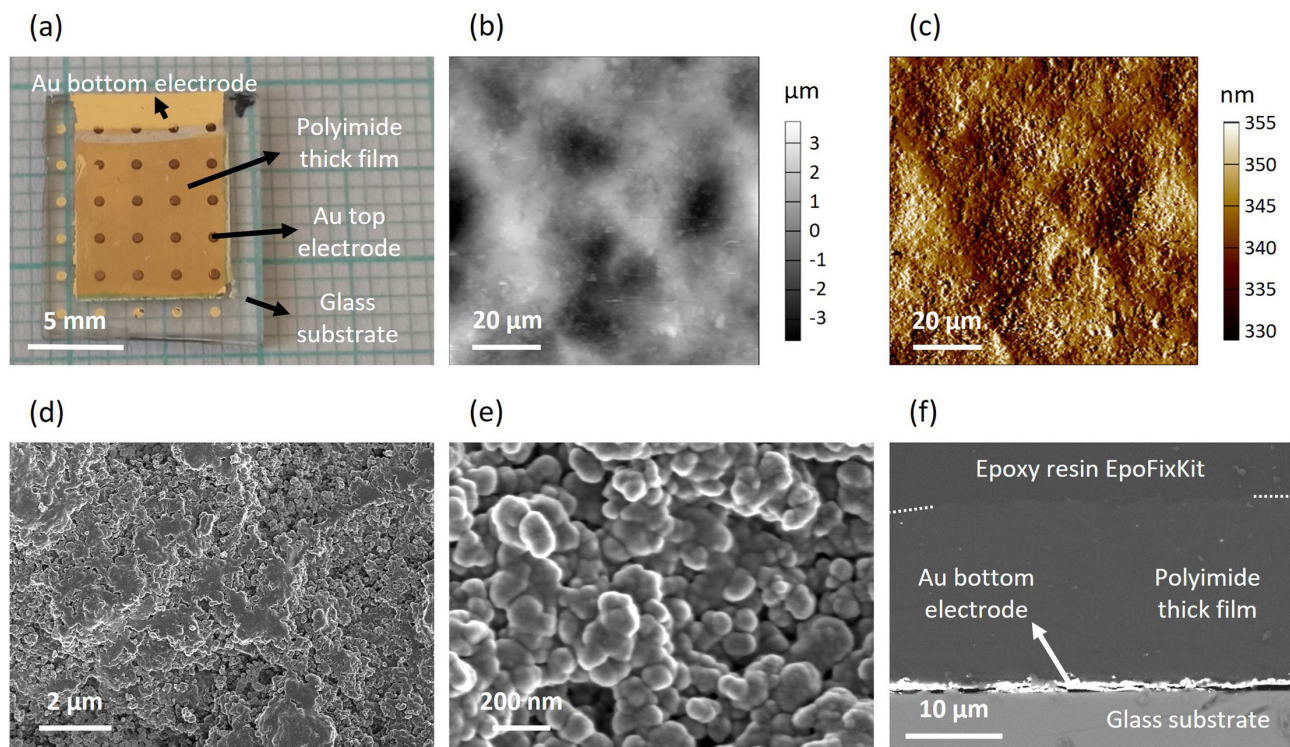


Figure 4: (a) Photograph of aerosol-deposited polyimide layer on gold-sputtered glass substrate. AFM (b) height and (c) tapping mode amplitude images. SEM (d, e) surface and (f) cross-section images of the polyimide layer. Please note that on panel (f), two white dotted lines in the corners of the image between the polyimide layer and the epoxy resin EpoFixKit are only the guide for the eye.

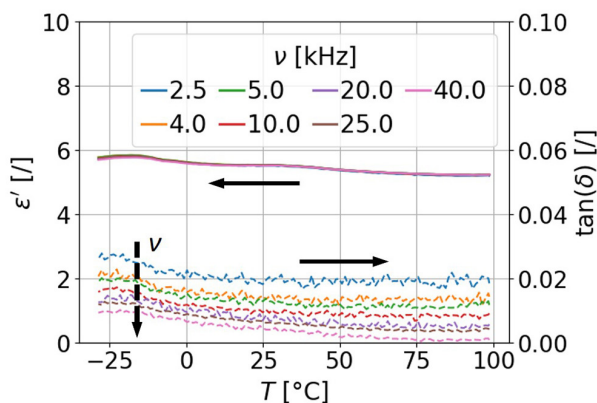


Figure 5: Temperature-dependent ϵ' and $\tan(\delta)$ of polyimide layer at different frequencies. The vertical black dashed arrow indicates increase in frequency.

with increasing temperature, similar as in the case of polyimide layers (Figure 5). However, it remains below 0.05 over the entire measurement range.

3.4 Water droplet contact angles on dielectric layers

The roughness R_q and dielectric permittivity ϵ' of prepared layers are collected in Table 2. Polyimide layers prepared with AD method have the highest R_q , while epoxy-based photopolymer SU-8 layers, prepared with

spin-coating method have the lowest R_q between all three different types of layers. In AD, powder particles collide with layer surface and form rougher surface in comparison to spin-coating method. When comparing Al_2O_3 and polyimide layers, both prepared with AD method, huge difference in roughness can be observed. While ceramic Al_2O_3 particles break during the AD process, forming the surface with lower roughness, polyimide particles deform and stick together, forming the surface with much higher roughness. The ceramic Al_2O_3 layers exhibited the highest dielectric permittivity ϵ' compared to both polyimide and epoxy-based photopolymer SU-8 layers.

Table 2: The root-mean-square surface roughness R_q and dielectric permittivity ϵ' of prepared dielectric layers.

	Aerosol deposition		Spin-coating
Material	Al_2O_3	Polyimide	SU-8
R_q [nm]	40	1400	4
ϵ' [] @ 10 kHz	11	5.5	6.5

Figure 8 shows theoretical voltage-dependent water droplet contact angles on Al_2O_3 , polyimide and epoxy-based photopolymer SU-8 layers. The voltage-dependent droplet contact angles of the water droplet were

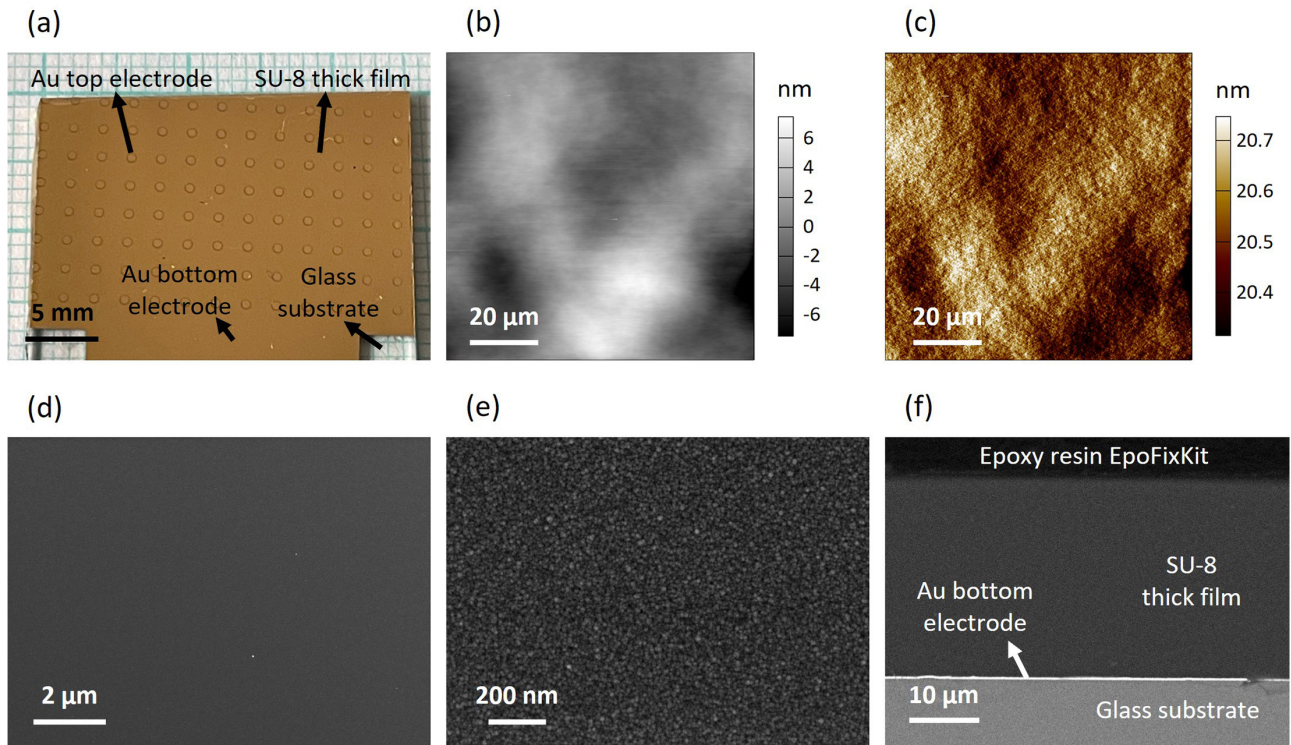


Figure 6: (a) Photograph of spin-coated epoxy-based photopolymer SU-8 layer on gold-sputtered glass substrate. AFM (b) height and (c) tapping mode amplitude images. SEM (d, e) surface and (f) cross-section images of the epoxy-based photopolymer SU-8 layer.

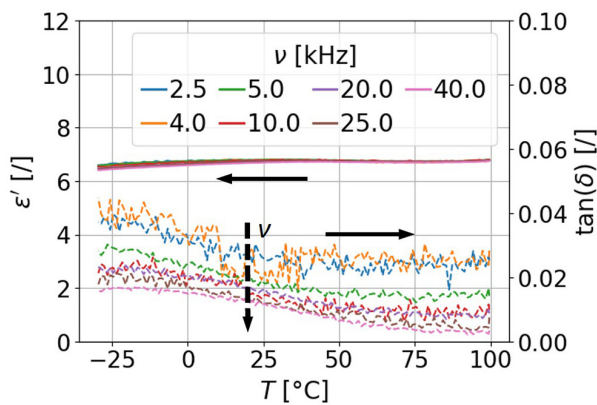


Figure 7: Temperature-dependent ϵ' and $\tan(\delta)$ of epoxy-based photopolymer SU-8 layer at different frequencies. The vertical black dashed arrow indicates increase in frequency.

calculated according to Young-Lippmann equation [11]:

$$\cos \theta_{\text{ew}}(U) = \cos \theta_{\text{eq}} + \frac{\epsilon_0 \cdot \epsilon'}{2 \cdot d \cdot \gamma_{\text{lv}}} \cdot U^2, \quad (1)$$

where ϵ' was taken from Table 2. The θ_{eq} is the initial droplet contact angle, θ_{ew} a contact angle when electric field is applied, ϵ_0 dielectric permittivity of a vacuum, U voltage, d thickness of the dielectric layer and γ_{lv} surface tension

of a liquid droplet. For a water droplet in air atmosphere at room temperature, $\gamma_{\text{lv}} = 0.072 \text{ N m}^{-1}$ was used [24]. An additional hydrophobic layer can be applied on the top of the dielectric layer to achieve high θ_{eq} . Therefore, $\theta_{\text{eq}} = 120^\circ$ was used according to technical datasheet of fluoropolymer FluoroPel 1601V (Cytonix, USA), commonly used for EWOD applications [25]. Graphs in Figure 8 indicate Al_2O_3 to be the best choice between all three materials for EWOD applications, since it has the highest ϵ' , resulting in lower voltage required to obtain certain contact angle at chosen layer thickness d . However, Young-Lippmann equation assumes smooth and ideally flat surfaces, but the roughness of the dielectric layers also needs to be considered, since it influences the surface wettability – droplet contact angle [26]. In addition, the roughness also has the influence on the interface thermal resistances in the multilayer structure, which effects the heat transfer capabilities of digital microfluidic thermal switch based on EWOD effect. Therefore, SU-8 might also be appropriate due to lowest roughness, which would positively effect heat transfer capabilities of multilayer structure.

4 Conclusions

The microstructural and electrical properties of different dielectric layers were investigated and their influence on

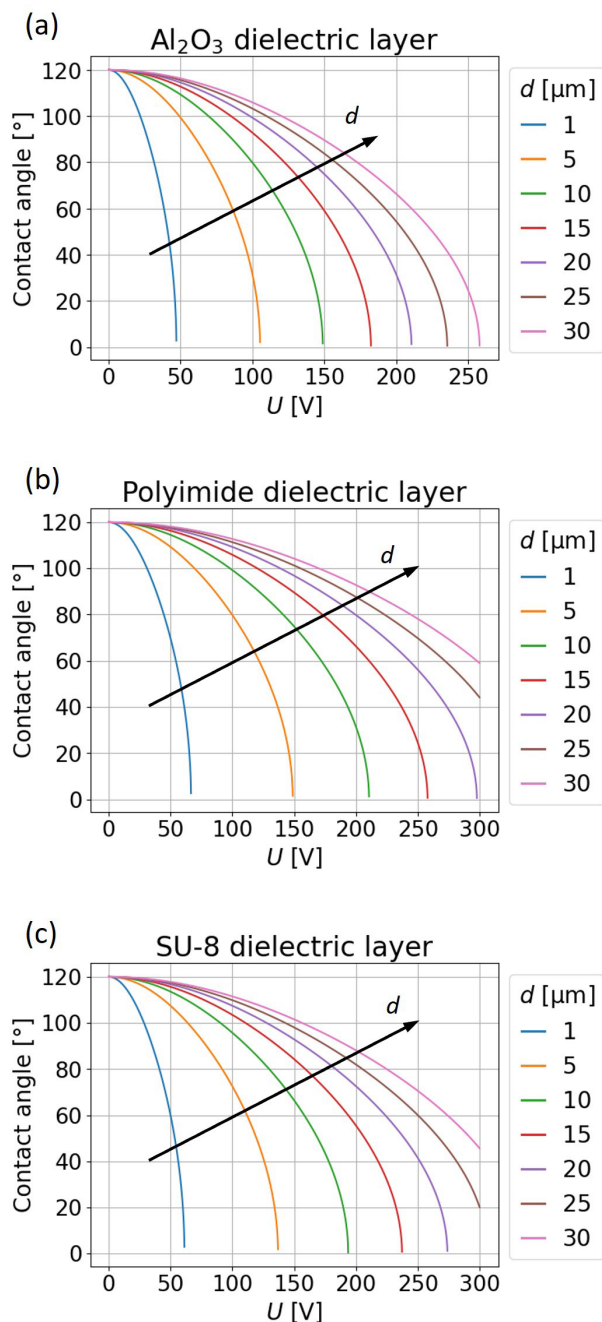


Figure 8: Theoretically calculated voltage-dependent contact angles for water droplets on (a) Al_2O_3 , (b) polyimide and (c) epoxy-based photopolymer SU-8 layers at different dielectric layer thicknesses.

the EWOD effect was determined. Al_2O_3 and polyimide layers were prepared with AD method, while epoxy-based photopolymer SU-8 was prepared with spin-coating method. Microstructural analysis revealed dense layers without any anomalies. Particle analysis indicates breaking of ceramic Al_2O_3 particles during the AD process. In the case of polyimide, big agglomerates, observed in raw powder, break apart during the AD process, while smaller polyimide particles deform and stick together. Dielectric

measurements revealed temperature- and frequency-independent dielectric permittivity ϵ' for Al_2O_3 and epoxy-based photopolymer SU-8, while slight temperature dependency of ϵ' can be observed in polyimide. Highest dielectric permittivity ϵ' between all three materials was measured in Al_2O_3 layers ($\epsilon' \sim 11$), indicating Al_2O_3 as the optimal choice for EWOD application.

5 Supplementary material

Supplementary material available on the publisher's web page contains:

- S1: Particle size distribution and SEM analysis of Al_2O_3 powder
- S2: Particle size distribution and SEM analysis of polyimide powder

6 Acknowledgments

The authors acknowledge financial support from the transnational consortium M-ERA.NET for the project Cool BatMan: Battery Thermal Management System Based on High Power Density Digital Microfluidic Magnetocaloric Cooling (No. 9400, Slovenian part of the project is financed by Ministry of Higher Education, Science and Innovation). Authors also acknowledge the financial support of the Slovenian Research and Innovation Agency for the research core fundings (No. P2-0422, P2-0223, J2-1738-1 and P2-0105). The assistance of Jena Cilenšek, Val Fišinger, Brigita Kmet and Andreja Benčan is gratefully acknowledged.

7 Conflict of interest

The authors declare no conflict of interest. The founding sponsors had no role in the design of the study; in the collection, analyses, or interpretation of data; in the writing of the manuscript, and in the decision to publish the results.

8 References

1. R. Dorey, *Ceramic Thick Films for MEMS and Micro-devices*. 2011.
<https://doi.org/10.1016/C2009-0-20338-2>.
2. M. Kosec, D. Kuscer, and J. Holc, "Processing of ferroelectric ceramic thick films," *Springer Series in Materials Science*, vol. 140, no. 1, 2011,
https://doi.org/10.1007/978-90-481-2875-4_2.

3. B. Malič, D. Kuščer, M. Vrabelj, and J. Koruza, "Review of methods for powder-based processing," in *Magnetic, Ferroelectric, and Multiferroic Metal Oxides*, 2018.
<https://doi.org/10.1016/B978-0-12-811180-2.00005-0>.
4. D. Hanft, J. Exner, M. Schubert, T. Stöcker, P. Fuierer, and R. Moos, "An overview of the Aerosol Deposition method: Process fundamentals and new trends in materials applications," *Journal of Ceramic Science and Technology*, vol. 6, no. 3, 2015.
<https://doi.org/10.4416/JCST2015-00018>.
5. J. Akedo, "Room temperature impact consolidation (RTIC) of fine ceramic powder by aerosol deposition method and applications to microdevices," *Journal of Thermal Spray Technology*, vol. 17, no. 2, 2008.
<https://doi.org/10.1007/s11666-008-9163-7>.
6. M. Sadl, U. Tomc, and H. Ursic, "Investigating the feasibility of preparing metal–ceramic multi-layered composites using only the aerosol-deposition technique," *Materials*, vol. 14, no. 16, 2021,
<https://doi.org/10.3390/ma14164548>.
7. T. Schneller, R. Waser, M. Kosec, and D. Payne, *Chemical solution deposition of functional oxide thin films*. 2013.
<https://doi.org/10.1007/978-3-211-99311-8>.
8. K. Norrman, A. Ghanbari-Siahkali, and N. B. Larsen, "Studies of spin-coated polymer films," *Annual Reports on the Progress of Chemistry - Section C*, vol. 101, 2005.
<https://doi.org/10.1039/b408857n>.
9. T. Pečnik, S. Glinšek, B. Kmet, and B. Malič, "Combined effects of thickness, grain size and residual stress on the dielectric properties of $\text{Ba}_{0.5}\text{Sr}_{0.5}\text{TiO}_3$ thin films," *J Alloys Compd*, vol. 646, 2015,
<https://doi.org/10.1016/j.jallcom.2015.06.192>.
10. K. Klinar, T. Swoboda, M. Muñoz Rojo, and A. Kitanovski, "Fluidic and Mechanical Thermal Control Devices," *Advanced Electronic Materials*, vol. 7, no. 3, 2021.
<https://doi.org/10.1002/aelm.202000623>.
11. F. Mugele and J. Heikenfeld, *Electrowetting: Fundamental Principles and Practical Applications*. Wiley-VCH, 2018.
<https://doi.org/10.1002/9783527412396>.
12. S. K. Cho, H. Moon, and C. J. Kim, "Creating, transporting, cutting, and merging liquid droplets by electrowetting-based actuation for digital microfluidic circuits," *Journal of Microelectromechanical Systems*, vol. 12, no. 1, 2003,
<https://doi.org/10.1109/JMEMS.2002.807467>.
13. T. Lampke et al., "Corrosion and wear behavior of alumina coatings obtained by various methods," *Materials Science*, vol. 46, no. 5, 2011,
<https://doi.org/10.1007/s11003-011-9328-2>.
14. M. Sadl, U. Tomc, U. Prah, and H. Ursic, "Protective alumina coatings prepared by aerosol deposition on magnetocaloric gadolinium elements," *Informacije MIDEM*, vol. 49, no. 3, 2019,
<https://doi.org/10.33180/infmidem2019.306>.
15. M. Linz, J. Exner, T. Nazarenus, J. Kita, and R. Moos, "Mobile sealing and repairing of damaged ceramic coatings by powder aerosol deposition at room temperature," *Open Ceramics*, vol. 10, 2022,
<https://doi.org/10.1016/j.oceram.2022.100253>.
16. B. Xie, Y. Li, J. Pan, and D. A. Hall, "Process optimisation of alumina coatings by modification of powder characteristics in the aerosol deposition method," *J Eur Ceram Soc*, vol. 44, no. 5, pp. 3147–3157, 2024,
<https://doi.org/10.1016/j.jeurceramsoc.2023.12.085>.
17. H. P. Palani Velayuda Shanmugasundram, E. Jayamani, and K. H. Soon, "A comprehensive review on dielectric composites: Classification of dielectric composites," *Renewable and Sustainable Energy Reviews*, vol. 157, 2022.
<https://doi.org/10.1016/j.rser.2022.112075>.
18. V. Regis, M. Šadl, G. Brennecka, A. Bradeško, U. Tomc, and H. Uršič, "Investigation of Structural and Electrical Properties of $\text{Al}_2\text{O}_3/\text{Al}$ Composites Prepared by Aerosol Co-Deposition," *Crystals (Basel)*, vol. 13, no. 5, 2023,
<https://doi.org/10.3390/cryst13050850>.
19. M. Sadl et al., "Energy-storage-efficient $0.9\text{Pb}(\text{Mg}_{1/3}\text{Nb}_{2/3})\text{O}_3-0.1\text{PbTiO}_3$ thick films integrated directly onto stainless steel," *Acta Mater*, vol. 221, 2021,
<https://doi.org/10.1016/j.actamat.2021.117403>.
20. N. H. Khansur, U. Eckstein, L. Benker, U. Deisinger, B. Merle, and K. G. Webber, "Room temperature deposition of functional ceramic layers on low-cost metal substrate," *Ceram Int*, vol. 44, no. 14, 2018,
<https://doi.org/10.1016/j.ceramint.2018.06.027>.
21. Gersteltec Sàrl, "Technical Datasheet GM1070." Accessed: Feb. 01, 2024. [Online]. Available: <https://www.gersteltec.ch/su8/>
22. M. T. Hong et al., "The Effect of Bake Temperature on SU-8 Gate Insulator of IGZO Thin Film Transistor," *Journal of the Korean Physical Society*, vol. 73, no. 3, 2018,
<https://doi.org/10.3938/jkps.73.297>.
23. D. W. Lee, H. J. Kim, and S. M. Nam, "Effects of starting powder on the growth of Al_2O_3 films on Cu substrates using the aerosol deposition method," *Journal of the Korean Physical Society*, vol. 57, no. 41, 2010,
<https://doi.org/10.3938/jkps.57.1115>.
24. The Engineering ToolBox, "Surface Tension - Water in contact with Air." Accessed: Feb. 04, 2024. [On-

- line]. Available: https://www.engineeringtoolbox.com/water-surface-tension-d_597.html
25. Cytonix, "FluoroPel PFC1601V." Accessed: Mar. 05, 2024. [Online]. Available: <https://cytonix.com/products/1601v>
26. X. Wang and Q. Zhang, "Role of surface roughness in the wettability, surface energy and flotation kinetics of calcite," *Powder Technol*, vol. 371, 2020, <https://doi.org/10.1016/j.powtec.2020.05.081>.



Copyright © 2024 by the Authors.
This is an open access article distributed under the Creative Commons Attribution (CC BY) License (<https://creativecommons.org/licenses/by/4.0/>), which permits unrestricted use, distribution, and reproduction in any medium, provided the original work is properly cited.

Arrived: 13. 05. 2024

Accepted: 18. 07. 2024

Cold Sintering of Perovskite–Perovskite Particulate Composite Based on $K_{0.5}Na_{0.5}NbO_3$ and $BiFeO_3$

Samir Salmanov^{1,2}, Danjela Kuščer^{1,2}, Mojca Otoničar^{1,2}

¹Electronic Ceramics Department, Jožef Stefan Institute, Ljubljana, Slovenia

²Jožef Stefan International Postgraduate School, Ljubljana, Slovenia

Abstract: The cosintering of particulate composites often presents a challenge due to the conventionally high processing temperatures used. Inter-diffusion of species between two phases and their volatilization, formation of secondary phases, and cracking or delamination of ceramics are effects that hinder the coupling of functional properties and reduce the final responses of such composites. This is particularly relevant when producing perovskite–perovskite composites from phases that are conventionally sintered at different temperatures (T_s), such as $K_{0.5}Na_{0.5}NbO_3$ (KNN; $T_s \approx 1100^\circ\text{C}$) and $BiFeO_3$ (BFO; $T_s \approx 800^\circ\text{C}$). Obtaining high-quality KNN–BFO multifunctional composite was the goal of this study. We demonstrate herein that the low-temperature sintering technique known as the Cold Sintering Process (CSP) can be utilized for producing particulate perovskite–perovskite composites, specifically KNN–BFO. We show that cold-sintered KNN–BFO composites have a dense microstructure, good phase-to-phase contact, are crack-free and exhibit ferroelectric properties. Their dielectric and ferroelectric properties are strongly affected by the fraction of KNN, increasing polarization saturation, while BFO aids in increasing their dielectric breakdown strength.

Keywords: cold sintering process; ferroelectric; particulate composite; $BiFeO_3$; $K_{0.5}Na_{0.5}NbO_3$

Hladno sintranje prahov perovskitov na osnovi $K_{0.5}Na_{0.5}NbO_3$ in $BiFeO_3$

Izvleček: Sosintranje dveh različnih praškastih keramičnih materialov v kompozitne strukture predstavlja izziv, saj keramika zahteva pripravo pri visokih temperaturah. Pri teh pogojih, difuzija ionov med dvema fazama, sublimacija, tvorba sekundarnih faz ter nastanek razpok ali delaminacija keramike vplivajo na lastnosti kompozita in poslabšajo njegove funkcijske lastnosti. To je še posebej pomembno pri izdelavi kompozitov iz dveh perovskitnih faz, ki se običajno sintrajo pri različnih temperaturah (T_s). Tak primer so kompoziti na osnovi $K_{0.5}Na_{0.5}NbO_3$ (KNN; $T_s \approx 1100^\circ\text{C}$) in $BiFeO_3$ (BFO; $T_s \approx 800^\circ\text{C}$) feroelektričnih sestav, KNN–BFO, katerih pripravo in lastnosti obravnava ta študija. Dokazali smo, da je mogoče tehniko nizkotemperaturnega sintranja, znano kot postopek hladnega sintranja (CSP), uporabiti za izdelavo kompozitov iz prahov dveh različnih feroelektričnih perovskitnih materialov, KNN in BFO. Pokazali smo, da imajo hladno sintrani kompoziti gosto mikrostrukturo, dober stik med fazami, so brez razpok in izkazujejo feroelektrični odziv. Na povišanje dielektričnih in feroelektričnih lastnosti močno vpliva delež KNN v kompozitu, ki povečuje polarizacijsko nasičenost, medtem ko BFO pripomore k povečanju njihove dielektrične prebojne trdnosti.

Ključne besede: hladno sintranje; feroelektriki; kompozit; $BiFeO_3$; $K_{0.5}Na_{0.5}NbO_3$

* Corresponding Author's e-mail: samir.salmanov@ijs.si

1 Introduction

Ferroelectric perovskites are widely used in a variety of electronic devices such as capacitors, sensors, actuators, and transducers [1]. Among environmentally friendly lead-free materials, $K_{0.5}Na_{0.5}NbO_3$ (KNN) is a suitable candidate to replace $Pb(Zr_{1-x}Ti_x)O_3$ (PZT) in

piezoelectric applications, and $BiFeO_3$ (BFO) [2]–[4] is widely investigated and used for multiferroic coupling or high-temperature piezoelectric applications. Combination of the two functional materials in the form of a multiferroic composites with properties that can be fine-tuned by adjusting amounts of each individual

How to cite:

S. Salmanov et al., "Cold Sintering of Perovskite–Perovskite Particulate Composite Based on $K_{0.5}Na_{0.5}NbO_3$ and $BiFeO_3$ ", *Inf. Midem-J. Microelectron. Electron. Compon. Mater.*, Vol. 54, No. 3(2024), pp. 225–233

phase could be beneficial for use in electronic devices, integrated as a single multifunctional component [5].

However, processing of perovskite-perovskite particulate composites by a conventional cosintering route is challenging due to different sintering temperatures of materials of different composition, volatilization of elements and their diffusion coefficients. In the case of KNN and BFO ceramics, KNN densifies in a narrow temperature range at ~1100 °C, close to its melting point of 1140 °C [2], while BFO densifies at ~300 °C lower temperature of 800 °C. Above ~950 °C BFO decomposes into liquid phase and Fe-rich phase and is fully melted at 1100 °C [4], [6]–[8]. It was also reported that cosintering of KNN and $\text{BaFe}_{12}\text{O}_{19}$ at 1125 °C led to volatilization of alkalies, resulting in decreased relative density of the composite [9]. It was further demonstrated for CoFe_2O_4 (CFO) and PZT composite that Fe^{3+} can diffuse into PZT, and Ti^{4+} can diffuse into CFO already at 900–1000 °C [10]–[12]. This diffusion facilitates secondary phase formation, limiting functional-property coupling between the two phases, and can cause creation of oxygen vacancies, leading to enhanced conductivity of the composite [10]. In an attempt to limit such diffusion, in the case of cosintering of BFO and BaTiO_3 [13], as well as BFO and PZT [14], low sintering temperatures were used, but the microstructure was highly porous.

Beside the different sintering temperatures of the composite phases and with that the possible interdiffusion of species between the two phases during cosintering, forming a third solid-solution phase, producing composites is challenging also due to different thermal expansion coefficient (TEC) of individual phases. The latter may cause strains at the interfaces of different phases and microcracks [15], [16] during cooling of the composite from the processing temperature due to different shrinkage parameters of the lattices. The cracking effect due to different TEC of two composite phases is more evident in the case of a layered composite structure, e.g., cosintering CFO and PZT in a sandwiched structure resulted in cracks along the interface and delamination of the structure [17]. On the other hand, it was shown for CFO–PZT [18] and Co-doped BFO–PZT composite [12], as well as in the cosintered $\text{BFO-Ni}_{0.5}\text{Co}_{0.5-x}\text{Zn}_x\text{Fe}_2\text{O}_4$ composite [19] that interfacial strains influence the lattice distortions of individual phases, contributing to large magnetoelectric coupling. In the case of materials of our interest, BFO and KNN, BFO has TEC of $10.9 \times 10^{-6} \text{ K}^{-1}$ and $12.2 \times 10^{-6} \text{ K}^{-1}$ for the temperature range 25–325 °C and 344–838 °C, respectively [20], while KNN has TEC of $2.96 \times 10^{-6} \text{ K}^{-1}$, $4.35 \times 10^{-6} \text{ K}^{-1}$ and $7.52 \times 10^{-6} \text{ K}^{-1}$ for the temperature range 30–195 °C, 208–364 °C and 434–790 °C, respectively [21]. This implies that BFO will shrink almost twice more than KNN when cooling down from the sintering

temperature, likely producing strains at the interfaces and/or cracks.

A way to severely limit thermal expansion/shrinkage, diffusion or volatilization of species during sintering of composites is to sinter at temperatures below 300 °C. Cold sintering process (CSP) is a sintering technique that allows densification of materials at temperatures even below 300 °C, under applied uniaxial pressure of a few hundreds of MPa and in the presence of a transient liquid phase, which facilitates material densification through a pressure-dissolution process [22]. The low processing temperature of the CSP provides opportunities for combining a variety of materials, i.e., ceramic with polymers or metals, as well as different types of oxides [23]–[27]. While different perovskites have been cold-sintered so far, including KNN-based compositions and BFO ceramics [28], there are no reports yet on cold sintering of perovskite-perovskite composites, which is a viable way to produce multifunctional components.

In this contribution we studied the processing of KNN–BFO perovskite-perovskite particulate composite with different ratios of phases, using the CSP. Based on our previous investigations on cold sintering of KNN [29], [30] and BFO [28], we utilized a eutectic mixture of NaOH and KOH as a transient liquid phase (TLP) to aid the sintering of the composite, which resulted in a homogeneous distribution of the two phases, no secondary phases formed at the grain boundaries, and a dense microstructure. The aim of our work is to illustrate that cold sintering can be successfully employed for combining two ferroelectric perovskite compositions to produce high-quality composites as multifunctional components.

2 Materials and methods

The initial powder compositions, BiFeO_3 with added 0.1 wt.% Co (named BFO hereafter), and $\text{K}_{0.5}\text{Na}_{0.5}\text{NbO}_3$ (KNN), were prepared via solid-state synthesis. Details on preparation can be found elsewhere (KNN powder was calcined at 850 °C) [31], [32]. Both powders were separately milled at 200 rpm for 0.5h (KNN) and 2h (BFO) after calcination to break the agglomerates. The mean particle of KNN was $d_{50} = 0.50 \mu\text{m}$ and for BFO $d_{50} = 1.39 \mu\text{m}$. Different ratios of KNN and BFO powders were then mixed together in an agate mortar to produce $(1-x)\text{KNN}-x\text{BFO}$ compositions with $x = 0, 0.33, 0.50$ and 0.66 and 1 (in weight fraction). The samples are denoted as: KNN, 33%BFO, 50%BFO, 66%BFO and BFO, respectively. Converting BFO weight % into volume %, the three compositions are 20%BFO, 35%BFO and

50%BFO, respectively. For each composition, 75 μl of NaOH-KOH aqueous equimolar mixture was added to 0.6 g of powders and manually mixed in an agate mortar. The NaOH-KOH solution was prepared by dissolving NaOH (molarity is 4.26 M) and KOH (molarity is 4.26 M) in water. The moist powders were put in the CSP instrument and pressed under 676 MPa uniaxial pressure (with a pressing rate of 13 MPa/minute) and heated to 300 °C (with heating and cooling rates of 2 K/min) and cold-sintered for 2 hours. The slow rates have previously been shown to produce reliable crack-free samples [33] and were chosen here for two reasons, one being better liquid/particle distribution in the green compact and the other being the polymorphic phase transition at about 170 °C for KNN which might cause large strains due to lattice volume changes and cracking of grains/pellet. After CSP, the obtained pellets with thickness ~ 1.8 mm and diameter of 8 mm were dried in vacuum

drier at 80 °C overnight. Microstructure analysis of cold-sintered samples was performed on polished samples using a scanning electron microscope using backscattered electrons (SEM; JSM 7600 F, Jeol Ltd., Tokyo, Japan). Relative density of cold-sintered samples was calculated based on measured porosity from several SEM images. For dielectric and ferroelectric measurements, the samples were thinned to 0.15-0.25 mm, and gold-sputtered on both sides (using sputtering system 5Pascal, Italy). Dielectric properties were measured with an LCR meter (Hewlett Packard, Tokyo, Japan). Ferroelectric properties (polarization vs. electric field) were measured with a TF2000 analyzer (AixACCT Systems GmbH, Aachen, Germany) at a frequency of 100 Hz with a sinusoidal voltage waveform until their breakdown. Selected samples were annealed in O_2 flow at 500 °C for 2 hours, with 2 K/min heating and cooling rates for dielectric measurements.

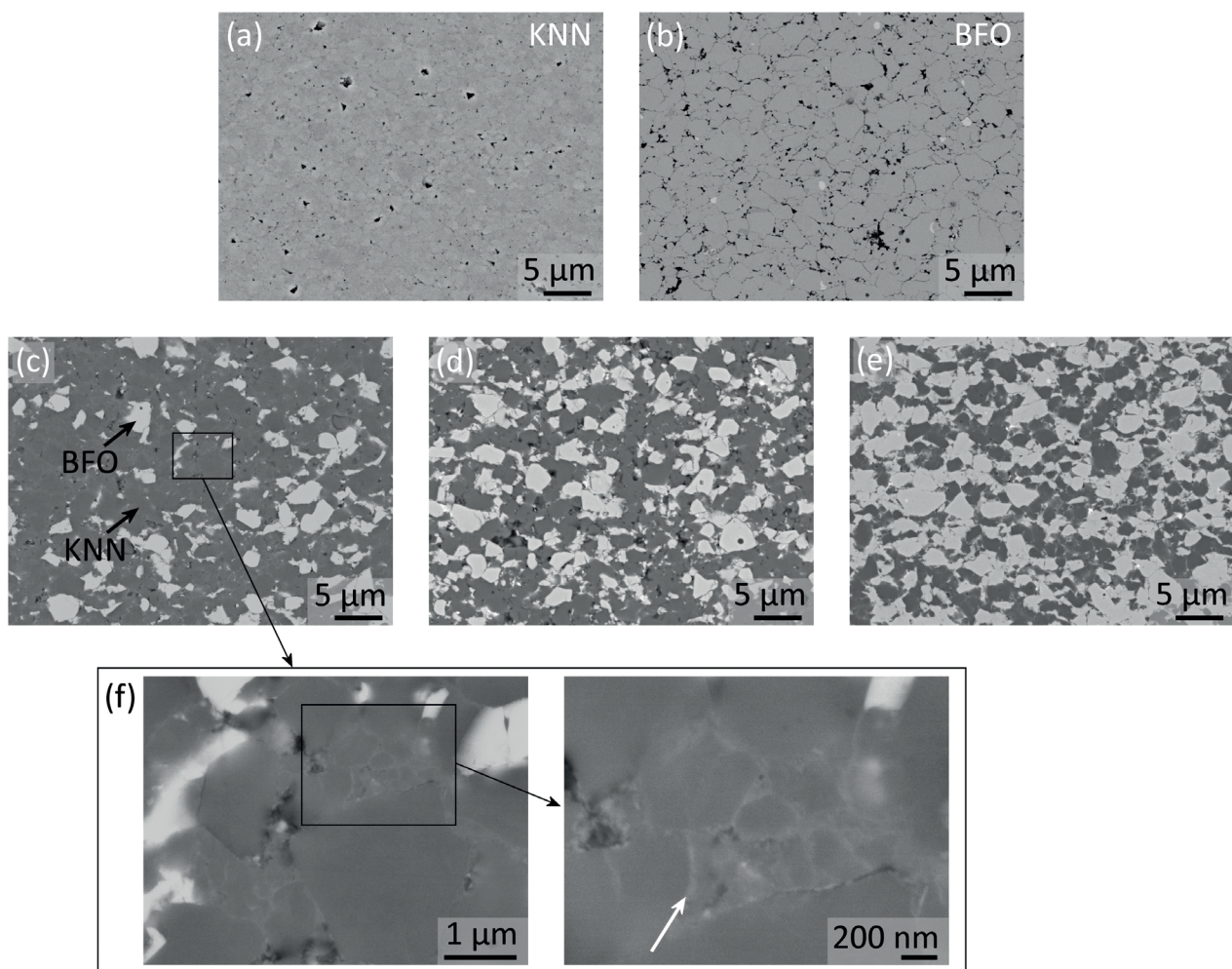


Figure 1: SEM images of ceramic samples cold sintered at 300 °C for 2 hours at 635 MPa with NaOH–KOH as a transient liquid phase: (a) KNN; (b) BFO; (c) 33%BFO; (d) 50%BFO and (e) 66%BFO (percentage given in wt.%). Light grey color of grains in the composites is BFO, and dark grey color of grains is KNN for (c), (d) and (e). Black spots are pores. (f) Enlarged area from 33%BFO composite in (c), showing grain-boundary contacts between KNN grains (white arrow in the right image).

3 Results and discussion

The microstructures of cold-sintered KNN–BFO composites with compositions 33%BFO, 50%BFO and 66%BFO, as well as single-phase KNN and BFO for comparison, are presented in Figure 1. The average grain size of KNN is about 1 μm or less, while BFO has larger grains, ranging up to 5 μm . No secondary phases are observed at the grain boundaries in KNN and BFO from the cold sintering procedure (Figure 1a–b). KNN shows higher relative density compared to BFO, with estimated 98 % compared to 94 %, respectively. Such a difference could be related to several reasons, one being better particle packing in KNN due to smaller initial particles. On the other hand, higher density of cold-sintered KNN compared to BFO can also be explained by the different levels of solubility of each ceramic in the base solution and/or eutectic liquid phase. It was previously shown for KNN dipped in aqueous solution of NaOH that the concentration of Nb^{5+} ions starts to increase already at 50 $^{\circ}\text{C}$ [34], indicating its significant solubility. No studies were found for the solubility of BFO, however, it was shown that during its hydrothermal synthesis it was only possible to dissolve and precipitate BFO species at temperatures above 175–200 $^{\circ}\text{C}$ [35]. This may indicate that KNN is more soluble in the

NaOH–KOH liquid phase compared to BFO, leading to higher densification levels of KNN during cold sintering. The third argument for better compaction of KNN could be its ability to significantly plastically deform with applied pressure that seems to exceed the yield strength of the material (e.g., for KNbO_3 crystal yield strength of 40 to 120 MPa was reported [36], [37]). Finally, the plastic deformation is realized through dislocation formation and lattice gliding [29], [30], [38], which may have been more efficient in KNN due to its lower density and/or weaker chemical bonding, resulting in a denser microstructure of KNN compared to BFO.

Microstructures of KNN–BFO composites (Figure 1c–e) show that KNN (dark grey phase) and BFO (bright grey phase) are homogeneously distributed, and the relative densities of 33%BFO, 50%BFO and 66%BFO, calculated from measured porosity from the microstructures, are $\sim 96\%$. Enlarged view of the 33%BFO composite in Figure 1f shows grain-boundary contacts, indicating good adhesion between the KNN grains, creating a matrix, with BFO grains well compacted between the sintered KNN grains.

These boundaries appear to be slightly curved, confirming the pressure-dissolution process [22] during

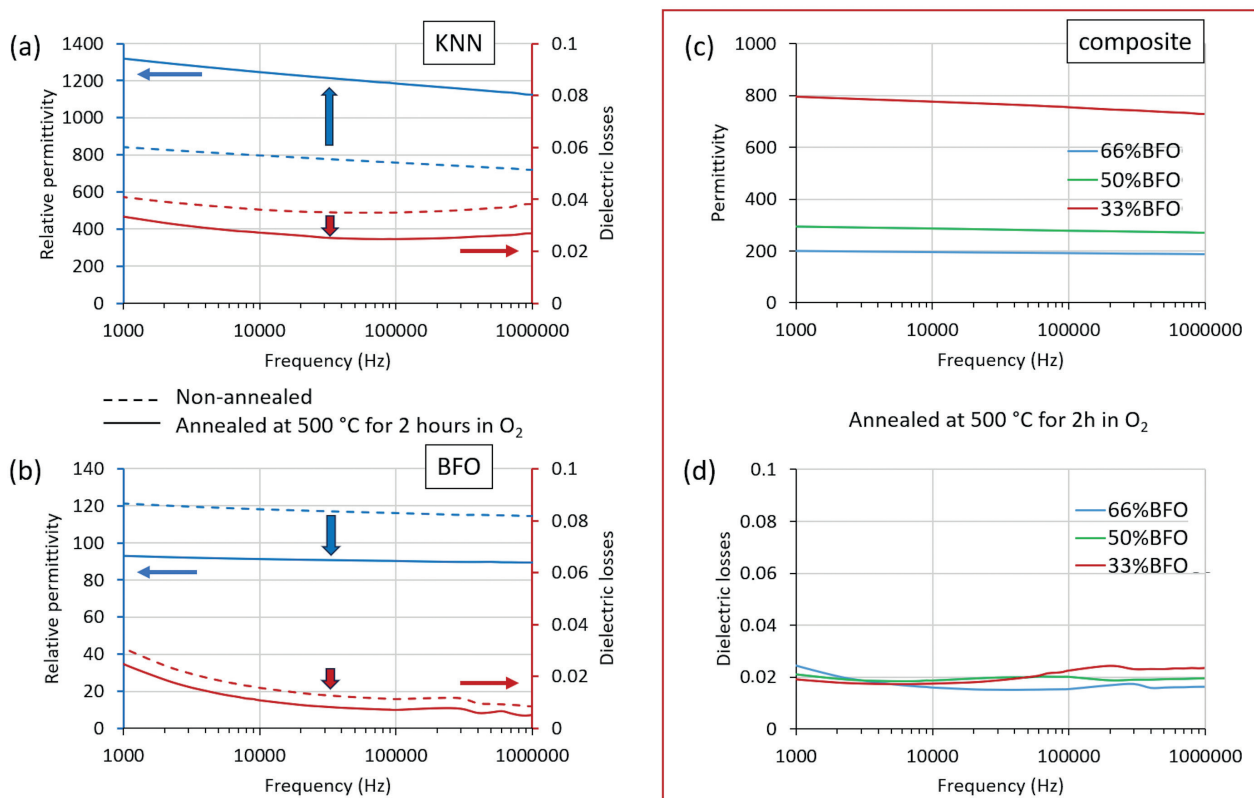


Figure 2: Comparison of dielectric permittivity and dielectric losses of as-prepared cold-sintered samples and samples annealed at 500 $^{\circ}\text{C}$ for 2 hours in O_2 (a) KNN and (b) BFO. (c) and (d) dielectric permittivity and losses of 33%BFO, 50%BFO and 66%BFO composites after annealing

cold sintering, but also appear lighter-grayish, which could indicate a Bi- or Nb-rich phase as a consequence of liquid-phase formation and precipitation of such a phase. The quantity of this phase, however, was too low to be identified by energy dispersive X-ray spectroscopy in SEM or X-ray diffraction. In 50%BFO, and especially in 66%BFO sample, contacts between BFO grains are observed that also show good contact and adhesion. No cracks are seen throughout the composites, which reflects good sintering and adhesion of grains, and minimal thermal expansion of the phases in the temperature range from sintering (300 °C) to room temperature.

The dielectric properties, presented in Figure 2, were measured on the as-prepared and dried cold-sintered KNN, BFO and composite samples, and after O₂ annealing. The as-prepared BFO exhibits the relative dielectric permittivity of ~120 and dielectric losses below 3% in a frequency range from 1 kHz to 1 MHz, and after annealing in O₂ no significant decrease in relative dielectric permittivity and dielectric losses is observed (Figure 2a). The cold-sintered KNN is characterized by a relative dielectric permittivity of ~800 and dielectric losses of 4% in a frequency range from 1 kHz to 1 MHz. However, after annealing in O₂, the dielectric permittivity increased by more than 50 %, while the dielectric losses decreased (Figure 2b). These results are consistent with previous data [30], [39]. The changes in dielectric properties after annealing in O₂ are believed to arise from the reoxidation of the perovskite and changes in the valence states of Nb atom, which was reduced from Nb⁵⁺ to Nb⁴⁺ during the CSP. For this reason, composites were also annealed in O₂.

The relative dielectric permittivity and dielectric losses of 33%BFO, 50%BFO and 66%BFO composites after annealing at 500 °C in O₂ are shown in Figure 2c and 2d, respectively. The 66%BFO composite exhibited relative dielectric permittivity of ~200, slightly higher than that of BFO. We can further follow a trend with increasing amount of KNN in the composites, resulting in an increase in the relative dielectric permittivity, with the value for the 33%BFO composite still lower than that of KNN. Especially notable is the difference in relative dielectric permittivity between 33%BFO and 50%BFO compared to the difference between 50%BFO and 33%BFO, which is minimal. This could be related to a critical amount of KNN in the composite. Since in 33%BFO there is only 20 vol. % of BFO, this suggests that the contribution to the relative dielectric permittivity of KNN dominates over BFO. On the other hand, the amount of BFO increases to 35 vol. % and 50 vol. % in 50%BFO and 66%BFO composites, respectively, increasing the contribution of BFO to the dielectric properties, decreasing the relative dielectric permittivity.

Interestingly, the values of the dielectric losses of all the composites were similar in the studied frequency range, but slightly higher in the low-frequency range in 66%BFO, similar to pure BFO, which could indicate local conductivity due to defect states in the BFO phase (Figure 2d).

The P–E-loops at 150 kV/cm applied electric field of cold-sintered KNN and BFO and composites 33%BFO, 50%BFO and 66%BFO are shown in Figure 3a. The results show that the coercive field (E_c) and remanent polarization (P_r) values of the composites are between the values for KNN and BFO. 33%BFO and 50%BFO samples show a similar P_r value, while P_r of 66%BFO is smaller, which is in line with the value of the major constituent phase, BFO. The KNN loop shows polarization saturation reached at 150 kV/cm applied, with $P_s=30 \mu\text{C}/\text{cm}^2$. The P–E loop of BFO, however, remains flat at this field and only starts to open at an applied electrical field greater than 150 kV/cm (see inset in Figure 3a for the BFO loop at 200 kV/cm). This indicates defect states in the material that unpin the domains only at stronger fields applied. The effect of defects seems to be hindered in the case of composites with increasing KNN phase, increasing also the P_r value. On the other hand, dielectric breakdown strength seems to be strongly affected by the amount of BFO in the composite, increasing the maximum possible applied electric field (E_{max}) (Figure 3b). We note here that while we did not systematically measure the dielectric breakdown strength of these materials, we consistently observe for all cold-sintered perovskites that the samples withstand larger electrical fields applied without their dielectric breakdown. The final reached value of P_r of the composite seems to be affected by the strength of the grain-boundary contacts between the KNN grains (see enlarged view in Figure 1f), which are more frequent in the composite with larger KNN amount. The analysis of the evolution of P–E loops with gradually increasing electric field for composites (Figure 3c–e) shows that in 66%BFO at maximum applied field (see the loop at 170 kV/cm) the P–E loop starts to open and becomes more rounded. This indicates a major contribution to electrical properties from the BFO phase with unpinning of defects and increased conductivity [31]. Comparison of the functional properties of cold-sintered samples is summarized in Table 1.

4 Conclusions

We demonstrated that CSP can be effectively utilized for sintering of perovskite–perovskite particulate composites based on different ratios of KNN and BFO. Microstructure analysis revealed that the composites have a

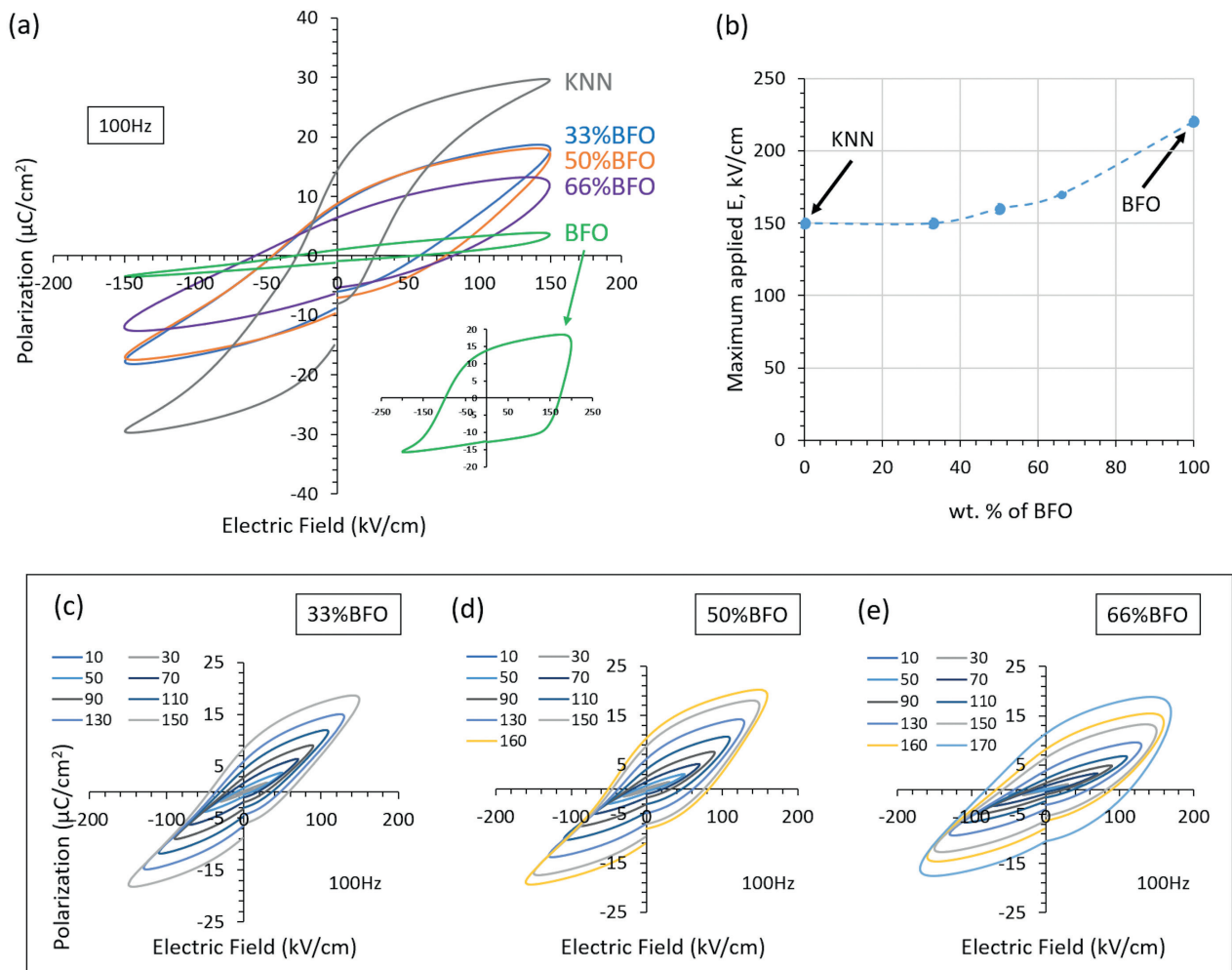


Figure 3: Comparison of ferroelectric properties cold-sintered KNN, BFO and composite ceramics after annealing 500 °C for 2 hours in O₂. (a) Polarization–electric-field (P–E) loops at 150 kV/cm. Inset shows the P–E loop of BFO at 200 kV/cm. (b) Maximum applied electric field during measurement of P–E loops for all samples before breakdown. (c)–(e) Evolution of P–E loops with increasing E for (c) 33%BFO, (d) 50%BFO and (e) 66%BFO composites. All measurements were done at 100 Hz

dense structure and homogeneously distributed KNN and BFO grains. Moreover, the contact regions between KNN and BFO grains did not exhibit any cracks or large pores, nor significant secondary phases. After annealing in O₂, the dielectric losses were below 3% across the entire frequency range of 1 kHz to 1 MHz and the values of relative dielectric permittivity were in line with KNN amount of KNN, increasing with increasing KNN fraction. Nevertheless, the composite with 66 wt. % of

BFO, where the contacts between KNN grains are rare, demonstrated approximately two times higher permittivity than single-phase cold-sintered BFO, and similar dielectric loss values. The composites showed decent ferroelectric properties and increasing polarization saturation with KNN content, while dielectric breakdown strength appeared higher with increasing BFO content. Remanent polarization is also enhanced by larger KNN fraction when up to 150 kV/cm field is applied, while

Table 1: Comparison of functional properties of cold-sintered samples

	Permittivity at 1kHz	Dielectric losses at 1kHz	Pr at 150 kV/cm	Pr at 200 kV/cm	E _{max} , kV/cm
KNN	~1300	~0.03	~14	-	150
33%BFO	~800	~0.02	~8	-	150
50%BFO	~300	~0.02	~8	-	160
66%BFO	~200	~0.02	~6	-	170
BFO	~100	~0.02	~2	~14	220

larger fraction of BFO in the composite allows to apply fields above 150 kV/cm, apparently increasing the breakdown strength of the composite.

5 Acknowledgments

The authors acknowledge the help of Brigita Kmet for KNN powder synthesis, Electronic Ceramics Department, Jožef Stefan Institute. The authors acknowledge the financial support of the Slovenian Research and Innovation Agency (core funding J2-2508, J2-50077, program P2-0105).

6 Conflict of Interest

The authors declare no conflict of interest.

7 References

1. G. H. Haertling, "Ferroelectric ceramics: history and technology," *J. Am. Ceram. Soc.*, vol. 82, no. 4, pp. 797–818, Apr. 1999, <https://doi.org/10.1111/j.1151-2916.1999.tb01840.x>.
2. B. Malič et al., "Sintering of lead-free piezoelectric sodium potassium niobate ceramics," *Materials (Basel)*, vol. 8, no. 12, pp. 8117–8146, Dec. 2015, <https://doi.org/10.3390/ma8125449>.
3. K. Hui et al., "KNN based high dielectric constant X9R ceramics with fine grain structure and energy storage ability," *J. Am. Ceram. Soc.*, vol. 104, no. 11, pp. 5815–5825, Nov. 2021, <https://doi.org/10.1111/jace.17970>.
4. T. Rojac et al., "BiFeO₃ Ceramics: Processing, Electrical, and Electromechanical Properties," *J. Am. Ceram. Soc.*, vol. 97, no. 7, pp. 1993–2011, Jul. 2014, <https://doi.org/10.1111/jace.12982>.
5. N. Ortega, A. Kumar, J. F. Scott, and R. S. Katiyar, "Multifunctional magnetoelectric materials for device applications," *J. Phys. Condens. Matter*, vol. 27, no. 50, p. 504002, Dec. 2015, <https://doi.org/10.1088/0953-8984/27/50/504002>.
6. M. I. Morozov, N. A. Lomanova, and V. V. Gusarov, "Specific features of BiFeO₃ formation in a mixture of bismuth(III) and iron(III) oxides," *Russ. J. Gen. Chem.*, vol. 73, no. 11, pp. 1676–1680, Nov. 2003, <https://doi.org/10.1023/B:RUGC.0000018640.30953.70>.
7. R. Palai et al., "β phase and γ–β metal-insulator transition in multiferroic BiFeO₃," *Phys. Rev. B*, vol. 77, no. 1, p. 014110, Jan. 2008, <https://doi.org/10.1103/PhysRevB.77.014110>.
8. M. S. Bernardo, "Synthesis, microstructure and properties of BiFeO₃-based multiferroic materials: A review," *Boletín la Soc. Española Cerámica y Vidr.*, vol. 53, no. 1, pp. 1–14, Feb. 2014, <https://doi.org/10.3989/cyv.12014>.
9. P. Kasaeipoor Naeini, T. Delshad Chermahin, M. Shayegh Boroujeny, B. Ebadzadeh, M. Nilforoushan, and M. Abdollahi, "Study of dielectric properties of lead-free multiferroic KNN/22.5 BaFe₁₂O₁₉ composites," *Adv. Ceram. Prog.*, vol. 7, no. 3, pp. 23–28, 2021, <https://doi.org/10.30501/ACP.2021.298611.1071>.
10. S. Basu, K. R. Babu, and R. N. P. Choudhary, "Studies on the piezoelectric and magnetostrictive phase distribution in lead zirconate titanate–cobalt iron oxide composites," *Mater. Chem. Phys.*, vol. 132, no. 2–3, pp. 570–580, Feb. 2012, <https://doi.org/10.1016/j.matchemphys.2011.11.071>.
11. P. Jenus, D. Lisjak, D. Kuscer, D. Makovec, and M. Drofenik, "The low-temperature cosintering of cobalt ferrite and lead zirconate titanate ceramic composites," *J. Am. Ceram. Soc.*, vol. 97, no. 1, pp. 74–80, Jan. 2014, <https://doi.org/10.1111/jace.12600>.
12. A. Marzouki et al., "New approach for designing bulk multiferroic composites made of two perovskite oxides with enhanced direct magnetoelectric coupling," *Scr. Mater.*, vol. 194, pp. 5–7, Mar. 2021, <https://doi.org/10.1016/j.scriptamat.2020.113673>.
13. M. Yao et al., "Great multiferroic properties in BiFeO₃/BaTiO₃ system with composite-like structure," *Appl. Phys. Lett.*, vol. 122, no. 15, Apr. 2023, <https://doi.org/10.1063/5.0139017>.
14. M. Yao et al., "Grain size and piezoelectric effect on magnetoelectric coupling in BFO/PZT perovskite-perovskite composites," *J. Alloys Compd.*, vol. 948, p. 169731, Jul. 2023, <https://doi.org/10.1016/j.jallcom.2023.169731>.
15. J. Chen, L. Hu, J. Deng, and X. Xing, "Negative thermal expansion in functional materials: controllable thermal expansion by chemical modifications," *Chem. Soc. Rev.*, vol. 44, no. 11, pp. 3522–3567, 2015, <https://doi.org/10.1039/C4CS00461B>.
16. T. C. Lu, J. Yang, Z. Suo, A. G. Evans, R. Hecht, and R. Mehrabian, "Matrix cracking in intermetallic composites caused by thermal expansion mismatch," *Acta Metall. Mater.*, vol. 39, no. 8, pp. 1883–1890, Aug. 1991, [https://doi.org/10.1016/0956-7151\(91\)90157-V](https://doi.org/10.1016/0956-7151(91)90157-V).
17. J. Zhou, H. He, Z. Shi, G. Liu, and C.-W. Nan, "Dielectric, magnetic, and magnetoelectric properties of laminated PbZr_{0.52}Ti_{0.48}O₃/CoFe₂O₄ composite ceramics," *J. Appl. Phys.*, vol. 100, no. 9, Nov. 2006, <https://doi.org/10.1063/1.2358191>.

18. L. K. Pradhan, R. Pandey, R. Kumar, and M. Kar, "Lattice strain induced multiferroicity in PZT-CFO particulate composite," *J. Appl. Phys.*, vol. 123, no. 7, Feb. 2018, doi: 10.1063/1.5008607.
19. Z. Manzoor, A. Khalid, G. M. Mustafa, S. M. Ramay, S. Naseem, and S. Atiq, "Magnetoelectric coupling caused by strain mediation in hetero-structured spinel-perovskite multiferroic composites," *J. Magn. Magn. Mater.*, vol. 500, p. 166409, Apr. 2020, <https://doi.org/10.1016/J.JMMM.2020.166409>.
20. J. D. Bucci, B. K. Robertson, and W. J. James, "The precision determination of the lattice parameters and the coefficients of thermal expansion of BiFeO₃," *J. Appl. Crystallogr.*, vol. 5, no. 3, pp. 187–191, Jun. 1972, <https://doi.org/10.1107/S0021889872009173>.
21. B. Malič, H. Razpotnik, J. Koruza, S. Kokalj, J. Cilenšek, and M. Kosec, "Linear thermal expansion of lead-free piezoelectric K_{0.5}Na_{0.5}NbO₃ ceramics in a wide temperature range," *J. Am. Ceram. Soc.*, vol. 94, no. 8, pp. 2273–2275, Aug. 2011, <https://doi.org/10.1111/j.1551-2916.2011.04628.x>.
22. A. Ndayishimiye, S. H. Bang, C. J. Spiers, and C. A. Randall, "Reassessing cold sintering in the framework of pressure solution theory," *J. Eur. Ceram. Soc.*, vol. 43, no. 1, pp. 1–13, Jan. 2023, <https://doi.org/10.1016/J.JEURCERAMSOC.2022.09.053>.
23. Y. Ji et al., "Cold sintered, temperature-stable CaSnSiO₅-K₂MoO₄ composite microwave ceramics and its prototype microstrip patch antenna," *J. Eur. Ceram. Soc.*, vol. 41, no. 1, pp. 424–429, Jan. 2021, <https://doi.org/10.1016/J.JEURCERAMSOC.2020.08.053>.
24. D. Wang et al., "Direct Integration of Cold Sintered, Temperature-Stable Bi₂Mo₂O₉-K₂MoO₄ Ceramics on Printed Circuit Boards for Satellite Navigation Antennas," *J. Eur. Ceram. Soc.*, vol. 40, no. 12, pp. 4029–4034, Sep. 2020, <https://doi.org/10.1016/J.JEURCERAMSOC.2020.04.025>.
25. J. Guo, S. S. Berbano, H. Guo, A. L. Baker, M. T. Lanagan, and C. A. Randall, "Cold Sintering Process of Composites: Bridging the Processing Temperature Gap of Ceramic and Polymer Materials," *Adv. Funct. Mater.*, vol. 26, no. 39, pp. 7115–7121, 2016, <https://doi.org/10.1002/adfm.201602489>.
26. X. Zhao, J. Guo, K. Wang, T. Herisson De Beauvoir, B. Li, and C. A. Randall, "Introducing a ZnO-PTFE (Polymer) Nanocomposite Varistor via the Cold Sintering Process," *Adv. Eng. Mater.*, vol. 20, no. 7, p. 1700902, Jul. 2018, <https://doi.org/10.1002/adem.201700902>.
27. H. Zubairi, F. Hussain, S. Sheikh, A. A. Shaikh, D. Wang, and I. M. Reaney, "Comparative study of cold assisted and conventional sintering of (1-2x) K_{0.5}Na_{0.5}NbO₃-xBaTiO₃-xBiFeO₃ multiferroic ceramics," *Mater. Sci. Eng. B*, vol. 296, p. 116632, Oct. 2023, <https://doi.org/10.1016/j.mseb.2023.116632>.
28. S. Salmanov et al., "Impact of transient liquid phase on the cold sintering of multiferroic BiFeO₃," *UNDER Rev. J. - Eur. Ceram. Soc.*, 2024.
29. K. Tsuji, Z. Fan, S. H. Bang, S. Dursun, S. Trolier-McKinstry, and C. A. Randall, "Cold sintering of the ceramic potassium sodium niobate, (K_{0.5}Na_{0.5})NbO₃, and influences on piezoelectric properties," *J. Eur. Ceram. Soc.*, vol. 42, no. 1, pp. 105–111, Jan. 2022, <https://doi.org/10.1016/j.jeurceramsoc.2021.10.002>.
30. S. Salmanov et al., "Structure and electrical properties of cold-sintered strontium-doped potassium sodium niobate," *J. Eur. Ceram. Soc.*, vol. 43, no. 16, pp. 7516–7523, Dec. 2023, <https://doi.org/10.1016/J.JEURCERAMSOC.2023.07.069>.
31. M. Makarovic et al., "Tailoring the electrical conductivity and hardening in BiFeO₃ ceramics," *J. Eur. Ceram. Soc.*, vol. 40, no. 15, pp. 5483–5493, Dec. 2020, <https://doi.org/10.1016/j.jeurceramsoc.2020.06.037>.
32. J. Hreščak, B. Malič, J. Cilenšek, and A. Benčan, "Solid-state synthesis of undoped and Sr-doped K_{0.5}Na_{0.5}NbO₃," *J. Therm. Anal. Calorim.*, vol. 127, no. 1, pp. 129–136, Jan. 2017, <https://doi.org/10.1007/s10973-016-5615-3>.
33. A. Jabr, J. Fanghanel, Z. Fan, R. Bermejo, and C. Randall, "The effect of liquid phase chemistry on the densification and strength of cold sintered ZnO," *J. Eur. Ceram. Soc.*, vol. 43, 2023, <https://doi.org/10.1016/j.jeurceramsoc.2022.11.071>.
34. A. Włodarkiewicz, M. E. Costa, and P. M. Vilarinho, "The dissolution of potassium sodium niobate (KNN) in aqueous media towards sustainable electroceramics sintering," *Mater. Des.*, vol. 233, p. 112169, Sep. 2023, <https://doi.org/10.1016/J.MATDES.2023.112169>.
35. S. H. Han et al., "Synthesis and characterization of multiferroic BiFeO₃ powders fabricated by hydrothermal method," *Ceram. Int.*, vol. 36, no. 4, pp. 1365–1372, May 2010, <https://doi.org/10.1016/j.ceramint.2010.01.020>.
36. A. F. Mark, M. Castillo-Rodriguez, and W. Sigle, "Unexpected plasticity of potassium niobate during compression between room temperature and 900°C," *J. Eur. Ceram. Soc.*, vol. 36, no. 11, pp. 2781–2793, Sep. 2016, <https://doi.org/10.1016/j.jeurceramsoc.2016.04.032>.
37. M. Höfling et al., "Large plastic deformability of bulk ferroelectric KNbO₃ single crystals," *J. Eur. Ceram. Soc.*, vol. 41, no. 7, pp. 4098–4107, Jul. 2021, <https://doi.org/10.1016/J.JEURCERAMSOC.2021.02.023>.

38. K. Nakagawa, M. Iwasaki, Z. Fan, J. I. Roscow, and C. A. Randall, "The unusual case of plastic deformation and high dislocation densities with the cold sintering of the piezoelectric ceramic $K_{0.5}Na_{0.5}NbO_3$," *J. Eur. Ceram. Soc.*, vol. 43, no. 9, pp. 4015–4020, Aug. 2023, <https://doi.org/10.1016/J.JEUCERAMSOC.2023.02.057>.
39. D. Kuscer *et al.*, "Evolution of phase composition and microstructure of sodium potassium niobate –based ceramic during pressure-less spark plasma sintering and post-annealing," *Ceram. Int.*, vol. 45, no. 8, pp. 10429–10437, 2019, <https://doi.org/10.1016/j.ceramint.2019.02.102>.



Copyright © 2024 by the Authors.

This is an open access article distributed under the Creative Commons

Attribution (CC BY) License (<https://creativecommons.org/licenses/by/4.0/>), which permits unrestricted use, distribution, and reproduction in any medium, provided the original work is properly cited.

Arrived: 29. 04. 2024

Accepted: 06. 08. 2024

Boards of MIDEM Society | *Organi društva MIDEM*

MIDEM Executive Board | Izvršilni odbor MIDEM

President of the MIDEM Society | Predsednik društva MIDEM

Prof. Dr. Barbara Malič, Jožef Stefan Institute, Ljubljana, Slovenia

Honorary president:

Prof. Dr. Marko Topič, UL, Faculty of Electrical Engineering, Slovenia

Vice-presidents | Podpredsednika

Prof. Dr. Janez Krč, UL, Faculty of Electrical Engineering, Ljubljana, Slovenia

Dr. Iztok Šorli, Mikroiks d.o.o., Ljubljana, Slovenia

Secretary | Tajnik

Olga Zakrajšek, UL, Faculty of Electrical Engineering, Ljubljana, Slovenia

MIDEM Executive Board Members | Člani izvršilnega odbora MIDEM

Prof. Dr. Slavko Bernik, Jožef Stefan Institute, Slovenia

Assoc. Prof. Dr. Miha Čekada, Jožef Stefan Institute, Ljubljana, Slovenia

Prof. DDr. Denis Donlagič, UM, Faculty of Electrical Engineering and Computer Science, Maribor, Slovenia

Prof. Dr. Vera Gradišnik, Tehnički fakultet Sveučilišta u Rijeci, Rijeka, Croatia

Mag. Leopold Knez, Iskra TELA, d.d., Ljubljana, Slovenia

Mag. Mitja Koprivšek, ETI Elektroelementi, Izlake, Slovenia

Asst. Prof. Dr. Gregor Primc, Jožef Stefan Institute, Ljubljana, Slovenia

Prof. Dr. Janez Trontelj, UL, Faculty of Electrical Engineering, Ljubljana, Slovenia

Asst. Prof. Dr. Hana Uršič Nemevšek, Jožef Stefan Institute, Ljubljana, Slovenia

Dr. Danilo Vrtačnik, UL, Faculty of Electrical Engineering, Ljubljana, Slovenia

Supervisory Board | Nadzorni odbor

Dr. Drago Resnik, retired, Slovenia

Prof. Dr. Franc Smole, retired, Slovenia

Prof. Dr. Drago Strle, UL, Faculty of Electrical Engineering, Ljubljana, Slovenia

Court of honour | Častno razsodišče

Darko Belavič, retired, Slovenia

Prof. Dr. Danjela Kuščer Hrovatin, Jožef Stefan Institute, Ljubljana

Dr. Hana Uršič Nemevšek, Jožef Stefan Institute, Ljubljana, Slovenia

Informacije MIDE
Journal of Microelectronics, Electronic Components and Materials
ISSN 0352-9045

Publisher / Založnik:
MIDEM Society / Društvo MIDE
Society for Microelectronics, Electronic Components and Materials, Ljubljana, Slovenia
Strokovno društvo za mikroelektroniko, elektronske sestavne dele in materiale, Ljubljana, Slovenija

www.midem-drustvo.si